

Unsteady Topology and Control of a Turbulent Boundary Layer Separation over an Airfoil

by

Austin Ma

A thesis submitted in partial fulfillment of the requirements for the degree of
Master of Science

Department of Mechanical Engineering
University of Alberta

© Austin Ma, 2020

Abstract

The subject of interest for this thesis is the detachment of a turbulent boundary layer. Engineers are interested in techniques that delay or suppress flow separation entirely because the performance of many fluidic devices, such as airfoil and diffuser, are hindered by this flow phenomenon. The sensitivity of flow separation to numerous flow-related parameters, and unsteady nature of the flow phenomenon contribute to the complexity of the subject. As a result, it is difficult to predict for the occurrence of flow separation using numerical methods. A fundamental understanding of separated flow is required to advance development of flow control techniques and predictive models for flow detachment. An experimental approach is used to characterize the unsteady topology of a three-dimensional flow separation from the trailing edge of an airfoil. Near-wall streamlines of the time-averaged flow revealed a flow topology known as a stall cell, which feature a saddle point and a pair of counter-rotating foci at the sides of the airfoil. Inspection of the time-resolved measurements revealed similar, but smaller, stall cell structures within the separation front. The instantaneous structures are created because of a region of strong local flow in either downstream or upstream direction, such as high-speed streaks. The momentum of the high-speed streaks are converted into a rotational motion at the separation front. In the latter part of the project, the feasibility of separation control using piezoelectric actuators is briefly explored through a parametric investigation. It is shown that the separation front is shifted downstream when an array of actuators operate synchronously. This effect is improved with increasing frequency, and the separation front was shifted by 4% of the chord length at the maximum frequency tested. No change is observed when adjacent actuators operated 180° out-of-phase.

Preface

All of the experimental work detailed in this thesis, including both the setup and collection of data, presented in this thesis were conducted by me personally with assistance from other lab members as required. Analysis of the collected data were done by me, the author of the thesis. However, some MATLAB codes were obtained from other lab members and then adapted for the data presented here.

The contents in chapter 4 of the presented thesis contains the results of a published paper under Journal of Fluid Mechanics. The published paper is given as

Ma, A., Gibeau, B., & Ghaemi, S. (2020). Time-resolved topology of turbulent boundary layer separation over the trailing-edge of an airfoil. *J. Fluid Mech.* (2020).

The results in section 4 are presented nearly identical to the published version with slight modifications to include more detail that was not necessary for the journal. I was responsible for designing the experiment, collecting and analyzing all of the data, generating all the figures, and writing almost all of the text. The two co-authors provided guidance and assistance with all those stages whenever required by me. In addition, the co-authors reviewed previous versions of the manuscript and offered suggestions for improvements. They also added or modified existing text where they felt necessary. Ownership of the content belongs to Cambridge University Press, but permission to reproduce the material here was obtained. The literature review section (section 2) may contain some material from the introduction of the published content.

The contents in chapter 5 of the thesis contain results that may be used for future publications. If so, the materials will be subjected to appropriate changes and then published. Once again, the contents is original work written by me under the guidance of the same coauthors as the published work in chapter 3.

Dedicated to my family and friends

Acknowledgement

First, I would like to thank Dr. Sina Ghaemi for the mentorship and guidance provided for the completion of this thesis. I would also like to thank Bradley Gibeau, who also played a tremendous role in guiding and assisting me towards the end of this project.

Secondly, I would like to thank Bernie Faulkner and Rick Conrad for manufacturing, assistance, and troubleshooting of the apparatuses used in this experiment. It should be noted that his assistance was always provided swiftly so that I may complete my experiments on schedule.

Lastly, I would like to acknowledge the support of the Natural Sciences and Engineering Research Council of Canada (NSERC) for the funding provided so I may focus on the completion of the project.

Table of Contents

Chapter 1. Introduction	1
1.1 Motivation	1
1.2 Thesis Outline	2
Chapter 2. Background	3
2.1 Boundary Layer Separation.....	3
2.1.1 Two-Dimensional Separation	3
2.1.2 Three-Dimensional Separation	8
2.1.3 Critical Point Theory.....	9
2.1.4 Airfoil Stall and Stall Cells	13
2.1.5 Leading-Edge Separation.....	14
2.2 Control of Flow Separation	17
2.2.1 Passive Flow Control	17
2.2.2 Active Flow Control	17
2.2.3 Piezoelectric Actuators for Flow Control	19
2.3 Particle Image Velocimetry.....	22
2.3.1 Fundamental Principle	22
2.3.2 Tracer Particles and Seeding.....	23
2.3.3 Image Quality.....	24
2.3.4 Image Correlation	25
2.4 Data Analysis Techniques.....	27
2.4.1 Proper Orthogonal Decomposition	27
2.4.2 Welch's Overlapped Segmented Average	28
Chapter 3. Experimental Setup	31
3.1 Wind Tunnel.....	31
3.2 Airfoil Model.....	32
3.3 Experiment I.....	36
3.3.1 Particle Image Velocimetry in the x - y Plane.....	37
3.3.2 Particle Image Velocimetry in the x - z Plane.....	38
3.3.3 Detection and Tracking of Critical Points	40

3.4	Experiment II.....	42
3.4.1	Actuator Setup and Modes.....	42
3.4.2	Actuator Dynamics	44
3.4.3	Particle Image Velocimetry Setup	45
Chapter 4. Three-dimensional turbulent-boundary layer separation over an airfoil.....		47
4.1	Mean Flow Characteristics.....	49
4.1.1	Turbulent Boundary Layer.....	49
4.1.2	Reynolds Stresses and Turbulence Transport at Mid-Span	51
4.1.3	Mean Skin-Friction Lines	53
4.1.4	Reynolds Stresses of the Near-Wall Plane.....	56
4.2	Unsteady Flow Characteristics.....	57
4.2.1	Energy Spectra	57
4.2.2	Spatial Organization of Critical Points	59
4.2.3	Instantaneous Forward and Backward Stall Cells	65
4.2.4	High-Speed Streaks.....	68
4.3	Energetic Motions	70
4.4	Summary and Conclusions.....	75
Chapter 5. Active Control of Flow Separation using Piezoelectric Actuators		78
5.1	Mean Velocity Flow Fields	79
5.2	Reynold stresses	84
5.3	Spectral Analysis.....	86
5.4	Conclusions	88
Chapter 6. Conclusion.....		89
6.1	Summary	89
6.2	Future Works.....	90
REFERENCES		92
Appendix A – Extra Figures		97
Appendix B – Matlab Codes.....		107
B1.	Identifying Possible Critical Points	107
B2.	Determining Type of Critical Point	110
B3.	Calculating Track Velocities	112

List of Figures

Figure 1. The view of a two-dimensional turbulent boundary layer separation with reversed flow. The dashed line in the figure indicates where the mean streamwise velocity is zero ($\langle U \rangle = 0$). Figure taken with permission from Simpson (1989).	6
Figure 2. The surface topology of separated flow over a cube. Taken with permission from Depardon <i>et al.</i> (2005).	9
Figure 3. Classification of singular points in the p - q plane. Taken with permission from Déleroy (2013).	10
Figure 4. The convergence of skin-friction lines indicate a detachment, while the divergence of streamlines indicate an attachment to the surface.	11
Figure 5. The surface topology of separated flow over a cube. Taken with permission from Déleroy (2013).	12
Figure 6. <i>a</i>) A surface pattern of an airfoil with one stall cell and <i>b</i>) two stall cells.	13
Figure 7. Surface patterns on the suction side of a NACA 0012 airfoil at <i>(a)</i> $\alpha = 0^\circ$, <i>(b)</i> 5.0° , <i>(c)</i> 13.5° , and <i>(d)</i> 16.0° . Taken with permission from Liu <i>et al.</i> (2011).	16
Figure 8. A basic schematic of a time-resolved planar PIV setup for investigating the flow inside a channel.	23
Figure 9. The scattering cross section as a function of particle diameter and wavelength of incident light. Figure taken from Melling (1997).	25
Figure 10. The light scattering pattern from a $1 \mu\text{m}$ oil droplet. Figure taken from Raffel <i>et al.</i> (2018).	25
Figure 11. The three main steps of vector cross correlation for two single-exposure frames.	26
Figure 12. The Hanning, Hamming, Kaiser4, and Blackman window function with a length of 128 elements.	29
Figure 13. The distribution of weighting for a Hanning window with $M = 128$ over 640 data points with <i>(a)</i> no overlap, <i>(b)</i> and 50% overlap.	30
Figure 14. A model of the closed-loop wind tunnel in the Mechanical Engineering building at University of Alberta.	31
Figure 15. A comparison of the original NACA 4418 airfoil and the new profile that contains a flat section in the rear 23% of the chord.	32

Figure 16. The lift-coefficient curve of the NACA 4418 airfoil at different Reynolds number (Abbott & Von Doenhoff 1959). Taken with permission.....	34
Figure 17 (a) Schematic of the tuft installation and (b) flow visualization of the trailing-edge separation with tufts.....	35
Figure 18. Schematic of the PIV setups for experiment I. The coordinates are defined relative to the flat surface of the airfoil. The origin of the coordinate system (O) is located at the separation point at mid-span and 140 mm ($0.14c$) upstream of the trailing edge. Note that the axes are displaced from mid-span of the airfoil for clarity of the figure.	36
Figure 19. Statistical convergence of the (a) second-order and (b) third-order moments. The results shown here are for a sample point located at $(x, y) = (10, 25)$ mm.	38
Figure 20. Convergence test of the advection velocities and speed for saddle points.....	41
Figure 21. A schematic of the PIV setup for experiment II highlighting the location of the actuators and PIV cameras. The dimensions of the airfoil including the chord length (c), span (s), and length of the flat section (l) are the same as experiment I. The actuators are located 168 mm ($0.17c$) from the trailing edge of the airfoil (d).....	42
Figure 22. (a) Top view of the actuator array and (b) sectional view highlighting the placement of actuators. Two different signals, A and B, are fed to the ten actuators. The width, w , and height, h , of each actuator flaps are 20 mm and 30 mm respectively. The free length, L_f , of the actuator is 28 mm. Note that the L_f and h are slightly different.....	44
Figure 23. Dynamic response of the piezoelectric actuator with a 20×30 mm ² steel sheet mounted on top. The displacement here is defined as the amplitude, i.e., the maximum displacement from the off position.	45
Figure 24. (a) Vectors of mean velocity at various chordwise positions upstream and downstream of the mean separation point ($x/c = 0$). The vector profiles are shown in $0.05c$ increments and the vectors are downsampled by a factor of 6 in the y -direction for clarity of the visualization. Contours of the normalized mean streamwise velocity, $\langle U \rangle / U_\infty$, are shown in the background. Positive contours are above the dashed line and negative contours are located under the dashed line. (b) Contour lines of the backflow parameter (γ) in the x - y plane. The dashed line indicates where the mean streamwise velocity is zero.....	50

Figure 25. Contours of (a) streamwise (b) and wall-normal Reynolds stresses, and (c) Reynolds shear stress in the x - y plane. The dashed line shown in the figures indicates $\langle U \rangle = 0$. The values are normalized using the freestream speed of the wind tunnel U_∞ 53

Figure 26. Contours of the third-order central moments (a) $\langle u^3 \rangle / U_\infty^3$ and (b) $\langle u^2 v \rangle / U_\infty^3$ in the x - y plane. The turbulence transport terms are normalized by the freestream speed of the wind tunnel U_∞ . The dashed line shown in the figures indicates $\langle U \rangle = 0$. Contours enclosed with solid lines denote negative values and contours without solid borders denote positive values. 54

Figure 27. (a) Streamlines obtained from the mean flow in the near-surface ($y = 2$ mm) plane. Colors in the background represent the mean streamwise velocity normalized by freestream speed of the wind tunnel U_∞ . The positive and negative contours can be identified based on the streamwise direction of the streamlines. (b) Contour lines of the backflow parameter (γ) in the near-surface plane, showing intermittency of the separated flow..... 55

Figure 28. Contours of (a) streamwise and (b) spanwise components of Reynolds normal stress, and (c) Reynolds shear stress in the x - z plane. The near-surface streamlines obtained from the mean flow are superimposed on the contours. The negative contours are shown with solid black outlines..... 57

Figure 29. Power spectral density (PSD) of the fluctuating (a) streamwise and (b) spanwise velocity at a location upstream of the mean separation point ($x/c = -0.05$), at the saddle point ($x/c = 0$), and a point in the backflow region ($x/c = 0.05$) along mid-span ($z = 0$). 58

Figure 30. Snapshot of the instantaneous near-surface streamlines with a background contour of (a) normalized streamwise velocity and (b) two-dimensional Q -criterion. The sign of the contours in (a) can be identified using the streamwise direction of the streamlines. 60

Figure 31. Filtered streamlines of the instantaneous velocity field in Figure 30 with (a) instantaneous streamwise velocity and (b) two-dimensional Q -criterion shown in the background. A moving average filter with cutoff frequency at $St = 0.05$ was applied. Once again, the color of the contours in (a) can be identified through the streamwise direction of the streamlines. 62

Figure 32. (a) Visualization of the detected tracks of saddle points, clockwise foci, and counter-clockwise foci over 1.0 s. Saddle points, clockwise foci, and counter-clockwise foci are shown with black, medium gray (green), and light gray (yellow) tracks, respectively. Tracks shown in the figures have a minimum length of 25 frames (0.014 s). The lower two plots show projections

of the locations of the (b) saddle points and (c) foci obtained from 2.5 s of time-resolved data onto the x - z plane.	65
Figure 33. The formation and dissipation of (a – d) a forward stall cell and (e – h) a backward stall cell due to local concentrations of strong streamwise momentum. The colors in the background correspond to the normalized streamwise velocity.	67
Figure 34. Probability density functions (PDFs) of the spanwise wavelength of high-speed streaks (λ_z/s) at three different chordwise positions. The wavelengths were determined by spatial autocorrelation of the fluctuating streamwise velocity using Eq. (4.1) and were fitted with a lognormal distribution.	68
Figure 35. (a) Isosurfaces of the fluctuating streamwise velocity corresponding to $u/U_\infty = 0.12$. (b) The isosurfaces projected onto the x - t axis to highlight the advection velocity of streaks in the streamwise direction.	70
Figure 36. The energy content of the first 100 POD modes in the x - z plane of FOV2.	71
Figure 37. The first six POD modes obtained from decomposition of the fluctuating velocity field. Contours of the fluctuating streamwise velocity are shown in the background.	72
Figure 38. Low-order flow fields obtained by superimposing a selected spatial mode with the mean velocity field. The temporal amplitudes a_i are chosen based on the RMS value of the amplitudes associated with the respective mode. The background contours correspond to the normalized streamwise velocity.	74
Figure 39. Mean velocity field of the near-wall flow with piezoelectric actuators at rest. The background contour correspond to the streamwise component of the near-wall velocity vectors.	80
Figure 40. Mean velocity field of the near-wall flow with actuating frequencies between 50 and 225 Hz under the two-dimensional control mode. The background contour correspond to the streamwise component of the near-wall velocity vectors.	81
Figure 41. Mean velocity field of the near-wall flow with actuating frequencies between 50 and 225 Hz under the three-dimensional control mode. The background contour correspond to the streamwise component of the near-wall velocity vectors.	82
Figure 42. The backflow interface identified by points where $\langle U \rangle = 0$ for the (a) two-dimensional and (b) three-dimensional actuation mode. The location of the ten actuators are shown relative to the backflow interfaces.	83

Figure 43. (a) Streamwise Reynolds normal stresses ($\langle u^2 \rangle$), (b) spanwise Reynolds normal stresses ($\langle w^2 \rangle$), and (c) Reynolds shear stresses ($\langle uw \rangle$) for the no actuation case, two-dimensional actuation at 225 Hz, and three-dimensional actuation at 225 Hz. 85

Figure 44. Power spectral density of the fluctuating streamwise velocity, u , for the (a) two-dimensional and (b) three-dimensional actuation mode at 225 Hz. The PSDs are obtained from points $x/c = 0.01, 0.05, 0.10,$ and 0.15 at $z/c = 0$ (midspan). 86

Figure 45. Power spectral density of the backflow ratio (Γ) for the separated flow with no flow control and two- and three-dimensional actuation at 225 Hz. 87

List of Tables

Table 1. Two-dimensional studies of flow separation and their method of maintaining two-dimensionality in the flow.	7
Table 2. Classification of different types of actuators for suppressing flow separation (Cattafesta & Sheplak 2011).	18
Table 3. Boundary layer parameters for various positions upstream of and at mean separation.	51
Table 4. Advection velocities and speed of saddle points and foci evaluated based on the tracks detected in five sets of filtered time-resolved data.	64

Nomenclature

Symbol	Definition
$ \dots $	Magnitude of enclosed parameter
$\langle \dots \rangle$	Time-averaged quantity of enclosed parameter
a_m	Temporal amplitude of spatial mode m from POD
c	Chord length of airfoil
d_a	Tip displacement of actuator measured from rest
f_a	Actuating frequency of piezoelectric actuator
H	Boundary layer shape factor
P	Fluid pressure
Re	Reynolds number
s	Span of airfoil
St	Strouhal number
U	Instantaneous streamwise velocity
u	Fluctuating streamwise velocity
U_∞	Freestream speed
V	Instantaneous wall-normal velocity
v	Fluctuating wall-normal velocity
W	Instantaneous spanwise velocity
w	Fluctuating spanwise velocity
x	Streamwise direction
y	Wall-normal direction
z	Spanwise direction
α	Airfoil pitch angle, also referred to as angle-of-attack
γ	Backflow parameter
δ^*	Boundary layer displacement thickness
δ_{99}	Boundary layer thickness
θ	Boundary layer momentum thickness
λ_z	Spanwise wavelength of high-speed streaks
μ	Dynamic viscosity of fluid
ρ	Density of a fluid or particle
τ	Local wall shear stress
φ_m	Spatial mode m from POD

Acronym	Definition
APG	Adverse Pressure Gradient
CW	Clockwise direction
CCW	Counter-clockwise direction
FFT	Fast-Fourier Transform
FOV	Field of View
ID	Incipient detachment ($\gamma = 0.99$)
ITD	Intermittent Transitory Detachment ($\gamma = 0.80$)
NACA	National Advisory Committee for Aeronautics
PIV	Particle Image Velocimetry
PSD	Power spectral density
PDF	Probability Density Function
POD	Proper Orthogonal Decomposition
ZPG	Zero Pressure Gradient

Chapter 1. Introduction

1.1 Motivation

The separation of a turbulent boundary layer is defined as the breakdown of boundary layer flow, which is typically accompanied with wall-normal motion and reversed flow (Simpson 1989). This thesis is concerned with flow separation that is caused by an adverse pressure gradient (APG) in the streamwise direction. The phenomenon is potentially observed in flow over airfoils, blades of a wind turbine, and within diffusers at moderate to high angles of attack. In engineering, flow separation is typically linked to a decrease in performance of the fluid device (Simpson 1989); a stalled airfoil contain significantly less lift and more drag than an airfoil operating under normal condition. The unsteady nature of the wake due to separation can also introduce unwanted structural vibrations. Understanding the mechanics of flow separation will allow engineers to develop methods to delay separation, thus improving the performance and reliability of high-lift devices. In many engineering applications, the peak performance of a device is located at the brink of separation; an airfoil achieves highest lift just before the stall angle of attack. Predicting flow separation with computational fluid dynamics is difficult due to high turbulence intensity and sensitivity to upstream conditions (Angele & Muhammad-Klingmann 2006).

This project is broken down into two different parts. First, the unsteady three-dimensional topology of an intermittent separation is characterized through high-speed particle image velocimetry (PIV). This will be referred to as ‘experiment I’ in the thesis. Second, the effects of piezoelectric actuators upstream of the mean separation front on the near-wall topology and turbulence statistics are analyzed. This portion will be denoted as ‘experiment II’ in the presented thesis. Separated flow was created by operating a thick two-dimensional airfoil at a pre-stall angle of attack inside a wind tunnel facility located at the University of Alberta Mechanical Engineering building.

1.2 Thesis Outline

The thesis is written as a paper-based thesis with the following chapters:

- Chapter 2 is a literature review of investigations regarding flow separation, active methods of flow control, PIV, and advanced analysis techniques used in this project. The latter include proper orthogonal decomposition and Welch's power spectral density estimate.
- Chapter 3 contains a detail overview of the experimental setup including the wind tunnel facility, airfoil model, and various PIV setups.
- Chapter 4 contains the results of a published paper on the unsteady topology of an airfoil with trailing-edge separation. The content contains characterization of the unsteady topology and a discussion of the connection between separation structures and surrounding flow conditions.
- Chapter 5 is a parametric study on the effects of flapping piezoelectric actuators on near-wall topology and turbulence statistics.
- Chapter 6 is a brief summary of the current work with suggestions for future improvements.

Chapter 2. Background

This chapter is review on literature regarding experimental studies of APG-induced flow separation and control of flow separation. The working principle of two-dimensional PIV and advance analytical techniques such as proper orthogonal decomposition (POD) and Welch's overlapped segmented average is also covered in the latter portion of the chapter.

In this thesis, the x -, y -, and z -directions are the streamwise, wall-normal, and spanwise directions, respectively. The parameters U , V , and W presented in this thesis are defined as the instantaneous velocity in the x -, y -, and z -directions, respectively, while u , v , and w are the fluctuating velocity components. The symbol $\langle \dots \rangle$ represents the temporal average of the enclosed parameter.

2.1 Boundary Layer Separation

In this section, the characteristics of both two-dimensional and three-dimensional separation will be reviewed. In addition, the critical point theory, which is a mathematical theory used to analyze trajectory curves on a plane, will also be reviewed. This theory is applied to skin-friction lines to study the topology of three-dimensional separation.

Flow separation is defined as the departure of boundary-layer flow accompanied with large wall-normal motion (Simpson 1989). Separation can be caused by an abrupt change of the surface geometry or by the presence of an adverse pressure gradient (APG) (Alving & Fernholz 1996). An adverse pressure gradient is defined for a pressure field where the static pressure increases in the direction of the boundary layer flow ($dP/dx > 0$). If the strength of the adverse pressure gradient is strong enough, the boundary will detach from the surface and result in a region of reversed flow. Unlike separation due to geometry, APG induced separation is strongly dependent on the Reynolds number (Alving & Fernholz 1996). The detached flow can also reattach depending on the strength of APG (Alving & Fernholz 1996).

2.1.1 Two-Dimensional Separation

Similar to many other areas of fluid mechanics, the investigation of flow separation began with the simplest case: two-dimensional flow. The flow for two-dimensional separation is limited to only the streamwise-wall-normal plane. Since the fluid is unable to escape in the spanwise

direction, two-dimensional separated flow will lead to a closed recirculation bubble. Two-dimensional separations do not exist in nature due to sensitivity of the flow to many surrounding parameters (Moss & Murdin 1970; Gregory *et al.* 1971; Winkelman & Barlow 1980).

Creating a full two-dimensional flow separation in a controlled laboratory environment such as a wind tunnel is difficult due to the interference of sidewalls. A summary of existing studies on two-dimensional flow separation and their method of eliminating spanwise variation is shown in Table 1. Initially, researchers tried to achieve two-dimensionality by introducing suction or blowing along the walls (Coles & Wadcock 1978; Gregory *et al.* 1971), but they were unsuccessful. Gregory *et al.* (1971) determined that separation occurred earlier (i.e. mean separation point is located more upstream) at the sidewalls for an airfoil with no leading-edge separation. The corner separations direct the near-surface flow toward the mid-span, resulting in three-dimensionality. Suction along the wall was successful in removing corner separations, but three-dimensionality remained. Some time later, researchers were able to force a two-dimensional separation through implementation of flow guides along the sidewalls (Coles & Wadcock 1978; Thompson & Whitelaw 1985; Wadcock 1987). Confirmation of two-dimensionality was mostly achieved through either surface oil flow visualization or surface pressure profiles. Both these techniques reveal little about the flow's unsteadiness (Lu 2010). Consequently, it is difficult to say whether the separation in some of these studies was truly two-dimensional.

The separation point is typically associated with the location on the surface where reverse flow first occur in the mean velocity field. However, this is only true in all cases for a steady, two-dimensional separation (Simpson 1989). It is possible for flow to separate without the occurrence of backflow in three-dimensional flow. Through the perspective of two-dimensional flow, the velocity of the fluid is limited to the streamwise-wall-normal plane, meaning fluid is unable to escape in the spanwise direction in the presence of an APG. As a result is trapped within a recirculation zone (Délery 2013).

For unsteady flow, it is impossible to define one point on the surface as the definitive point of separation due to intermittency of the flow. Consequently, Simpson (1981) proposed the backflow parameter γ_{pu} to characterize the flow, which is defined as the fraction of time that the flow is downstream. Using the backflow parameter, Simpson (1981) described a two-dimensional separation as the likeliness of backflow increased with streamwise distance. This description is shown in Figure 1. Separation begins at the incipient detachment (ID), which equates to the point

on the surface where the flow is downstream 99% of the time. Intermittent transitory detachment (ITD) corresponds to the point where $\gamma_{pu} = 0.80$; transitory detachment is located where flow reversal occur half the time ($\gamma_{pu} = 0.50$). In two-dimensional steady flow, the transitory detachment point (D) is coincident with the location of zero shear stress and the start of flow reversal.

Despite uncertainties around the two-dimensionality of experiment, majority of previous studies were focused on characterization of the separation along the streamwise-wall-normal plane at mid-span (Angele & Muhammad-Klingmann 2006; Coles & Wadcock 1978; Holm & Gustavsson 1999; Wadcock 1987). As the flow approaches the APG, the boundary layer profile lose the fullness that is observed in a zero pressure gradient turbulent boundary layer. The shape factor is defined as the ratio between the displacement and momentum thickness of a boundary layer. It can be evaluated to identify the state of the boundary layer – whether it is laminar or turbulent. Past experiments show that shape factor of the boundary layer ranges from 3.40 to 3.45 at the mean detachment point (Angele & Muhammad-Klingmann 2006; Holm & Gustavsson 1999). Castillo *et al.* (2004) predicted a shape factor of 2.76 at separation using the momentum boundary layer equations, which is similar to the value determined by Dengel & Fernholz (1990). The value provided by Castillo *et al.* (2004) is a prediction for the ITD point, which occurs sooner than the detachment point measured from a time-averaged flow field. According to Thompson & Whitelaw (1982), the standard log law of the wall is applicable in the near-wall region before separation, but the height of the logarithmic region decrease as the flow approach separation. The peak Reynolds stress is located near the wall upstream of separation and deflect outward in a boundary layer with APG downstream (Angele & Muhammad-Klingmann 2006; Simpson 1989; Thompson & Whitelaw 1985). This observation is attributed to separation of the shear layer from the surface.

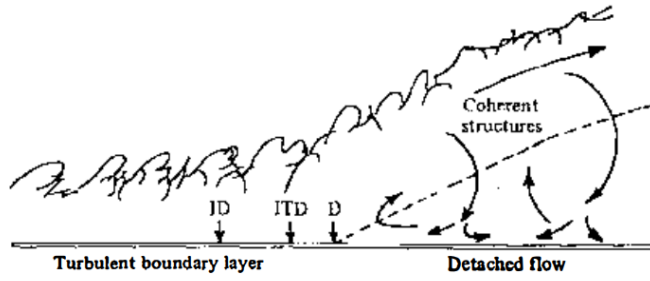


Figure 1. The view of a two-dimensional turbulent boundary layer separation with reversed flow. The dashed line in the figure indicates where the mean streamwise velocity is zero ($\langle U \rangle = 0$). Figure taken with permission from Simpson (1989).

Table 1. Two-dimensional studies of flow separation and their method of maintaining two-dimensionality in the flow.

2D Separation	Description	Reynolds Chord Number	Corner Control	2D Verification Method	Results
Gregory <i>et al.</i> (1971)	Thick and thin airfoil study using surface oil flow visualization (SOFV)	$0.85 - 1.7 \times 10^6$	Suction along the wall	SOFV	Eliminated corner separation but 3D pattern remained.
Cole & Wadcock (1979)	Flying hot-wire measurements over NACA 4412 airfoil in boundary layer, separated, and near wake region. It is assumed measurements are taken at mid-span.	1.5×10^6	Flow guides/suction	Surface pressure measurements at different span location	Similar surface pressure distribution at $\frac{1}{4}$ -span, $\frac{3}{4}$ span, and mid-span.
Thompson & Whitelaw (1985)	Various measurements (hot-wire, pressure probes) over flat plate with a trailing flap.	2.6×10^6	Flow guides	SOFV, pressure and local velocity measurements	Pressure distribution, mean velocity, and Reynold stresses were consistent within experimental error over 90% of the span.
Wadcock (1987)	Three-component laser velocimetry at the boundary layer region and wake of a NACA 4412 airfoil.	1.64×10^6	Flow guides around leading edge	Surface pressure measurements at different span location	Measured near identical surface pressure distribution at three different spanwise location.

2.1.2 Three-Dimensional Separation

The importance of studying 3D separation comes from the fact that flow is never completely two-dimensional in both nature and laboratory environment because of boundary conditions. Three-dimensional separation can occur even with a two-dimensional setup. For example, the flow over a 2D airfoil with separation results in a three-dimensional flow due to corner vortices and the wall boundary layer (Broeren & Bragg 2001).

Unlike two-dimensional separation, the separation point is identified by a saddle point with converging skin-friction lines on the surface. The curve that nearby skin-friction lines converge toward is the separation line. Skin-friction lines are defined as lines on the surface with their slope parallel to the local wall shear-stress, τ (Délery 2013). The skin-friction lines are characterized mathematically by

$$\frac{dx}{\tau_x(x, z)} = \frac{dz}{\tau_z(x, z)}. \quad 2.1$$

where the x -, and z -coordinates are the streamwise and spanwise direction respectively. If the fluid is Newtonian, then skin-friction lines are also known as limit streamlines because they correspond to the limit of streamlines as they approach the wall (Délery 2013).

Historically, the skin-friction lines can be obtained qualitatively with the use of surface oil flow-visualization technique. The skin-friction pattern shown in Figure 2 is for separated flow around a cube (Depardon *et al.* 2005). The patterns produced from surface oil is a depiction of the mean flow due to long response time of the technique (Lu 2010). Surface pattern measurements can also be measured by 2D PIV over a near-surface plane. The measurement plane must be sufficiently close to the surface to minimize both positioning and structural discrepancies (Depardon *et al.* 2005). In some setups, this may be difficult due to the reflection of light coming from the surface, thus disrupting the process of cross-correlation. The benefits of using PIV include increased spatial resolution and the capability of measuring the instantaneous skin-friction pattern. In addition, PIV measurements are quantitative thus removing the need for human interpretation, which may be subjective when the pattern becomes more complex. Tufts have also been used to obtain an imprecise outline of the separation line (Manolesos *et al.* 2014).



Figure 2. The surface topology of separated flow over a cube. Taken with permission from Depardon *et al.* (2005).

2.1.3 Critical Point Theory

Critical point theory is a mathematical tool used to study integral curves on a plane. It was first developed by mathematician Henri Poincaré (1928). The theory is applied here to the concept of skin-friction lines to study the topology of a three-dimensional separation.

The topology of the separated flow around a three-dimensional object is characterized through singular points in the surface pattern. Singular points are located where the skin friction is null. There exist three types of singular points: nodes, foci, and saddle points. Classification of singular points is achieved by using the equation

$$S^2 + pS + q = 0, \text{ where} \quad 2.2$$

$$p = -\left(\frac{\partial \tau_x}{\partial x} + \frac{\partial \tau_z}{\partial x}\right), \text{ and} \quad 2.3$$

$$q = \frac{\partial \tau_x}{\partial x} \frac{\partial \tau_z}{\partial z} - \frac{\partial \tau_z}{\partial x} \frac{\partial \tau_x}{\partial z}. \quad 2.4$$

The roots of equation 2.2, S , is used to identify the type of critical point present (Délery 2013). The three different types of singular points are shown on the p - q plane in Figure 3. Two real roots with the same sign indicate a node is present; two complex roots shows a focus point, and two real roots with opposite signs reveal a saddle point.

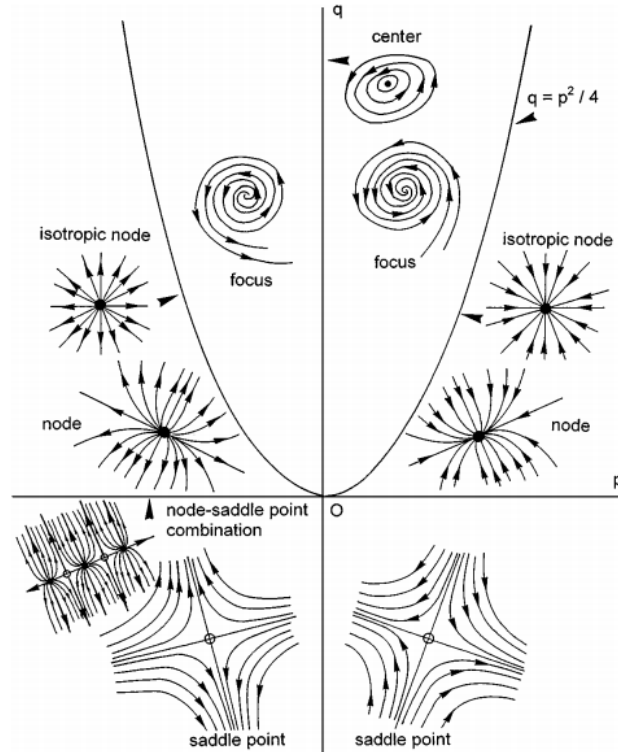


Figure 3. Classification of singular points in the p - q plane. Taken with permission from Détery (2013).

The node is a point on the surface where all skin-friction lines intersect with a common tangent except for one skin-friction line. The node is either an attachment or detachment type depending on the direction of the lines coming out of the node. An attachment node contains skin-friction lines emerging from the singular point, while a detachment node consists of lines entering the point. Attachment nodes that exist on a forward-facing surface are typically a stagnation point (Tobak & Peake 1982).

The second type of singular point is the focus, which features a point where nearby skin-friction lines spiral and converge into it. Foci are similar to nodes in the sense that they both act as a source or sink for skin-friction lines (Tobak & Peake 1982), i.e., skin-friction lines must begin at a node/focus and then disappear at a node/focus. The motion attributed to a focus is similar to a tornado; fluid is pulled towards the focus point and away from the surface through a spiral motion.

The final singular point is the saddle point. According to Tobak & Peake (1982), all separated flows contain at least one saddle point in their friction pattern. The saddle point has two skin-friction lines that intersect the point that are known as separatrices in mathematical terminology. One of the separatrices is aligned with the upstream flow while the second separatrix is either a

separation or attachment line. This is dependent on whether nearby skin-friction lines diverge or converge away from the separatrix. The convergence of skin-friction lines along the separatrix corresponds to flow detachment while the divergence of skin-friction lines indicate attachment. As shown in Figure 4, the convergence of streamline imply a vertical dilation of the streamtube, which implies fluid leaving the surface. On the contrary, the divergence of skin-friction lines would imply flow diving towards the surface due to vertical contraction of the streamtube. The separation line extends into the flow, creating a separation surface as shown in Figure 5. The separation surface act as a barrier that separates upstream and downstream streamlines. Based on topological constraint, the number of nodes and foci subtracted by the total number of saddle points is two for a simple three-dimensional body with no holes.

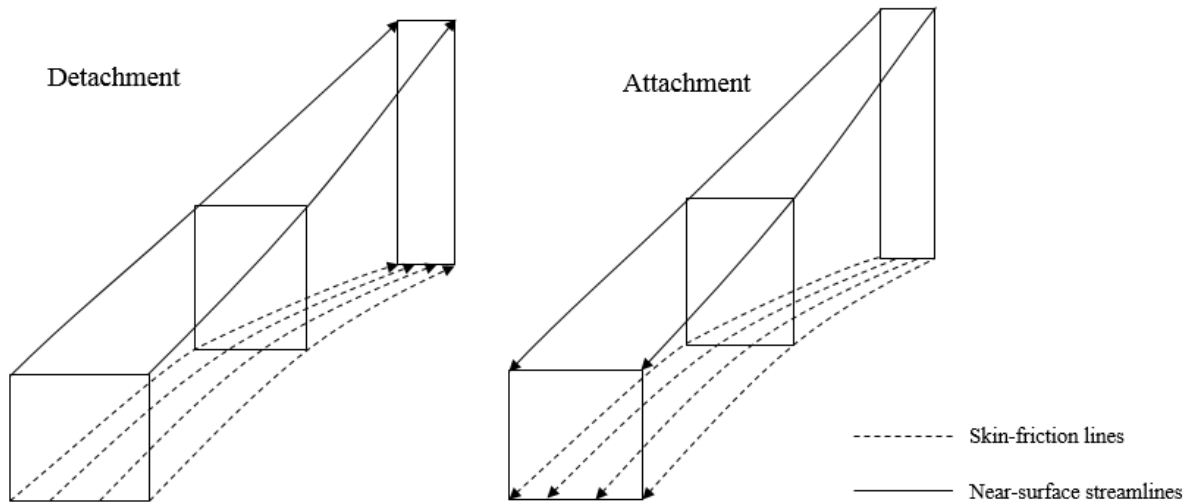


Figure 4. The convergence of skin-friction lines indicate a detachment, while the divergence of streamlines indicate an attachment to the surface.

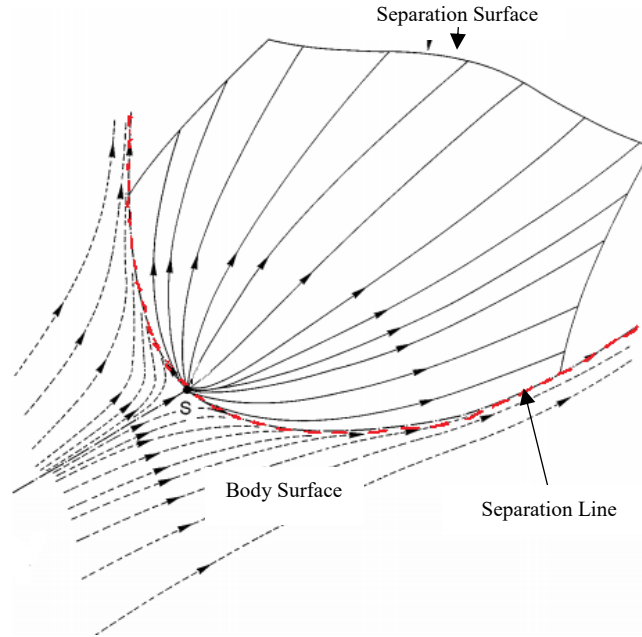


Figure 5. The surface topology of separated flow over a cube. Taken with permission from Délery (2013).

In the previous section, it was mentioned that the convergence of skin-friction lines is associated with flow detachment while divergence is associated with attachment. It should be noted that this postulate is not universally accepted in the study of flow separation (Tobak & Peake 1982). Thus far, there is one documented scenario where the convergence of skin-friction lines from a saddle point is actually produced by flow attachment: the laminar vortex structure upstream of a cylinder-wall juncture (Visbal 1991). In a recent investigation, Zhang *et al.* (2012) confirmed with PIV measurements that the saddle point with converging skin-friction lines for flow separation upstream of a cylinder juncture is actually an attachment point. While surface patterns have been used frequently to study the topology of separated flow, this is the only reported scenario where a saddle point with converging skin-friction lines indicated flow attachment.

Investigation of 3D separation is achieved by assigning topology to basic surface patterns observed in separated flow. Complex separation patterns are constructed of four elementary patterns: saddle – node, saddle – focus, saddle – limit cycle, and limit cycle (Surana *et al.* 2006). A limit curve is defined as a closed curve where nearby skin-friction lines spiral into or around it. The former two, which involves a separation line starting at a saddle and then terminating at a node or focus, are known as closed or global separations. Originally, it was believed that only closed separations are physical (Lighthill 1963; Surana *et al.* 2006). The existence of open

separation has been confirmed by Wang (1972) who initially termed this type of detachment as crossflow separation.

2.1.4 Airfoil Stall and Stall Cells

The separation pattern over a stalled airfoil is dependent on many parameters. The selected profile along with the angle of attack determines the type of separation that will occur over the airfoil. Airfoils with a moderate thickness typically contain a leading-edge stall once the critical angle of attack has been reached. As a result, a saddle point structure is expected at the leading edge of the airfoil. An airfoil with a thickness ratio greater than 0.15 typically display a trailing edge stall (McCullough & Gault 1951) where its most upstream saddle point will be located in the aft section of the airfoil. The flow topology over a stalled airfoil is also dependent on how the airfoil is mounted to the wind tunnel, the aspect ratio, and the type of trip wire used (Liu *et al.* 2011). For a wall-mounted airfoil, the wall boundary layers can introduce three-dimensional effects into the separated flow. An airfoil mounted only with supports contain tip vortices that can also alter the surface pattern on both the pressure and suction side. Because the flow is sensitive to a large quantity of parameters, surface pattern over a stalled airfoil is typically complicated and involve large number of singular points.

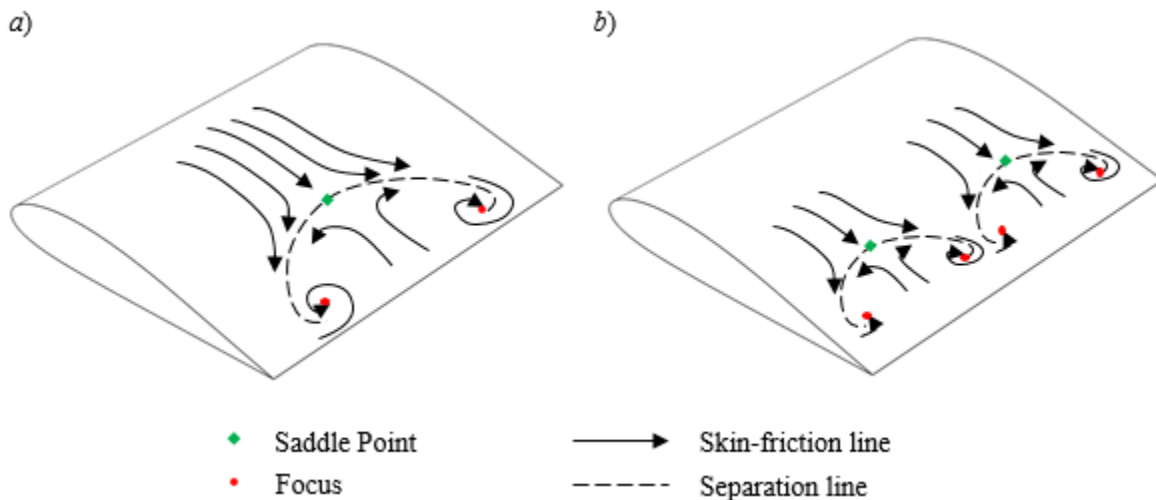


Figure 6. *a)* A surface pattern of an airfoil with one stall cell and *b)* two stall cells.

One distinguished pattern, which is also the focus of the present thesis, is known as stall cell. Stall cells are large-scale three-dimensional structures that can be observed over the suction side of a stalled rectangular planform wing where the ends are flush with the walls (Broeren & Bragg

2001). The skin-friction pattern of a stall cell is characterized by a saddle point with the ends of the separation line terminating at a pair of counter-rotating foci, as depicted in Figure 6. The pattern is also called the “owl-faced” or mushroom-shaped pattern due to its appearance. This phenomenon can occur over an airfoil model with trailing-edge separation (Manolesos *et al.* 2014) or leading-edge separation (Yon & Katz 1998). Multiple stall cells can appear on the skin-friction pattern. Both Winkelmann & Barlow (1980) and Yon & Katz (1998) established that the number of cells present on an airfoil increase with growing aspect ratio. Manolesos & Voutsinas (2014a) discovered that the distance between the pair of counter rotating foci increase with angle of attack and Reynolds number.

The three-dimensional topology of stall cells have been briefly investigated in the past. As a preliminary study, Winkelmann & Barlow (1980) came up with a tentative model of the three-dimensional topology for stall cell patterns. They hypothesized that the two foci that appears on the surface are created by a spanwise vortex that connects one focus to the other, which they called the loop vortex. There is also a secondary spanwise vortex at the trailing-edge of the airfoil that rotate in the opposite direction of the loop vortex. Based on this topology, Weihs & Katz (1983) created a theoretical model relating the number of stall cells that appear on the surface pattern to the aspect ratio of the wing. The model was developed based on the assumption that stall cells are vortex rings generated from the instability of spanwise vortices from the separated shear layer. After a brief period, Yon & Katz (1998) discovered the model suggested by Winkelmann & Barlow (1980) was inconsistent with their experimental data. Instead, they suggested that the two foci on the surface corresponds to two separate counter-rotating vortices that start in the wall-normal direction and then extend downstream into the wake in the streamwise direction. This was later validated by Manolesos & Voutsinas (2014b) and Ragni & Ferreira (2016) through stereoscopic PIV measurements. Two spanwise vortices were also observed by Manolesos & Voutsinas (2014b): one located at the separation line and another at the trailing edge. The two spanwise vortices rotated in opposite directions relative to each other.

2.1.5 Leading-Edge Separation

Liu *et al.* (2011) investigated the surface pattern of a NACA 0012 airfoil with leading-edge separation. The airfoil was mounted with supports and the sides of the airfoil was exposed so that tip vortices could be formed. Figure 7 shows the transformation of skin-friction lines on the suction

side of the airfoil as the flow changed from attached to a full leading-edge separation. As expected, no singular points are present in the skin-friction lines of the fully attached flow shown in Figure 7a. The skin-friction lines reveal an influx of flow from the pressure side through tip vortices. As the angle of attack is changed to 5.0° , the surface pattern remained free of saddle points. The first saddle point is observed at an angle of 13.5° , indicating that separation first occurs at 13.5° . The flow quickly reattaches as indicated by the attachment type saddle point in Figure 7c. At an angle of attack of 16.0° , the flow is fully separated resulting in a more complex topology. The pattern features five saddle points and a pair of foci on each side of the airfoil. The saddle point S1 in Figure 7d reveals a leading-edge separation. Due to the influence of tip vortices, the separation line rolls into a focus.

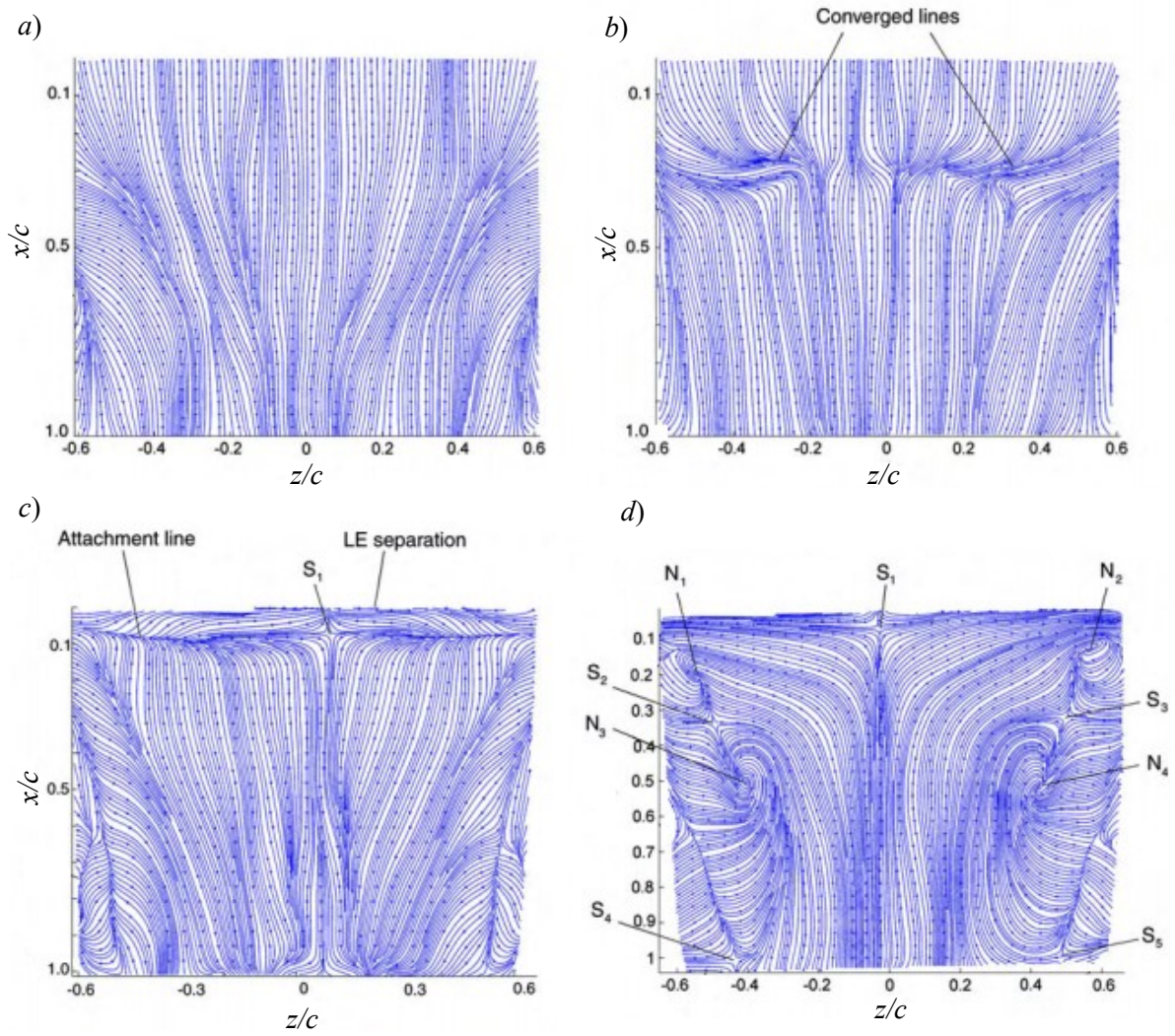


Figure 7. Surface patterns on the suction side of a NACA 0012 airfoil at (a) $\alpha = 0^\circ$, (b) 5.0° , (c) 13.5° , and (d) 16.0° . Taken with permission from Liu *et al.* (2011).

2.2 Control of Flow Separation

The following section cover common methods of suppressing an APG-induced separation. The distinction between different methods of passive and active flow controls will be briefly discussed. A detail review on the use of piezoelectric actuators for flow control will be conducted, because piezoelectric actuators will be used to delay suppression in this project.

2.2.1 Passive Flow Control

Passive flow control are techniques for suppressing flow separation that involves a slight modification or addition to the geometry of the flow device. Some methods of passive flow control include grooves, porous surfaces, and vortex generators (Lin *et al.* 1989). These devices are more practical because they are easily implemented with a slight change in geometry and do not require a power source. For this reason, they have been widely used on aircrafts.

Utilization of grooves or pores on the surface of an object for suppression of separation can be seen in both engineering design and nature. Dimples on golf ball pushes the separation point on the spherical body further back, thus reducing the pressure drag induced by the wake region. The flippers on a humpback whale contains large rounded protuberances on the leading edge that prevent separation, effectively reducing the drag as it swims underwater (Fish & Lauder 2006).

Vortex generators typically consist of a pair of vanes mounted in a V-shape with the two ends facing the upstream direction. However, unconventional shapes such as wishbone, doublet or ramp have also been looked at (Wang & Ghaemi 2019). The effectiveness of different types of vortex generators has been briefly investigated. Vortex generators, as its name suggests, induce vortices that transfers momentum from the outer flow regime to the near-wall region (Schubauer & Spangenberg 1960). The increase in momentum of the near-wall flow encourages the flow to remain attached to the wall over a longer distance, thus delaying separation.

2.2.2 Active Flow Control

Active flow control is the suppression of flow separation by using actuators, typically by introducing momentum into the surrounding flow (Cattafesta & Sheplak 2011). Although active flow controls are more difficult to implement compared to passive methods, they can be utilized in a closed-loop control system to optimize flow separation under changing conditions. The most

common actuators are classified based on the method that they supply momentum to the surrounding fluid: fluidic, moving object/surface, and plasma actuators. Further classification of these categories are shown in Table 2. Less common types of actuators include electromagnetic or magnetohydrodynamic.

Table 2. Classification of different types of actuators for suppressing flow separation (Cattafesta & Sheplak 2011).

Fluidic jets	Moving object/surface	Plasma	Other
Zero-net mass flux	Vibrating ribbon	Corona discharge	Electromagnetic
Nonzero mass flux	Vibrating flap	Dielectric barrier discharge	Magnetohydrodynamic
	Oscillating wire	Local arc filament	
	Rotating surface	Sparkjet	
	Morphing surface		

The most common type of actuators for flow control are fluidic jets. These actuators utilizes the injection or suction of fluid to suppress or delay separation. The process can be repeated in a uniform or oscillatory manner (Moghaddam & Neishabouri 2017). Fluidic jet actuators are further classified by whether or not an external mass sink/source is used for the injection or suction of fluid. Zero-net mass flux are fluidic actuators that expel or pull in the working fluid only while nonzero mass flux actuators involves the injection or expelling of an external fluid. The second category contains actuators that contains movement of the surface or a mounted object in an oscillating manner. Few examples of moving object/surface actuators include a vibrating flap, oscillating wire, or a rotating rod. The motion of the moving object/surface supply momentum to the near-wall flow. The last category contains plasma-type actuators. In a plasma actuator, plasma is created through a high-frequency, high-voltage alternating current across a pair of electrode, which supply momentum into the surrounding flow by ionizing the nearby fluid (Corke *et al.* 2010; Gregory *et al.* 2007).

2.2.3 Piezoelectric Actuators for Flow Control

Piezoelectric actuators are actuators of the vibrating flap type; they deform when a voltage is supplied to it. As a result, their motion is easily controlled by manipulating the input waveform. These actuators contain a simple design and can operate over a wide range of frequencies, which make them suitable for closed-loop control (Cattafesta & Sheplak 2011). The effectiveness of these actuators are dependent on many parameters including oscillation frequency and amplitude, location of actuation, method of installation, and mode of excitation.

Piezoelectric actuators are resonant devices, which means they oscillate at increasingly high amplitudes when they operate close to its resonant frequency. This is beneficial for flow control since higher amplitude results in more energy transferred to the fluid, thus more effective for flow control (i.e. the flow remains attached for higher angles of attack). Therefore, many researchers chose to operate piezoelectric actuators close to the resonant frequency (Blackwelder *et al.* 1998; Kim *et al.* 2013; Seifert *et al.* 1998; Zhang *et al.* 2012). This may be detrimental in some cases because piezoelectric actuators are ceramic, which means they are extremely brittle. Subsequently, there is a higher chance of failure at large amplitudes. According to Seifert *et al.* (1996), the most effective actuation frequency, f , for flow control occurs at $St = 1$, where $St = f l_c / U_\infty$. The characteristic length, l_c , in this scenario is the streamwise size of the separated region. For example, the characteristic length of an airfoil with trailing-edge separation at $x = 0.8c$ with no reattachment is $0.2c$. In a separate study, Kim *et al.* (2013) studied the flow around a single actuator operating at various non-dimensionalized frequencies ($St = 0.1, 0.67, 1.33, \text{ and } 2.53$). Unlike previous researchers, Kim *et al.* (2013) defined the characteristic length as the gap between the edge of the actuators and the cavity's sidewall. Counter-rotating streamwise vortex pairs were observed at low to moderate excitation frequencies ($St = 0.1 - 0.67$), which increased in size with increasing actuating frequency. At higher frequencies ($St > 1.33$), the flow became highly unorganized, resulting in an increase of mixing downstream of the actuators. Careful selection of the actuation frequency is required ensure optimum separation suppression while avoiding breakage during actuation.

The effectiveness of piezoelectric actuators for flow control is also dependent on the how the actuators are mounted, specifically the placement, spacing, and cavity. According to Seifert *et al.* (1996), effective flow control is achieved when the amplitude of the oscillation is largest at the mean separation point. This is true for all types of periodic active flow control. Actuators are

typically installed in a row along the spanwise direction (Choi *et al.* 2002; Seifert *et al.* 1998) with a small gap between actuators to prevent them from rubbing up against each other while in motion. Seifert *et al.* (1998) and Choi *et al.* (2002) installed the actuators with 0.5 mm and 2 mm gaps in between actuators, respectively. According to Kim *et al.* (2013), the formation of streamwise vortex pairs is affected by the gap width since these structures are generated through the efflux and influx of fluid through the gap. The presence of gaps in between actuators can also introduce three-dimensional effects that may affect the performance of flow control. However, this effect is not known, as there are no study that directly compare the performance of piezoelectric electric actuators mounted with and without gaps. Finally, the method in which the actuators are installed onto the surface can also affect the actuators ability to generate streamwise and spanwise vortices. Piezoelectric actuators are commonly mounted flush with the surface with a cavity underneath (Choi *et al.* 2002; Seifert *et al.* 1998; Zhang *et al.* 2012), allowing the actuators to oscillate symmetrically in the wall-normal direction. Jeon & Blackwelder (2000) mounted their actuator directly on the surface without a cavity leading to an asymmetric oscillation. Both forms of mounting are able to suppress separation by generating streamwise and spanwise vortices. However, it is not known which method is more efficient as there are no literature that directly compare the performances of the two methods.

Two modes of actuation have been investigated in the past: a two-dimensional mode where all actuators along the airfoil span operate in phase with each other and a three-dimensional mode where adjacent actuators operate 180° out of phase relative to each other. Seifert *et al.* (1998) investigated the effects the two different actuation modes have on airfoil performance. In this study, the authors mounted the actuators upstream of an airfoil with trailing-edge separation at $x/c = 0.41$. It was discovered that both modes of actuation produced similar results in terms of increasing maximum lift and delaying the stall angle; both modes increased maximum lift by ~20% and the stall angle by 2 – 4°. This was later validated by Choi *et al.* (2002), who also observed minimal differences between performances of the two modes. The two-dimensional mode is preferred for dynamic stall control because it contains a mild post-stall behavior, i.e. lift decreases at a slower rate post separation with increasing angle of attack. On the other hand, the three-dimensional mode requires four times less power to run. This is because the downward motion of the actuator assists the upward motion of the adjacent actuators (Seifert *et al.* 1998). On the other hand, the two-dimensional mode requires more power as the downward movement of the actuator

temporarily compresses the fluid in the cavity between cycles. Under a two-dimensional mode, Zhang *et al.* (2012) supplied the actuators with a sine and square-wave signal and then compared the turbulence statistics of the controlled flow. It was discovered that the periodic motion resulted in an increase in mean velocity and Reynold stresses in both the streamwise and wall-normal direction. The increase of Reynold stresses indicate an increase in turbulence, which helps with delaying APG-induced separation. A square-wave signal was deemed more effective for flow control, since it contains both harmonic and perturbation frequency component, allowing the actuators to supply more energy to the fluid close to the wall. It can be seen from the literatures that only simple actuating modes and input signals have be investigated. In the future, more complicated arrangements of actuators and signals can be looked into.

By delaying separation with oscillating piezoelectric actuators, the airfoil exhibits an increase in maximum lift, stall angle, lift-drag ratio, and a reduction in drag. In general, the working principle behind piezoelectric actuators is linked to the formation of streamwise and spanwise vortices. These structures transport low-momentum fluid away from the wall while bringing in high-momentum fluid towards the wall (Kim *et al.* 2013). This motion corresponds to an increase of both mean velocity and Reynold stresses in the near-wall region, leading to a delayed separation (Zhang *et al.* 2012). According to Blackwelder *et al.* (1998), vibrating actuators form two low-speed regions with spanwise velocity. The presence of spanwise motion slows down the decay of streamwise vortices, allowing the mixing of low- and high-speed fluid to persist. Beyond this principle, there is little information on how else the oscillating flaps affect the topology of separated flow, specifically the skin-friction lines, as most studies were focused solely on the performance parameters, i.e. lift and drag. The present investigation aims to characterize the effects of piezoelectric flapping actuators on skin-friction lines under different actuation modes.

2.3 Particle Image Velocimetry

PIV is a modern method of flow visualization that can be used to obtain the velocity field over a plane or volume. The benefits of PIV include quantitative results, non-invasive to the surrounding flow, and the capability of time-resolved measurements. The measurement of two-dimensional vectors within the plane of interest is known as planar PIV (2D-2C), while the measurement of three-dimensional vectors within a two-dimensional plane is stereoscopic PIV (2D-3C). Advancement in PIV system allowed for measurement of three-dimensional velocity vectors within a given volume, which is known as tomographic PIV (3D-3C). The following section covers the main measurement technique used in the experiment: planar PIV. The content in this section were obtained from a PIV textbook (Raffel *et al.* 2018) and conference paper (Brossard *et al.* 2009).

2.3.1 Fundamental Principle

The principal of PIV is simple: particles inside a region of interest are illuminated with a light source and visualization of the flow is recorded in grayscale. The instantaneous velocity field is calculated by

$$\mathbf{U} = \frac{\Delta \mathbf{x}}{t} \quad 2.5$$

where $\Delta \mathbf{x}$ is the displacement vector for a group of particles over a time interval, t . The displacement vector is determined through a statistical method known as vector cross correlation while the time interval is the delay between adjacent frames. A schematic of a simple planar PIV experiment for a channel flow with one camera is shown in Figure 8. There are four main components in a PIV setup: camera(s), a light source, tracer particles, and a timing unit. In many cases, optics are used to form and position the laser sheet. Additional cameras can be used to achieve a larger field-of-view for planar PIV. Multiple cameras are necessary for stereoscopic and tomographic PIV to determine the position of the fluid in three-dimensional space. The camera can have either a charge-coupled device (CCD) sensor or a complementary metal-oxide semiconductor (CMOS) sensor. CMOS sensors analyze one pixel at a time, which makes it time-efficient for examining part of an image. The light source is used to light up the particles so the cameras can detect them. A laser is typically used due to its high concentration of power. Tracer

particles are added to the flow to improve flow visualization. A timing unit is used to coordinate and manage the timing between the cameras and laser. The steps of PIV are highlighted below

- 1) The region of interest is illuminated by a light source, which is typically a high-power laser that is formed into a sheet or volume.
- 2) The flow is seeded with appropriate sized particles.
- 3) Grayscale images of the region of interest are obtained with a known time interval between images.
- 4) Image is discretized into smaller interrogation windows and cross-correlation is used to determine the velocity field between frames/images.

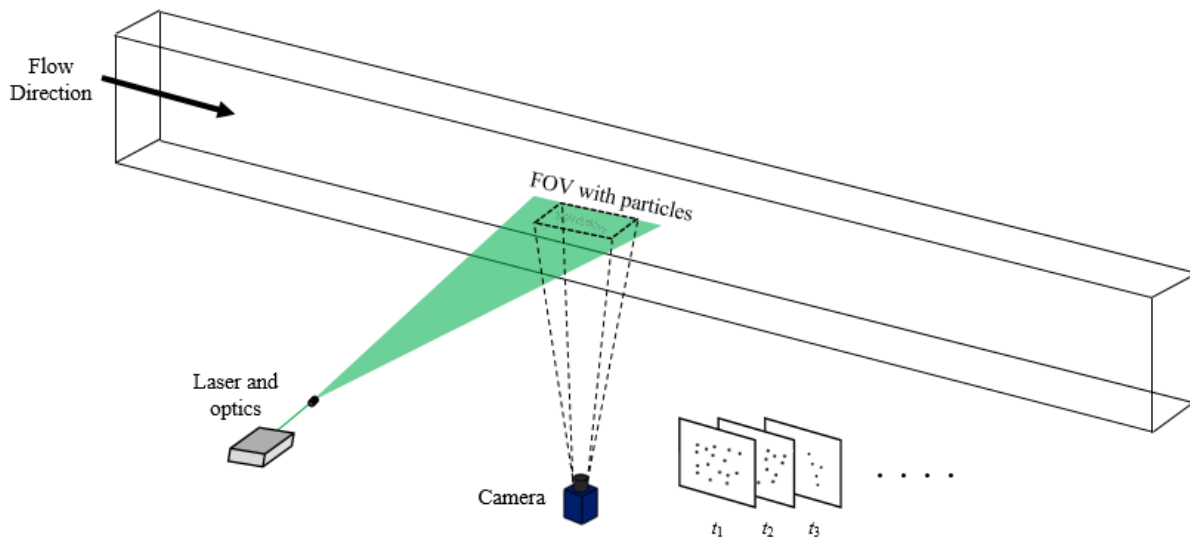


Figure 8. A basic schematic of a time-resolved planar PIV setup for investigating the flow inside a channel.

2.3.2 Tracer Particles and Seeding

It should be noted that PIV measures the motion of the fluid by determining the displacement of the tracer particles. Consequently, the particles should follow the motion of the fluid for the PIV measurements to be accurate. In other words, the response time of the particle should be minimized. If the density of the particle is higher than the density of the fluid, which is usually the case for the study of airflow, then the response time of the particle due to motion of the fluid is given by

$$\tau_p = d_p^2 \frac{\rho_p}{18\mu}. \quad 2.6$$

where ρ_p is the particle density, d_p is the diameter of the particle, and μ is the dynamic viscosity of the fluid (Raffel *et al.* 2018). From equation 2.6, it is shown that larger, denser particles will result in a longer response time. The size of the particles should also be proportional to the magnification of the cameras; each particle should occupy 2 – 4 pixels to avoid peak-locking error (Adrian & Westerweel 2011). Peak-locking is an error source of PIV where both the location and position of a particle is biased towards the closest integer (Michaelis *et al.* 2016). Smoke particles from a fog generator is typically used for PIV experiments inside a wind tunnel. If laser power is an issue, then helium-filled soap bubbles is an option. The particle is deemed acceptable for PIV if the particle Stokes number

$$Stk = \frac{\tau_p}{\tau_f} \quad 2.7$$

is less than 0.1 (Raffel *et al.* 2018). The characteristic time scale of the flow, τ_f is defined as the ratio between the length scale and characteristic velocity of the flow studied. Ideally, the size of the particle should be as small as possible, but large enough to be observed in the images.

Uniform seeding density with at least 6 – 8 particles per interrogation window is suitable for PIV (Kähler *et al.* 2012). Lower particle density is suitable for particle tracking velocimetry (PTV). The time delay between frames should be selected so that the particles move approximately a quarter of the window size.

2.3.3 Image Quality

It is imperative that there is sufficient contrast between the particle and the background in order to isolate the position of the particle. Contrast between the particle and background is directly proportional to the amount of light scattered by the particle. The amount of light scattered from a particle is quantified by the scattering cross section, which is the ratio of total scattered power to laser directed on the particle (Melling 1997). The scattering cross section is dependent on the ratio of particle diameter to light's wavelength, d_p/λ . Mie's scattering theory is applied for particles with diameter larger than the wavelength of the scattered light (Raffel *et al.* 2018), which is indicated by the region where $d_p/\lambda > 1$ in Figure 9.

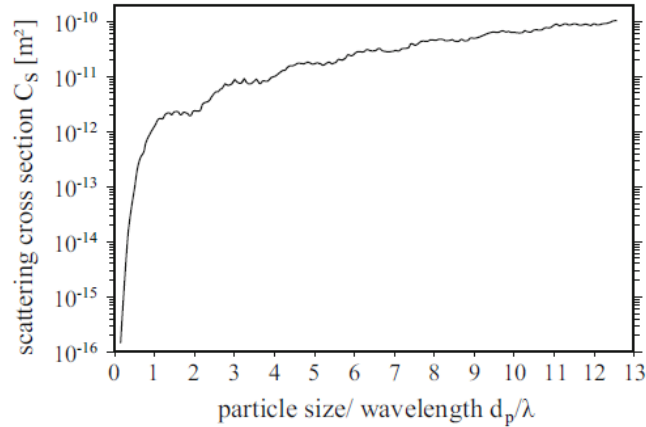


Figure 9. The scattering cross section as a function of particle diameter and wavelength of incident light. Figure taken from Melling (1997).

If the laser power is dispersed over a large region, such as the case for tomographic PIV, then the amount of light scattered off the particles can be an issue. From Figure 9, it is shown that the intensity of light scattered can be increased by increasing the size of the particle. When picking out a tracer particle, the size of the sphere should be small to minimize response time, yet large enough to create a sufficient contrast with the background. The light scattering pattern from a 1 μm oil droplet in air is shown in Figure 10. The amount of light scattered from a particle is also dependent on the direction; more light is scattered in the direction of the incident light. This phenomenon is known as forward scatter (Raffel *et al.* 2018).

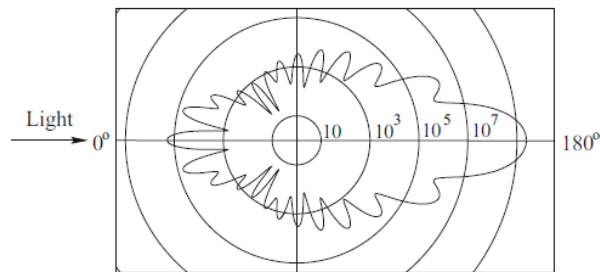


Figure 10. The light scattering pattern from a 1 μm oil droplet. Figure taken from Raffel *et al.* (2018).

2.3.4 Image Correlation

Instantaneous velocity vectors are determined through a statistical mean known as image cross correlation. The steps of vector cross correlation are highlighted in Figure 11 below. The simplest form of vector cross correlation involves two single-exposure frames with the time delay known. However, more advanced correlation schemes utilize more frames to minimize the likelihood of

erroneous vectors. To begin, images are broken down into many $M \times N$ pieces known as interrogation windows. The particles within an interrogation window are assumed to all move in unison. The cross correlation function for a shift of (x, y) pixels is described by

$$R_{II}(x, y) = \sum_{i=0}^M \sum_{j=0}^N I(i, j)I'(i + x, j + y) \quad 2.8$$

where I is a $M \times N$ matrix containing the intensity value of the pixels within an interrogation window in the first frame, and I' is an interrogation window in the second frame. The size of I' can be larger than $M \times N$ so that I does not extend outside of I' when it is shifted. The value is a measure of how well the two intensity fields I and I' align with each other (Raffel *et al.* 2018). A correlation map is obtained by calculating the correlation coefficient for a range of shifts. The shift that contains to the highest correlation coefficient is estimated to be the displacement of the group of particles within the interrogation window; this step is known as peak detection.

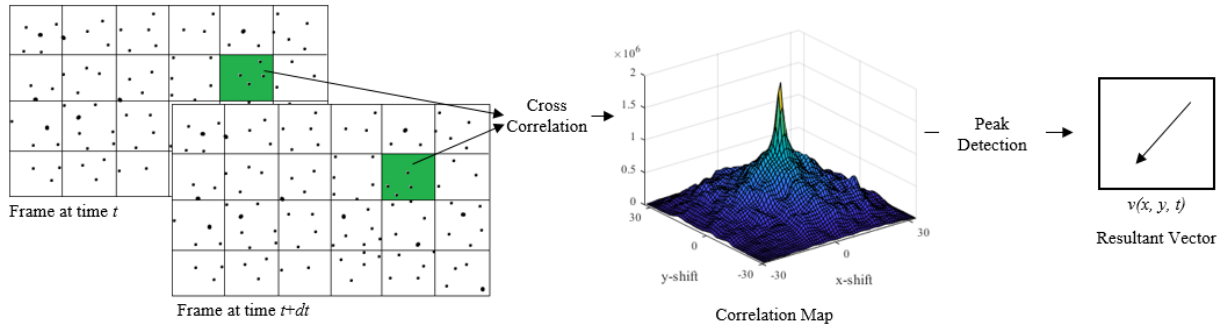


Figure 11. The three main steps of vector cross correlation for two single-exposure frames.

The confidence of the resultant vector can be improved by ensuring sufficient particle density and adequate contrast between the particles and background during data collection. Peak detection can also be improved by image processing to eliminate background noise. High spatial resolution is obtained by using a smaller window size. However, large windows are more suitable for peak detection. Multiple passes with decreasing window size after each pass is used to increase the likeliness of peak detection while also providing a high spatial resolution. There are many methods to improve peak detection and covering them all would be unreasonable. The methods discussed here are the main techniques used in this project.

2.4 Data Analysis Techniques

The following section covers some of the mathematical analysis deployed to analyze the PIV measurements. Proper orthogonal decomposition (POD) is covered in section 2.4.1 and Welch's fast Fourier transform is discussed in section 2.4.2.

2.4.1 Proper Orthogonal Decomposition

The purpose of POD is to decompose a set of high-order experimental or simulation data into an optimal low-dimensional basis (Luchtenburg *et al.* 2009), which is useful for identifying important characteristics and coherent structures for a particular type of flow. The decomposition breaks down the fluctuating velocity field $\mathbf{u}(\mathbf{x}, t)$ into N number of spatial modes $\mathbf{u}_i(\mathbf{x})$ and a corresponding temporal coefficient $a_i(t)$ as described by

$$\mathbf{u}(\mathbf{x}, t) = \sum_{i=1}^N a_i(t) \mathbf{u}_i(\mathbf{x}) \quad 2.9$$

The basis of spatial modes is optimal, which means that the mean square truncation error is minimized (Luchtenburg *et al.* 2009). These modes are ordered by their kinetic energy and a reduced order model of the complex flow can be built by neglecting the spatial modes that are deemed unimportant for characterization of the flow. The reduced order model essentially filters out low-energy noise within the ensemble. This method was used by Duquesne *et al.* (2015) to filter out small-scale flow structures so that structures in the instantaneous velocity field with higher-order of kinetic energy can be identified.

The method of snapshot (Sirovich 1987) is a discretization of POD and returns N number of spatial modes where N is equivalent to the number of snapshots within the ensemble. The method of snapshots starts by first forming a correlation matrix

$$\mathbf{C}_{mn} = \frac{1}{N} (u(\mathbf{x}, t_m), u(\mathbf{x}, t_n)) \quad 2.10$$

where (\mathbf{a}, \mathbf{b}) is the inner product of vector \mathbf{a} and \mathbf{b} . The eigenvector \mathbf{v}_i and eigenvalue λ_i of the correlation matrix is defined as

$$\mathbf{C}_{mn} \mathbf{v}_i = \lambda_i \mathbf{v}_i. \quad 2.11$$

The number of eigenvalues and eigenvectors for a set of PIV data is equivalent to the number of snapshots N . The energy content of the i^{th} mode is given by the eigenvalue λ_i , but is typically expressed as a proportion of the total energy

$$E_i = \lambda_i / \sum \lambda_i. \quad 2.12$$

After the eigenvectors are evaluated, the normalized spatial mode \mathbf{u}_i can then be computed by

$$\mathbf{u}_i = \frac{\boldsymbol{\phi}_i}{\|\boldsymbol{\phi}_i\|_2}, \text{ where} \quad 2.13$$

$$\boldsymbol{\phi}_i = \sum_{n=1}^N v_i(t_n) \mathbf{u}(t_n). \quad 2.14$$

The temporal amplitude is given by the inner product of the spatial mode and the original velocity field (i.e. the projection of the original velocity field onto the spatial mode)

$$a_i(t) = (\mathbf{u}(t), \mathbf{u}_i). \quad 2.15$$

2.4.2 Welch's Overlapped Segmented Average

Welch's Overlapped Segmented Average (WOSA) is used to estimate the power spectral density (PSD) of a time-series. Simply stated, the method involves breaking the time signal into segments, applying a discrete Fourier transform (DFT) on each segment, and then averaging the results. The DFT results of each segment is referred to as a periodogram. The main advantage of using WOSA is the reduction of variance in the estimated spectrum (Heinzel *et al.* 2002). In this thesis, we are concerned with a sampled signal f_n , where f_n contains N equally-spaced sampled points of the continuous $f(t)$. The time difference between adjacent signal points corresponds to the sampling interval, and the reciprocal of that is the sampling frequency f_s . Before going further, the PSD of a time-series shows the distribution of power over different frequencies (Seiler & Seiler 1989). Power is not defined here in its conventional sense (i.e. the rate of work), but rather as the square of its signal. For example, the mean power of the sampled signal f_n is defined as

$$P_m = \frac{1}{N} \sum_{n=1}^N |f_n|^2. \quad 2.16$$

The steps to generating a PSD estimate using Welch's method are highlighted by Heinzel *et al.* (2002) and summarized below:

1. The length of segment, M , is selected based on the desired frequency resolution. The value M is restricted to even numbers only. In some cases, it is recommended that the length of

each segment be a power of 2 to speed up processing time. The resolution of the frequency spectrum is a function of the length of each segment, which is given by

$$f_{res} = \frac{f_s}{M} \quad 2.17$$

By rearranging equation 2.17 to solve for M , the estimated value of M can be determined and then rounded up to the nearest allowable value.

2. The DFT function assumes that a time series of finite length is periodic for an infinite amount of time. In other words, the sampled signal repeats itself indefinitely. If the frequency of the input signal is not an exact multiple of the resolution frequency, which is typically the case, then the frequency spectrum will contain side lobes due to the discontinuity between the last point of the signal and the first point of the repeated signal (Heinzel *et al.* 2002). A window function is multiplied on top of the signal before performing DFT to reduce the significance of the discontinuity, thus suppressing the side lobes. The key feature of a window function is that it starts at or near zero, increase to a maximum at the center, and then back to zero at the end. Some common window functions are Hanning, Hamming, Kaiser4 and Blackman, which are shown in Figure 12.

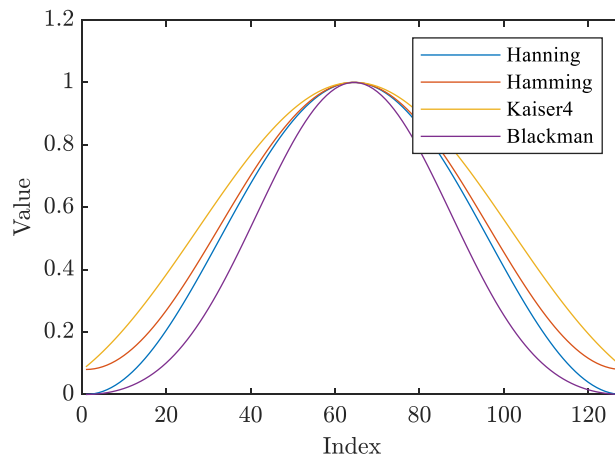
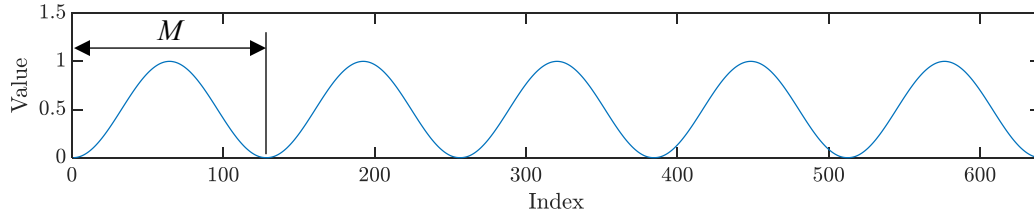


Figure 12. The Hanning, Hamming, Kaiser4, and Blackman window function with a length of 128 elements.

3. Once the window function is chosen, a suitable amount of overlap between segments of data must be chosen. The disadvantage of having non-overlapping segment is that points near the edge of the windows will have lesser weighting. This effect is visualized in Figure 13. The amount of overlap is typically dependent on the selected window function. An

overlap of 50% is suitable for a wide window such as Hanning, while 84% may be required for narrower flat-top windows (Heinzel *et al.* 2002).

(a)



(b)

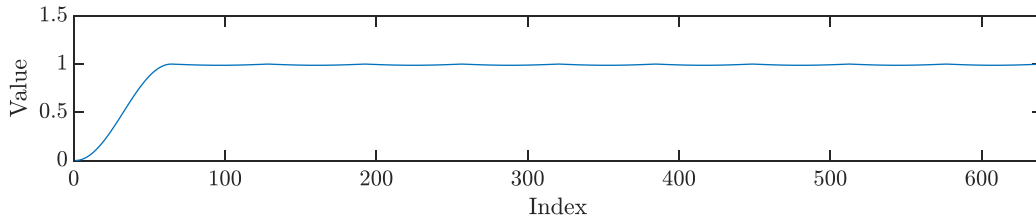


Figure 13. The distribution of weighting for a Hanning window with $M = 128$ over 640 data points with (a) no overlap, (b) and 50% overlap.

4. After multiplying the window function onto an individual segment of data, the values are fed into a DFT. The normalization of the DFT function may vary depending on the software used. In the present study, it is defined as

$$y_m = \frac{1}{M} \sum_{k=0}^{M-1} x_k e^{-2\pi i \frac{mk}{M}} \quad 2.18$$

where x_k is the input segment signal with the window function applied. Once the Fourier transform has been applied, the squared magnitude of the output y_m is evaluated and then averaged between all segments. The PSD can then be calculated by

$$\text{PSD} = \frac{2|y_m|^2}{f_s S_2} \quad 2.19$$

where S_2 is the sum of squares of the window function.

Chapter 3. Experimental Setup

This following section contains descriptions of all aspects of the experimental setup including the wind tunnel facility, airfoil model, and PIV setups for both experiment I and II. Experiment I is multiple PIV experiments used to characterize the intermittency of a three-dimensional separation over an airfoil. Experiment II features a parametric investigation on the impact of oscillating piezoelectric actuators on flow topology and turbulence statistics. The same airfoil model and wind tunnel facility were used for both experiments.

3.1 Wind Tunnel

The experiments were performed inside a closed-loop wind tunnel at the University of Alberta, which has a contraction ratio of 6.3:1 resulting in a cross sectional area of $2.4 \times 1.2 \text{ m}^2$ ($W \times H$) in the main test section. A model of the wind tunnel is presented in Figure 14. The wind tunnel is able to output a maximum wind speed of 35 m s^{-1} . Multiple meshes were installed to reduce turbulence intensity. Hotwire measurements from Gibeau & Ghaemi (2020) revealed a turbulence intensity of less than 0.4% in the test section at the freestream speed considered. Transparent acrylic and glass walls allowed for conducting PIV experiments. Pitot tubes were installed in the test section, one in the upstream and another in the downstream section, to measure the wind speed.

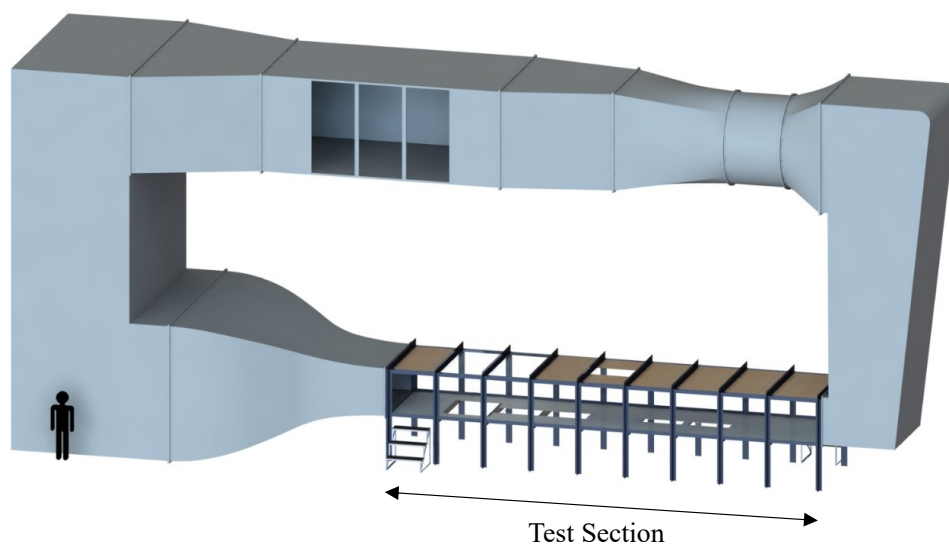


Figure 14. A model of the closed-loop wind tunnel in the Mechanical Engineering building at University of Alberta.

3.2 Airfoil Model

An APG-induced separation was formed near the trailing edge of a NACA 4418 airfoil at a moderate angle of attack. This particular profile was selected because it features a gradual decrease of post-stall lift, which is typical for airfoils that experience trailing-edge stall (Abbott & Von Doenhoff 1959). The lift curve for a NACA 4418 airfoil is shown in Figure 16. The curve reveal a gradual decrease of lift with increasing pitch angle after the maximum lift has been achieved. This is a characteristic of a trailing-edge separation. The NACA 4418 airfoil was constructed by folding an aluminum sheet around four equally spaced ribs. The ribs were machined using a water jet cutter to ensure a consistent profile. The airfoil has a chord length $c = 975$ mm and a span $s = 1200$ mm, corresponding to an aspect ratio of 1.2. A thick turbulent boundary layer with large-scale separation was desired so that the turbulent motions could be spatially resolved with PIV, hence a large chord length was chosen. A 1-mm trip wire was placed on the upper surface at $0.2c$ to ensure uniform transition to turbulence along the span of the airfoil. In order to measure the near-surface flow with planar PIV, the NACA 4418 airfoil was customized to have a flat rear section of length $l = 350$ mm that spanned from $0.67c$ to the trailing edge. A comparison of the customized profile and the original NACA 4418 airfoil can be seen in Figure 15. The customized profile was generated by removing the last 23% chord of the original NACA 4418 profile, and then using two tangent lines to extend the profile on the suction and pressure side until the lines meet. Since the curvature of the NACA 4418 profile in the rear portion is minimal, the difference between the original NACA 4418 profile and the customized profile is small. The airfoil was mounted vertically inside the wind tunnel with the gap between the airfoil and the sidewalls sealed.

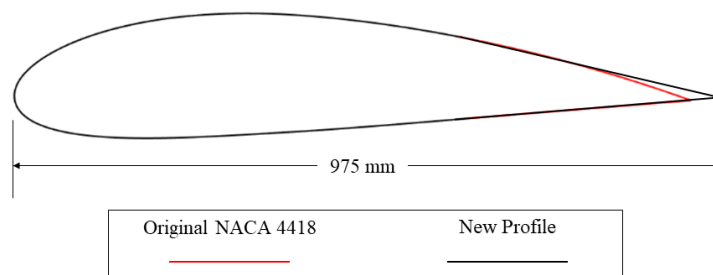


Figure 15. A comparison of the original NACA 4418 airfoil and the new profile that contains a flat section in the rear 23% of the chord.

A simple way of evaluating the direction and unsteadiness of the flow on an airfoil is attaching a series of organized yarns (tufts) throughout the surface. It is a quick and simple method to

determine whether separated flow over an airfoil has occurred. Tuft measurement were conducted on the suction side of the airfoil to determine whether a leading-edge separation bubble was present. The tufts covered the center 50% span and were spaced 50 mm apart in both the streamwise and spanwise direction. The strand of yarn was taped vertically so that there is no bias in either streamwise direction with the wind tunnel off (Figure 17a). A photo of the tuft visualization is shown in Figure 17b with the identical angle of attack and Reynolds number as ‘Experiment I’. It was determined that there is no leading-edge separation bubble since the tufts at the leading edge pointed downstream during the entire duration of the experiment, showing no signs of intermittency, i.e. separation.

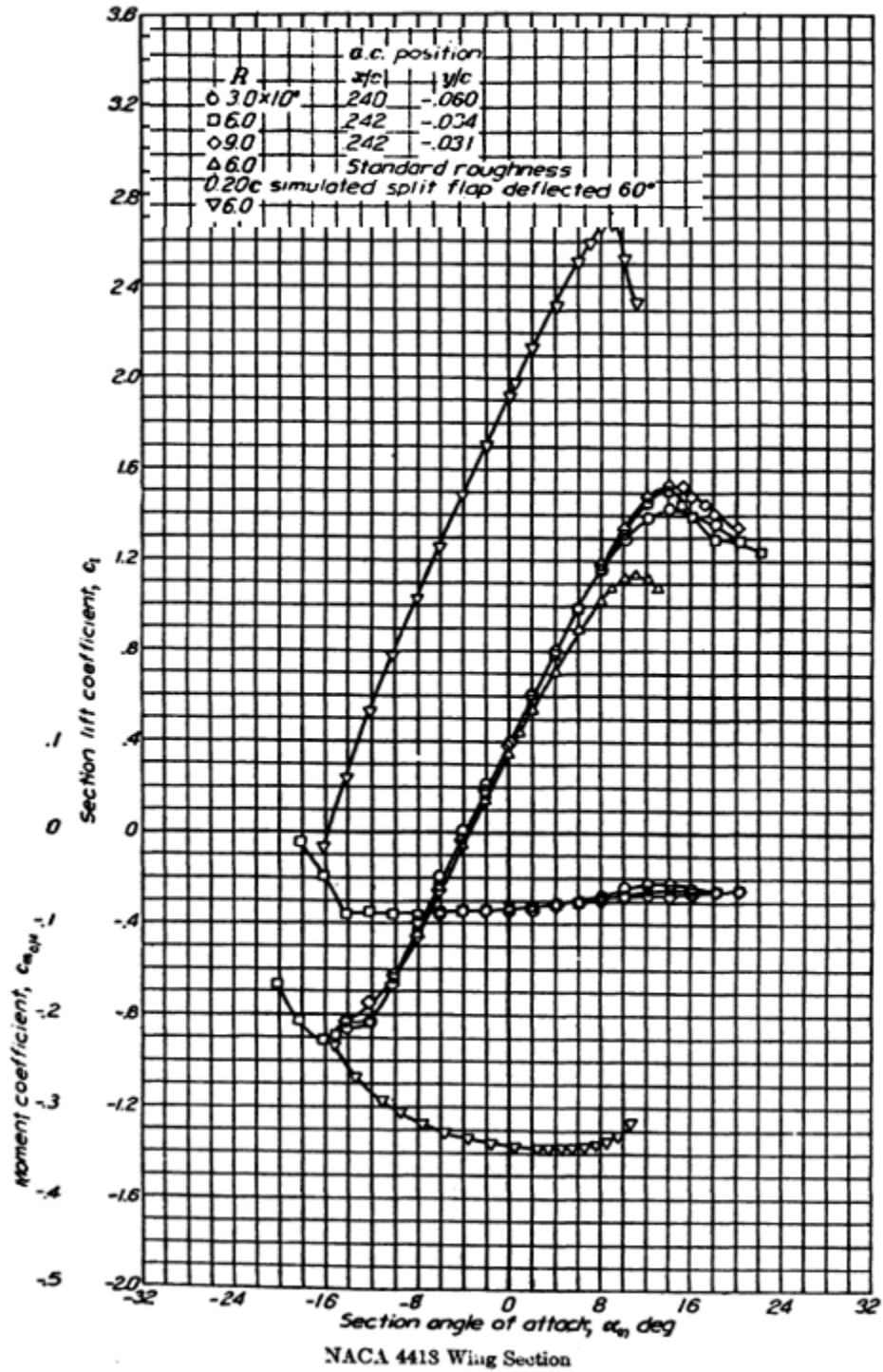
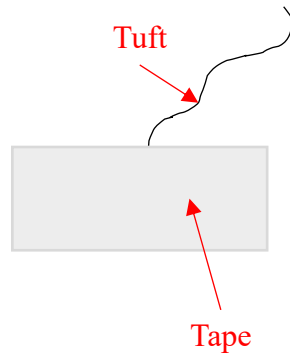


Figure 16. The lift-coefficient curve of the NACA 4418 airfoil at different Reynolds number (Abbott & Von Doenhoff 1959). Taken with permission.

(a)



(b)

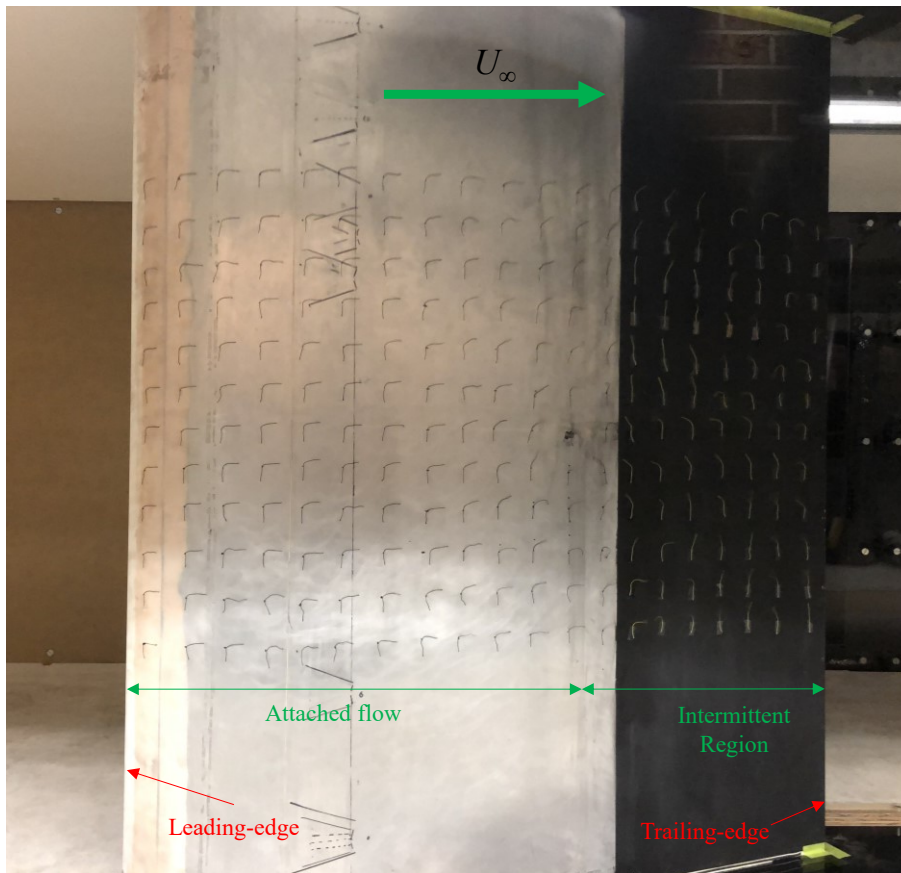


Figure 17 (a) Schematic of the tuft installation and (b) flow visualization of the trailing-edge separation with tufts.

3.3 Experiment I

Measurement of the separated flow was conducted using two separate planar PIV configurations. The first PIV setup features an x - y plane located along the mid-span of the airfoil, which is used to characterize the profile leading up to and post separation. A second setup was used to measure the near-wall streamlines. This was achieved by performing PIV on an x - z plane located as close to the flat section of the airfoil as possible. The two configurations are shown in Figure 18, and additional details of the PIV setups are provided in sections 3.3.1 and 3.3.2. A freestream speed of $U_\infty = 12 \text{ m s}^{-1}$ was used for this experiment, resulting in a Reynolds number as defined by the airfoil chord length ($Re_c = \rho U_\infty c / \mu$) of 750000. An angle of attack of 9° was chosen iteratively so that the mean separation point at mid-span was located near the center of flat trailing-edge section at $0.86c$. The origin (point O) is defined so that $x = 0$ is aligned with the mean separation point of the mid-span plane, $y = 0$ is the surface of the airfoil, and $z = 0$ is mid-span.

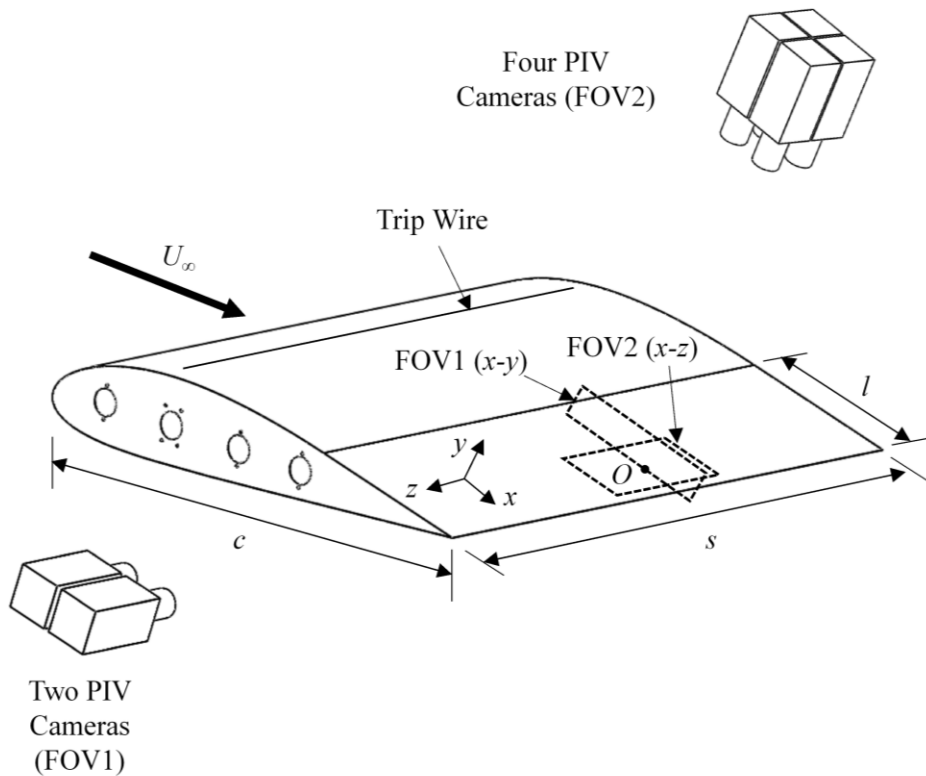


Figure 18. Schematic of the PIV setups for experiment I. The coordinates are defined relative to the flat surface of the airfoil. The origin of the coordinate system (O) is located at the separation point at mid-span and 140 mm ($0.14c$) upstream of the trailing edge. Note that the axes are displaced from mid-span of the airfoil for clarity of the figure.

3.3.1 Particle Image Velocimetry in the x - y Plane

The characteristics of the boundary layer at mid-span were investigated using planar PIV at the field-of-view (FOV) labelled as FOV1 in Figure 18. A fog generator was used to generate 1- μm droplets as flow tracers. The tracers in the FOV were illuminated using a dual-head Nd:YLF laser (Photonics Industries, DM20-527-DH), which is capable of outputting 527 nm light at maximum energy of 20 mJ per pulse with a pulse width of 170 ns. The laser was shaped into a 1-mm-thick sheet using a combination of cylindrical and spherical lenses. Two coated mirrors were used to direct the laser sheet parallel to FOV1 along mid-span. The illuminated tracers within the FOV were recorded using two high-speed cameras (Phantom v611) with a maximum resolution of 1280×800 pixels. The cameras contain a complementary metal oxide semiconductor (CMOS) sensor with a $20 \times 20 \mu\text{m}^2$ pixel size. Grayscale images of the flow were recorded at 12-bit depth. Both cameras were fitted with identical 105-mm Sigma lenses with aperture settings of $f/2$, and were placed 750 mm away from the viewing plane. At this distance, the FOVs of the cameras were $180 \times 53 \text{ mm}^2$ and $181 \times 53 \text{ mm}^2$, including a 15 mm overlap in the streamwise direction. The imaging system was calibrated to obtain the scaling and the relative orientation of the two FOVs by imaging a calibration grid.

Double-frame images were collected at 24 Hz with a delay of 150 μs between adjacent frames. Five sets of images were collected and each set of data contained 2700 images acquired over 112 s. Image and vector processing was performed using DaVis 8.4 (LaVision GmbH). In order to remove the background noise, the ensemble minimum was subtracted from all of the images. Normalization of the particle intensities was achieved by dividing the intensity values by the ensemble average. All images were cross-correlated multiple times with a final interrogation window size of 32×32 pixels with 75% overlap. The images were processed a second time using a sum-of-correlation algorithm (Meinhart *et al.* 2000) with a final window size of 8×8 pixels and 75% overlap. The sum-of-correlation processing scheme allowed for smaller interrogation windows, resulting in a higher spatial resolution for the mean velocity field. This was desired for characterization of the boundary layer profile. Vectors with a normalized residual value of greater than 2 within a 3×3 vector window were considered to be outliers and removed (Westerweel & Scarano 2005). The number of incorrect vectors accounted for less than 0.5% of the total vectors and were replaced by interpolation. The vectors from each camera FOV were stitched in DaVis 8.4 based on the spatial coordinates obtained through calibration. After stitching the vector fields

and removing the unwanted borders, the size of the effective FOV was $(\Delta x, \Delta y) = 325 \times 53 \text{ mm}^2$ with a digital resolution of 7.1 pix mm^{-1} . The minimum resolvable velocity for planar PIV is a displacement of approximately 0.1 pixels (Raffel *et al.* 2018). Under the current configuration, the error of the velocity measurement taken from 0.09 m s^{-1} ($0.008U_\infty$).

The measurements collected from this FOV are used to determine Reynold stresses and turbulence transport terms. Statistical convergence of these second- and third-order central moments was verified by plotting them against the number of samples at 50 locations distributed throughout the FOV. An example of a convergence curve for the Reynolds stresses and turbulence transport terms at one location is shown in Figure 19. The difference between the maximum and minimum value for the last 20% of each convergence curve was calculated. The random error of each parameter was estimated as the maximum difference from the 50 locations. The random errors of $\langle u^2 \rangle / U_\infty^2$, $\langle v^2 \rangle / U_\infty^2$, and $\langle uv \rangle / U_\infty^2$ are estimated to be 2.8, 0.6, and 1.1×10^{-4} , respectively. The random errors of $\langle u^3 \rangle / U_\infty^3$ and $\langle u^2 v \rangle / U_\infty^3$ are 11 and 2.5×10^{-5} , respectively.

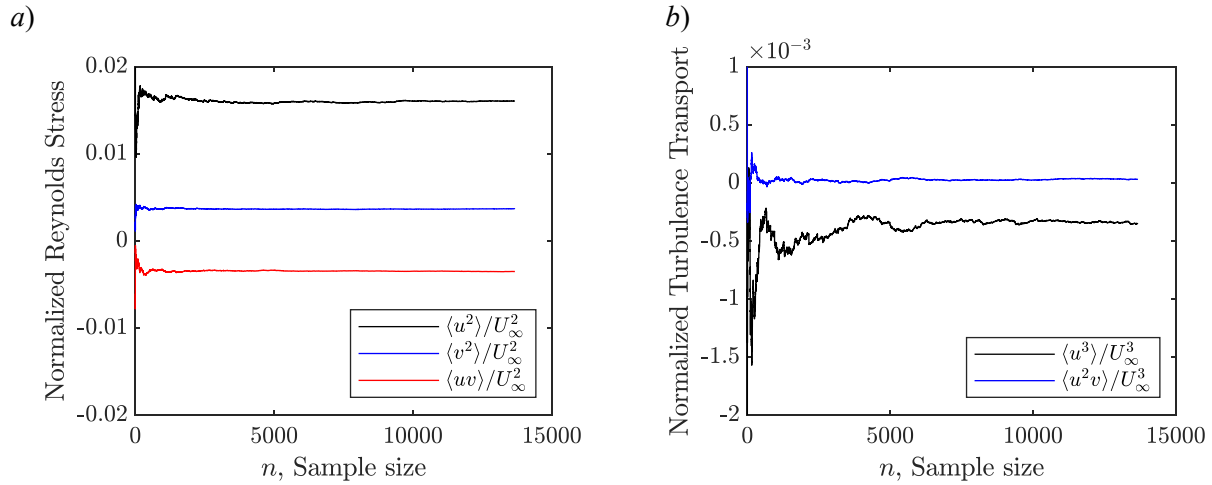


Figure 19. Statistical convergence of the (a) second-order and (b) third-order moments. The results shown here are for a sample point located at $(x, y) = (10, 25) \text{ mm}$.

3.3.2 Particle Image Velocimetry in the x - z Plane

The near-surface flow in a plane parallel to the flat section of the airfoil was measured using planar PIV in the FOV denoted as FOV2 in Figure 18. The same laser and Phantom v611 cameras used in the first configuration were also used in this setup. A combination of spherical and cylindrical lenses was used to collimate the laser beam into a 1-mm-thick laser sheet, which was directed parallel with the surface of the model using a large mirror. The center of the laser sheet was 2 mm

away from the flat surface of the airfoil. Four cameras were used to increase the size of the viewing region while maintaining a large spatial resolution. Each camera was fitted with a 200-mm Nikon lens with an aperture setting of $f/4$ and extension rings. The front of the lens was positioned 1550 mm from the region of interest. Due to the physical size of the cameras, they were angled slightly in order to obtain a 15 mm overlap in the streamwise direction and 25 mm overlap in the spanwise direction. Because the angle was less than 1° , the parallax error introduced by tilting the cameras is less than 0.1%. After stitching the images and removing the unwanted edges, the effective FOV was $(\Delta x, \Delta z) = 170 \times 230 \text{ mm}^2$ with a digital resolution of 7.9 pix mm^{-1} . Once again, the minimum resolvable velocity for planar PIV is a displacement of approximately 0.1 pixels (Raffel *et al.* 2018). However, a sliding sum-of-correlation algorithm was used with five successive images. This reduces the minimum resolvable velocity vector by a factor of five (Ghaemi *et al.* 2012). With this taken into consideration, the error of the velocity measurement taken from 0.004 m s^{-1} ($0.0004U_\infty$).

The sampling duration of each data set was limited by the storage capacity of the high-speed cameras. Consequently, two different camera settings were utilized for recording images within FOV2: one to obtain a large quantity of uncorrelated vector fields and another to gather time-resolved data. The uncorrelated data were collected in a cyclic multi-frame mode, where each cycle consisted of five successive images at 1750 Hz. The cycles were acquired every second for a total duration of 60 seconds. The measurement was repeated 20 times to obtain 1200 uncorrelated cycles. By acquiring five images at a high temporal rate of 1750 Hz within each cycle, a sliding-average correlation could be used for the evaluation of the velocity vectors to increase the signal-to-noise ratio (Ghaemi *et al.* 2012). The time-resolved data consisted of five individual sets of 5000 single-frame images collected at 1750 Hz. The uncorrelated images obtained from the first acquisition method will be referred to as the cyclic data while the latter will be referred to as the time-resolved data. The cyclic data were suitable for obtaining statistically converged quantities for some of the analyses including the evaluation of mean velocity field, Reynold stresses, and POD. In contrast, the time-resolved data was used to gain insight into the evolution of coherent structures present in the separation region.

All image and vector processing was performed using DaVis 8.4 once again. Background noise was removed by subtracting the ensemble minimum and then normalization was achieved by dividing the intensity values by the ensemble average. All images were cross-correlated using

a sliding sum-of-correlation of five successive frames (Ghaemi *et al.* 2012). The use of sliding sum-of-correlation reduced the number of incorrect and empty vectors. Multiple passes were used with a final interrogation window size of 48×48 pixels and 75% overlap. An outlier detection method, based on Westerweel & Scarano (2005), was applied to remove spurious vectors, which made up for less than 1% of the total vectors and were replaced by interpolation.

3.3.3 Detection and Tracking of Critical Points

The points on a surface where the wall shear, τ , is zero in all direction (i.e. $\tau_x = \tau_z = 0$) are known as the singular or critical points (D elery 2013). These critical points can be detected by identifying points with zero wall-normal gradient, i.e. $dU/dy = 0$, which along with the no-slip condition implies zero velocity in the immediate vicinity of the wall. However, since the measurements in the x - z plane were carried out at a wall-normal distance of $y = 2$ mm, a maximum threshold of 0.12 m s^{-1} ($0.01U_\infty$) was used for detecting the critical points. This threshold accommodates slight deviations from a linear dU/dy profile. The threshold value was determined iteratively through visual inspection of the critical points relative to the streamlines. A threshold smaller than $0.01U_\infty$ did not detect all the critical points that could be identified by visualized inspection of the streamlines, and a threshold value greater than $0.01U_\infty$ resulted in the detection of several spurious critical points. Velocity magnitude is defined here as the magnitude of the two-dimensional velocity vector in the streamwise-spanwise plane only. The wall-normal velocity does not contribute to the shear stress at the wall. In the algorithm, duplication of critical points in a neighborhood pertaining to the same structure were removed by only considering the local minima within a neighborhood of 9×9 vectors ($12 \text{ mm} \times 12 \text{ mm}$). After detection of the critical points, their classification is achieved by solving the equation introduced by Henri Poincar e (D elery 2013);

$$S^2 + pS + q = 0, \text{ where} \quad 3.1$$

$$p = -\frac{\partial U}{\partial x} - \frac{\partial W}{\partial z}, \text{ and} \quad 3.2$$

$$q = \frac{\partial U}{\partial x} \frac{\partial W}{\partial z} - \frac{\partial W}{\partial x} \frac{\partial U}{\partial z}. \quad 3.3$$

The roots of equation 3.1, S , reveal the type of critical point present. Nodes exist when both roots are real and of the same sign, foci exist when the roots form a pair of complex conjugates, and saddle points are present when the roots are real with opposite signs. The partial derivatives of the

velocity components on the right side of equations 3.2 and 3.3 were computed by fitting the vectors with a least-squares-optimal quadratic using a kernel size of 5.

A simple tracking algorithm was developed to follow saddle points and foci in the time-resolved velocity fields. The Matlab code for the tracking algorithm can be found in Appendix B. The tracking was achieved by applying a $6 \times 6 \text{ mm}^2$ (5×5 vectors) tracking window to an identified saddle point/focus and searching for another saddle point/focus inside the window in the next two frames. If subsequent structures are found, then they are grouped and a track is generated. This procedure is repeated until no more structures can be detected inside the tracking window, in which case the track ends. This tracking window can follow structures that are advected by velocities up to $0.44U_\infty$ in the near-wall x - z plane. Tracks with a lifespan of less than 25 frames (0.014 s) were also removed to consider only the coherent motions with a longer lifetime and to eliminate noise. Finally, the tracks were smoothed using a kernel regression that implements a quadratic polynomial and a kernel size of 5. The statistical convergence of the advection velocities were evaluated by plotting the value against the number of sample points. The convergence curves for the advection velocities and speeds of saddle points are shown in Figure 20. The difference between the maximum and minimum value for the last 20% segment of the statistical convergence curve was taken as the random error.

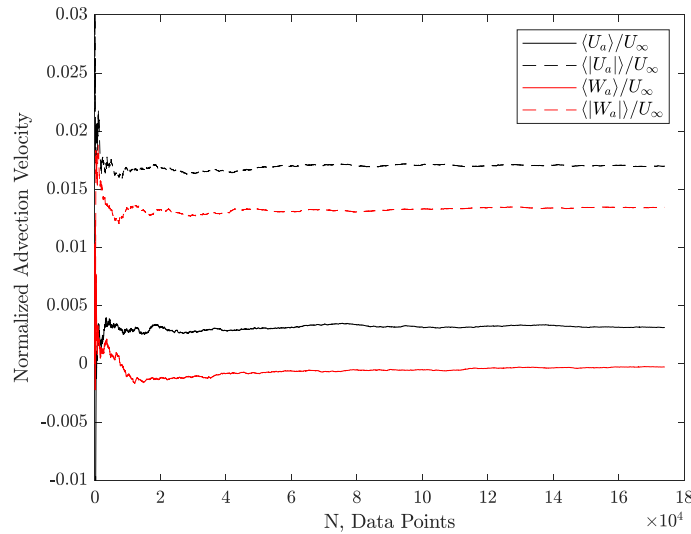


Figure 20. Convergence test of the advection velocities and speed for saddle points.

3.4 Experiment II

The purpose of experiment II is to investigate the effect of vibrating actuators on flow separation for different actuating frequencies, displacements, and modes of actuation. An array of actuator was installed onto the rear section of the NACA 4418 airfoil described in section 3.4.1. Experiment II was conducted at an angle of attack of 9° and a freestream speed of 10.5 ms^{-1} . The angle of attack and freestream speed were chosen so that the mean separation line occurred downstream of the actuators when they are at rest.

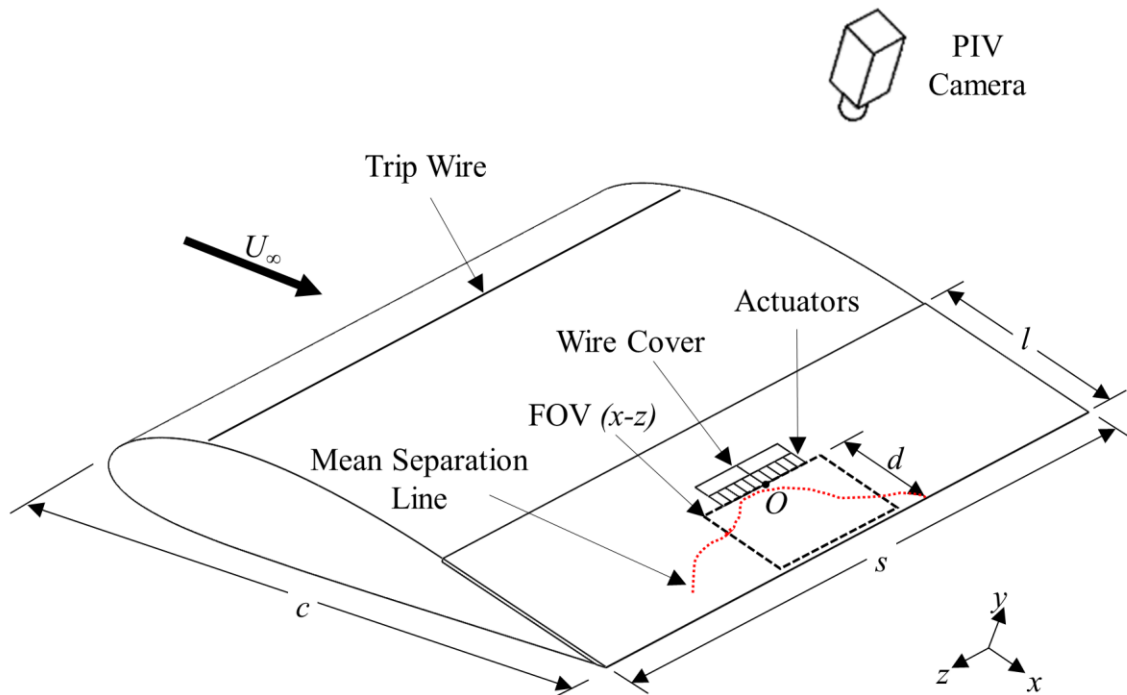


Figure 21. A schematic of the PIV setup for experiment II highlighting the location of the actuators and PIV cameras. The dimensions of the airfoil including the chord length (c), span (s), and length of the flat section (l) are the same as experiment I. The actuators are located 168 mm ($0.17c$) from the trailing edge of the airfoil (d).

3.4.1 Actuator Setup and Modes

Bender actuators from Physik Instrumente (PL 128.10) were used for the flow control. Ten piezoelectric actuators were mounted a distance $d = 168 \text{ mm}$ from the trailing edge of the airfoil as shown in Figure 21, which is immediately upstream of the mean separation line determined

from experiment I. A 0.005” thick steel flap with dimensions 19.5 mm × 29.5 mm ($w \times h$) was attached to each actuator to increase the surface area, resulting in a 0.5 mm gap between adjacent actuators. The free length of the actuator (L_f), defined as the portion of the actuator that is displaced in response to an electrical signal, is 28 mm. A cavity was machined onto the rear flat plate so that the piezoelectric actuators with the steel flap remained flush to the surface, as shown by the side view in Figure 22(b). This is to ensure that the actuators have minimal effect on the surrounding flow when they are not running. A rectangular hole is also machined into the flat plate so the actuator wires can pass through the airfoil’s interior. Clay was used to seal the space leading to the airfoil interior to prevent flow leakage. Actuators were attached to the airfoil with thin double-sided tape.

The ten actuators in are split into two groups of five as shown by the label A and B in Figure 22(a). Each group of actuator can be controlled independently with an input signal generated from a Speedgoat real-time target machine (SD631) installed with the IO135 module. An amplifier is present between the Speedgoat system and actuators to amplify the signal by a factor of 10. By having two input signals, adjacent actuators can operate asynchronously relative to each other, allowing for different modes of actuation. All actuators operate in synchronous when the two signals are in-phase. This mode of actuation is denoted as the two-dimensional mode. When the two signals are 180° out-of-phase, adjacent actuators operate out-of-sync relative to each other. This configuration is described as the three-dimensional actuation mode because it creates a three-dimensional effect on the surrounding flow. The two modes of actuation are identical to ones described by Seifert et al. (1998).

The effect of actuating frequency (f_a), and type of actuation (2D vs 3D) on separated flow will be investigated in this experiment. The actuator displacement (d_a) is indirectly controlled through the actuating frequency since the displacement grow near resonance frequency. All tests were conducted at the maximum voltage (V_{\max}) to generate the maximum displacement. The maximum operating voltage of the PL 128.10 actuator from Physik Instrumente is +30 V. Actuating frequencies ranging from 50 ($St = 0.8$) to 225 Hz ($St = 3.6$) in increments of 25 Hz ($St = 0.4$) will be tested.

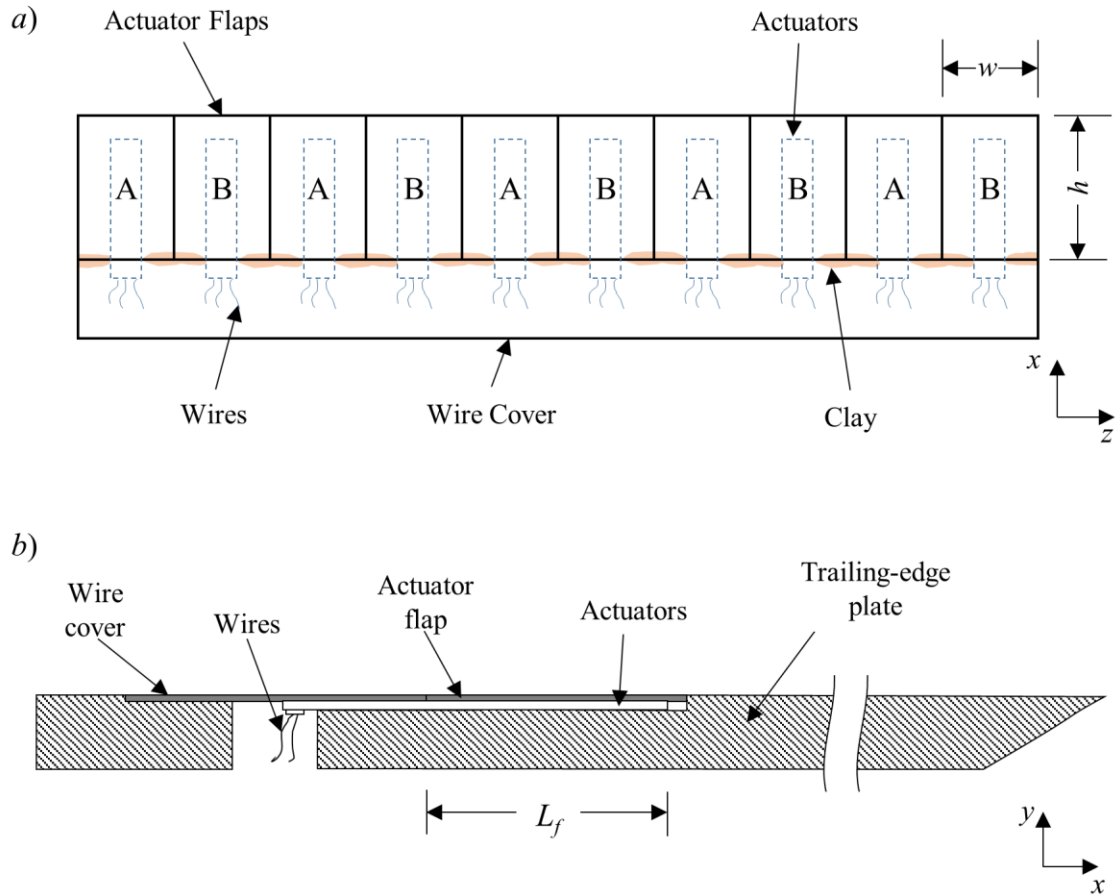


Figure 22. (a) Top view of the actuator array and (b) sectional view highlighting the placement of actuators. Two different signals, A and B, are fed to the ten actuators. The width, w , and height, h , of each actuator flaps are 20 mm and 30 mm respectively. The free length, L_f , of the actuator is 28 mm. Note that the L_f and h are slightly different.

3.4.2 Actuator Dynamics

According to the provided manufacturer specification, the PI piezoelectric actuator has a resonant frequency of 360 Hz. Since a thin piece of steel sheet was placed on top of the flapping actuator to increase the surface area of actuation, the resonant frequency of the actuator is decreased due to the added mass. It is necessary to characterize the frequency response of the actuator because it is desirable to operate the actuators close to resonant frequency to maximize actuator displacement (Blackwelder *et al.* 1998; Kim *et al.* 2013; Seifert *et al.* 1998; Zhang *et al.* 2012). Characterizing the dynamics of the actuators was done by recording the vibrating motion of actuator with a high-speed camera (Phantom v611) and then measuring the displacement between the lowest and highest point, i.e., the tip-to-tip displacement. A 200 mm macro lens was used to record the motion,

resulting in a digital resolution of $22.9 \mu\text{m pix}^{-1}$. Using this method to measure the tip displacement results in an error of ± 0.5 pixel, which equates to an error of $11.5 \mu\text{m}$. An error of $11.5 \mu\text{m}$ results in a relative error of approximately 3% at the smallest tip displacement. The motion of the actuator was recorded at 5 kHz and the frequency response is presented in Figure 23. The values shown in this figure correspond to the amplitude, which is half of the tip-to-tip displacement. From the results, it is concluded that the new resonant frequency is between 175 and 200 Hz.

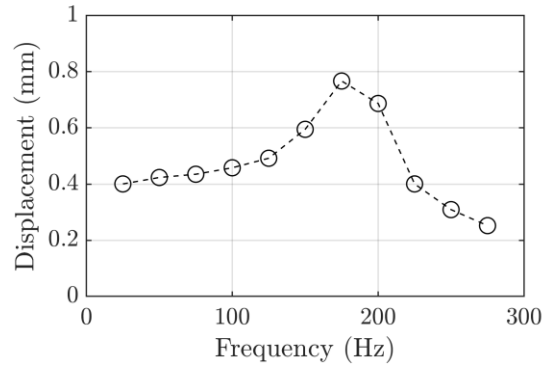


Figure 23. Dynamic response of the piezoelectric actuator with a $20 \times 30 \text{ mm}^2$ steel sheet mounted on top. The displacement here is defined as the amplitude, i.e., the maximum displacement from the off position.

3.4.3 Particle Image Velocimetry Setup

The near-surface flow downstream of the array of actuators was measured using a planar PIV setup similar to the one described in section 3.3.2. A fog generator was used to generate $1\text{-}\mu\text{m}$ droplets as tracer for flow visualization. The same dual-head Nd:YLF laser from Photonics Industries (DM20-527-DH) was used to illuminate the particles within the FOV. Various laser optics were used to shape the laser beam into a 2 mm thick sheet that was parallel to the flat section of the airfoil. The laser sheet was measured to be 2 mm away from the surface of the airfoil, which was consistent throughout the FOV. A Phantom v611 camera was used to record the motion of fog particles as shown in Figure 21. Each camera contained a 105-mm lens set to $f/4$. A distance of 1.5 m was measured between the front of the lens and the surface of the airfoil. The size of the FOV was $(\Delta x, \Delta z) = (171 \text{ mm}, 357 \text{ mm})$ with a digital resolution of 3.25 pix mm^{-1} .

Five sets of time-resolved images were collected at 2.5 kHz for 2 s for each configuration of flow control, totaling to 10 s of flow. All image preprocessing were done on Davis 8.4. Normalization of particle intensity and elimination of background noise were achieved

simultaneously through subtracting by the ensemble average. Afterwards, vectors were obtained through a sliding sum-of-correlation algorithm with a kernel size of $L = 2$ and no time delay. Multiple passes were used for vector calculation with a final interrogation window size of 32×32 pixels and 75% overlap. Vectors with a normalized residual value of larger than 2 were identified as an incorrect vector (Westerweel & Scarano 2005) and then replaced by interpolation. Incorrect vectors made up less than 2% of the total vectors. By considering the minimum resolvable velocity to be 0.02 pixels (Ghaemi *et al.* 2012), the error of the velocity vectors obtained through this experiment is 0.015 m s^{-1} ($0.001 U_\infty$).

Chapter 4. Three-dimensional turbulent-boundary layer separation over an airfoil

The separation of a turbulent boundary layer due to an APG is a phenomenon potentially observed in flow over airfoils, blades of a wind turbine, and within diffusers. As stated before, the consequence of separated flow in engineering application is a performance limit for the fluidic device. For example, the lift of an airfoil can be increased by increasing the angle of attack until shortly after the occurrence of separated flow. This is a strong incentive for developing a thorough understanding of and predictive models for flow separation. Current analytical models are limited to relatively low Reynolds number (Jones *et al.* 2008; Na & Moin 1998) because the computations require tremendous amounts of computational power. Experimental results are essential as a fundamental investigation, since they can be used for validation of computational results and aiding development of new analytical models.

Characterization of separated flow began by studying the flow within a two-dimensional streamwise-wall-normal plane. These studies neglect the inherent three-dimensionality of the flow phenomenon – it has been repeatedly shown that flow over a stalled two-dimensional airfoil results in a three-dimensional topology (Gregory *et al.* 1971; Moss & Murdin 1970; Winkelmann & Barlow 1980). Since separated flow naturally tend towards a three-dimensional topology, two-dimensionality can only be induced with modifications to the experimental setup. Gregory *et al.* (1971) and Coles & Wadcock (1978) attempted to create two-dimensional flow separation by suction/blowing along the walls. Gregory *et al.* (1971) observed that suction along the wall removed corner separations, but three-dimensionality remained in the mean flow pattern. Coles & Wadcock (1978), Thompson & Whitelaw (1985), and Wadcock (1987) succeeded in forcing a two-dimensional flow through implementation of vanes/fences along the sidewalls. Confirmation of two-dimensional separation was mostly achieved through either surface oil flow visualization or pressure profiles at the surface. Both these techniques reveal little about the flow's unsteadiness meaning the two-dimensionality was only confirmed for the mean flow. For this reason, it is difficult to say whether that the separation in some of these studies was truly two-dimensional, as instantaneous spanwise motion could exist.

A variety of surface topology have been associated with flow separation depending on the Reynolds number, angle of attack, airfoil aspect ratio and thickness, type of laminar-turbulent transition, and surrounding boundary condition (Broeren & Bragg 2001; Dell’Orso & Amitay 2018; Liu *et al.* 2011). A distinguished flow-separation pattern, which is also the focus of the present investigation, is an “owl-faced” skin-friction pattern known as a stall cell. This pattern was first observed by Winkelmann & Barlow (1980) and the counter-rotating swirls on the surface correspond to a saddle point and a pair of counter-rotating foci (Délery 2013). Stall cells have been observed on the suction side of thick airfoils that undergo a trailing-edge separation (Broeren & Bragg 2001) or leading-edge separation (Yon & Katz 1998) at the angle of attack of maximum lift and a few degrees beyond that into the post-stall regime (Dell’Orso & Amitay 2018; Yon & Katz 1998). However, there is also evidence of stall cells at angles of attack prior to that of the maximum lift. For an airfoil with 18% thickness and maximum-lift angle of attack of 9° , tuft visualization of Manolesos *et al.* (2014) showed a stall cell pattern at angles of attack as low as 7° . This angle is in the nonlinear pre-stall section of the lift curve. Ragni & Ferreira (2016) also observed a stall cell on a NACA 64-418 airfoil at an angle of attack of 11° while the maximum-lift angle of attack was 15° .

Because of the erratic nature of separated flow (Simpson 1989), it is also of interest to characterize the unsteadiness of an APG-induced separation. Previous experimental studies conducted on stall cells were performed using fine tufts (Yon & Katz 1998), SOFV (Dell’Orso & Amitay 2018; Winkelmann & Barlow 1980) or low frame-rate PIV (Dell’Orso & Amitay 2018; Manolesos & Voutsinas 2014b; Ragni & Ferreira 2016), which reveal limited information about its time-resolved behavior. As a result, little is known about the unsteadiness of stall cells and the motion of coherent structures present within the instantaneous velocity fields. Yon & Katz (1998) linked stall cells to the low frequency phenomenon observed by Zaman *et al.* (1989), which they attributed to a transition between a stalled and unstalled state. Duquesne *et al.* (2015) investigated the unsteadiness of flow separation in a turbine diffuser using two-dimensional PIV. By using a reduced-order model obtained through proper orthogonal decomposition (POD), they were able to filter out noise and small-scale structures in the skin-friction lines. Duquesne *et al.* (2015) observed that many saddle points and foci occupied the separation zone, and that the foci in the separation front are larger and more energetic than the turbulent vortices. However, more experiments are

required to extend such an analysis of the unsteady flow organization to airfoil trailing-edge separation.

The motivation of experiment I is to apply time-resolved PIV to study the unsteady topology of a trailing-edge separation formed on a thick airfoil in the nonlinear pre-stall regime. First, the boundary layer at mid-span is characterized and the results are compared with the previous literature including both two- and three-dimensional separations. Near-wall PIV performed at the separation region is used to obtain an approximation of the instantaneous and mean skin-friction lines. The skin-friction patterns are investigated with the goal of providing insight into the connection between instantaneous flow structures and the mean flow structure. Time-resolved PIV snapshots are then used to probe the instantaneous structure of the separation front. Finally, POD is applied to determine the most energetic motions in the near-wall plane.

4.1 Mean Flow Characteristics

In this section, the time-averaged statistics of the flow field, including mean velocity and Reynolds stresses, are analyzed. The measurements in the streamwise-wall-normal plane at the mid-span of the airfoil are compared with the literature on two- and three-dimensional separation, while the wall-parallel measurement plane is evaluated with respect to previous investigations of three-dimensional separation. All the statistics in this section are obtained from the cyclic data to ensure statistical convergence.

4.1.1 Turbulent Boundary Layer

The progression of the boundary layer profile with chordwise distance within FOV1 indicated in Figure 18 at mid-span is shown in Figure 24(a). Contours of the mean streamwise velocity are also shown in the background. The dashed line is located along $\langle U \rangle = 0$, with the positive contours located above and the negative contours located below. The streamwise coordinate was normalized by the chord length of the airfoil (c) and the wall-normal coordinate was normalized by the boundary layer thickness (δ_{99}) obtained at $x/c = -0.15$, which is 26.3 mm. The mean separation point is evident from the detachment of the boundary layer from the surface at $x/c = 0$, which is followed by a recirculation region with backflow.

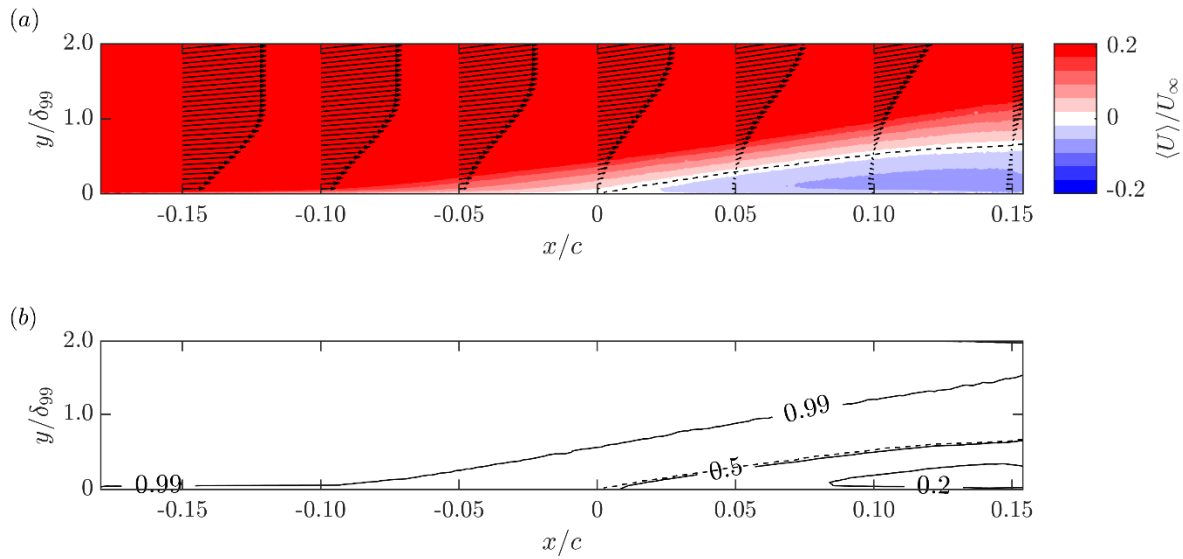


Figure 24. (a) Vectors of mean velocity at various chordwise positions upstream and downstream of the mean separation point ($x/c = 0$). The vector profiles are shown in $0.05c$ increments and the vectors are downsampled by a factor of 6 in the y -direction for clarity of the visualization. Contours of the normalized mean streamwise velocity, $\langle U \rangle / U_\infty$, are shown in the background. Positive contours are above the dashed line and negative contours are located under the dashed line. (b) Contour lines of the backflow parameter (γ) in the x - y plane. The dashed line indicates where the mean streamwise velocity is zero.

The shape factor of the boundary layer (H , the ratio of displacement and momentum thicknesses) at $x/c = -0.15$ is 2.1, which is larger than the typical value of roughly 1.3 for a turbulent boundary layer with zero pressure gradient (ZPG) (Schlichting & Gersten 2016). As expected, this is because the boundary layer is subject to an APG, and the effect is evident even at the most upstream region of the FOV. A reduction of streamwise velocity and an increase of wall-normal velocity are observed with downstream distance. In Table 3, the variation of both velocity components is shown for the farthest measurement data from the wall at $y = 2\delta_{99}$, which is indicated with ∞ and x subscripts for the specified streamwise position. The boundary layer thickness (δ_{99}), displacement thickness (δ^*), momentum thickness (θ), and shape factors (H) of the upstream boundary layer are also provided. The values are only provided up to $x/c = 0$ because the boundary layer thickness falls outside the FOV downstream of the mean separation point.

The effect of the APG can also be seen from the wall-normal velocity gradient ($\partial \langle U \rangle / \partial y$) of the velocity profile in Figure 24(a). As the mean separation point is approached, the wall-normal velocity gradient of the boundary layer decreases and the velocity profile loses the fullness that is

exhibited by a turbulent-boundary layer in ZPG. The change is highlighted by the increase of the shape factor with downstream distance. A value of $H = 3.6$ is reached at the mean separation point. This value is similar to the shape factors obtained by previous studies of two-dimensional separation performed by Wadcock (1987), Holm & Gustavsson (1999), and Angele & Muhammad-Klingmann (2006). A reduced shape factor of 2.85 was reported in the experiments conducted by Dengel & Fernholz (1990). The difference may be attributed to the fact that their investigations were performed over an axisymmetric body rather than a flat surface.

Contours of the backflow parameter (γ) are shown in Figure 24(b). Once again, the line of zero mean streamwise velocity is shown by the dashed line in Figure 24(b), which coincides with the contour line $\gamma = 0.50$. The contour line $\gamma = 0.50$ originates from a point on the surface known as the transitory detachment point (Simpson 1989) that is also close to the origin here. As expected, the probability of backflow increases with increasing downstream distance.

x/c	$U_{\infty,x}$ [m s ⁻¹]	$V_{\infty,x}$ [m s ⁻¹]	δ_{99} [mm]	δ^* [mm]	θ [mm]	H
-0.15	12.83	1.21	26.3	9.3	4.3	2.1
-0.10	12.33	1.30	31.5	12.6	5.1	2.5
-0.05	12.10	1.49	37.8	17.2	5.9	2.9
0.00	11.89	1.69	45.5	23.2	6.4	3.6

Table 3. Boundary layer parameters for various positions upstream of and at mean separation.

4.1.2 Reynolds Stresses and Turbulence Transport at Mid-Span

The normal and shear Reynolds stresses in the x - y plane are normalized by the freestream velocity and shown in Figure 25. All three Reynolds stresses exhibit a similar trend: the local peak of the wall-normal profiles moves away from the wall with increasing streamwise distance. Previous researchers have also observed a similar distribution of the Reynolds stresses in a streamwise-wall-normal plane within two-dimensional (Angele & Muhammad-Klingmann 2006; Thompson & Whitelaw 1985) and three-dimensional separation (Elyasi & Ghaemi 2019; Manolesos & Voutsinas 2014b). These authors attributed the trend to the separation of the boundary layer and the roll up of vortices. The roll up of vortices due to separation also increases turbulence mixing in this region, as indicated by the high intensity region of the $\langle uv \rangle / U_{\infty}^2$ distribution in Figure 25(c). Minimal shear stress is seen in the backflow region under the dashed line of $\langle U \rangle = 0$, which indicates negligible mixing inside the recirculation region.

The transport of streamwise turbulent kinetic energy due to streamwise and wall-normal fluctuations is evaluated using the third-order central moments $\langle u^3 \rangle / U_\infty^3$ and $\langle u^2 v \rangle / U_\infty^3$, respectively. The results are shown using the contours of $\langle u^3 \rangle / U_\infty^3$ and $\langle u^2 v \rangle / U_\infty^3$ in Figure 26(a) and (b), respectively. The distributions are similar to those obtained by Elyasi & Ghaemi (2019) from an APG-induced three-dimensional separation inside a diffuser. In both the current investigation and the one by Elyasi & Ghaemi (2019), the flow is broken down into two layers: an outer region and an inner region. The outer region contains negative $\langle u^3 \rangle / U_\infty^3$ and positive $\langle u^2 v \rangle / U_\infty^3$ and suggests that streamwise turbulent kinetic energy is transported away from the wall through ejection motions, i.e. negative u and positive v . In contrast, the inner region contains positive $\langle u^3 \rangle / U_\infty^3$ and negative $\langle u^2 v \rangle / U_\infty^3$, which indicates that streamwise turbulence is transported through sweeping motions, i.e. positive u and negative v .

Comparing the present results to those from past investigations reveals that there are similarities between different separated flows when the streamwise-wall-normal plane at mid-span is viewed. For example, all two and three-dimensional separations have shown that the boundary layer profile undergoes a similar transformation leading up to the mean separation point. Similar behavior of the Reynolds stresses is also observed; the local peak stress moves away from the wall with the separation of the boundary layer, accompanied by an increase of the Reynolds stresses and broadening of the associated peaks with downstream distance. Increasing of the Reynolds stress and broadening of the peak was also observed for separated flow over a smooth contoured ramp (Song & Eaton 2002), backward-facing step (Scarano & Riethmuller 1999), and a flat plate with a trailing flap (Thompson & Whitelaw 1985). The results for the third-order central moments presented here are also in agreement with Elyasi & Ghaemi (2019). These similarities were observed despite the fact that the three-dimensional topologies of the flows were different. The agreement suggests that the separated boundary layer and the roll-up of the shear layer, which is the common feature between these flows, has a major contribution to the Reynolds stress and turbulence transport in the streamwise-wall-normal plane.

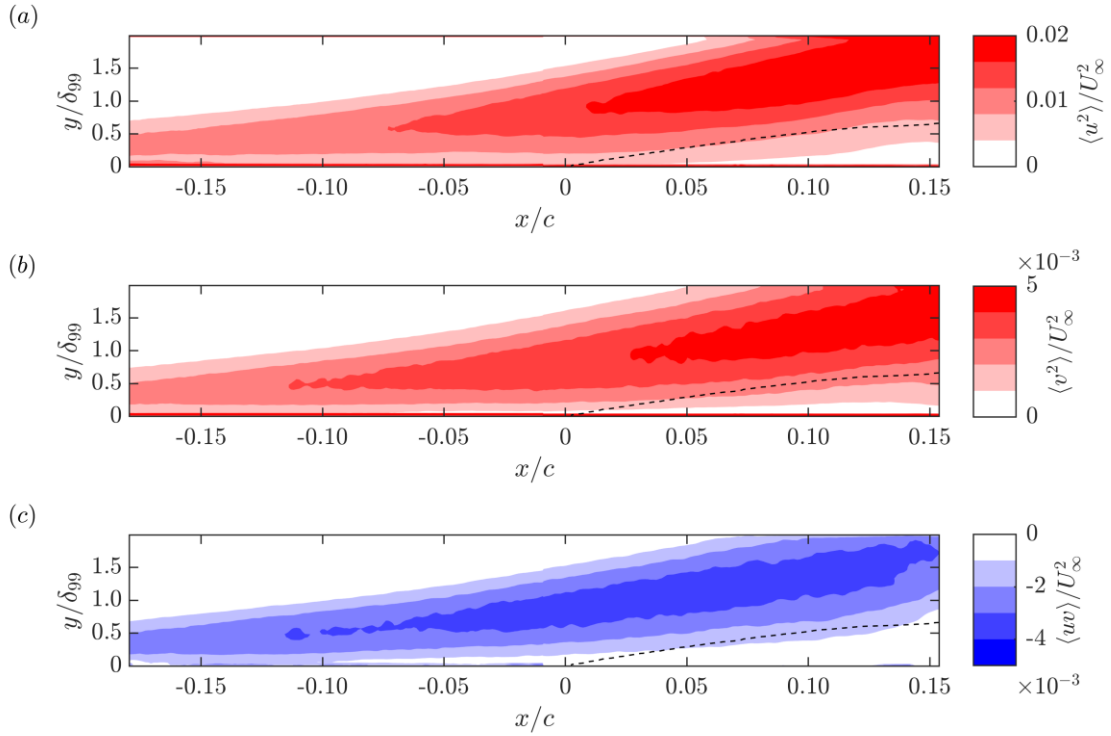


Figure 25. Contours of (a) streamwise (b) and wall-normal Reynolds stresses, and (c) Reynolds shear stress in the x - y plane. The dashed line shown in the figures indicates $\langle U \rangle = 0$. The values are normalized using the freestream speed of the wind tunnel U_∞ .

4.1.3 Mean Skin-Friction Lines

The mean velocity field in FOV2 displayed in Figure 27(a) is used to gain insight into the near-wall topology in the vicinity of the separation front. The measurement plane is located at $y = 2$ mm, equating to $0.08\delta_{99}$ where δ_{99} is the boundary layer thickness at the most upstream position in the FOV ($x/c = -0.15$). The near-wall streamlines obtained in this plane are expected to be similar to the skin-friction lines with minor positional discrepancies according to the investigation of Depardon *et al.* (2005). They studied separated flow around a cube and observed topological consistency when the measurement plane is underneath the location of the main streamwise and spanwise vortical structures. For wall-normal vortices, the near-wall PIV measurements are not expected to deviate from the skin-friction topology except for minor positional discrepancies

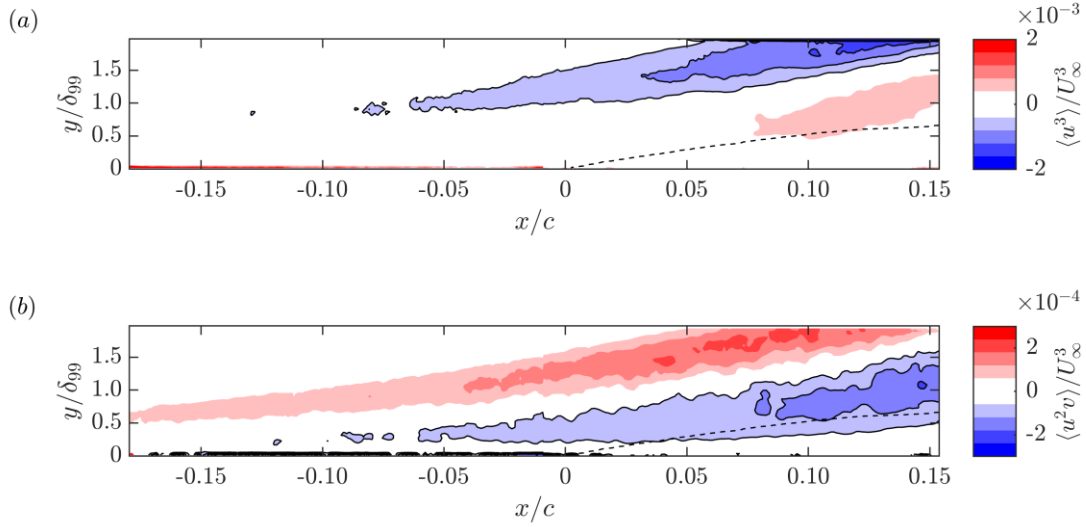


Figure 26. Contours of the third-order central moments (a) $\langle u^3 \rangle / U_\infty^3$ and (b) $\langle u^2 v \rangle / U_\infty^3$ in the x - y plane. The turbulence transport terms are normalized by the freestream speed of the wind tunnel U_∞ . The dashed line shown in the figures indicates $\langle U \rangle = 0$. Contours enclosed with solid lines denote negative values and contours without solid borders denote positive values.

The near-surface streamlines superimposed on the contours of streamwise velocity magnitude in Figure 27(a) reveal a three-dimensional separation. A saddle point is present near mid-span and a pair of counter-rotating foci are located at the sides, forming the stall-cell pattern. Such a stall cell pattern has been traditionally observed for thick airfoils at post-stall condition (Broeren & Bragg 2001; Dell’Orso & Amitay 2018; Manolesos & Voutsinas 2014b; Winkelmann & Barlow 1980). However, Manolesos *et al.* (2014) and Ragni & Ferreira (2016) reported a stall cell for thick airfoils in the nonlinear pre-stall regime of the lift versus angle of attack curve. The detachment-type separation line, shown in Figure 27(a) as a dashed line, rolls into the foci and forms tornado-like vortices. The separation line reveals an undulating pattern across the span. Spanwise motion is present at both spanwise sides of the saddle point immediately upstream of the separation line. This is explained by the tendency of flow to escape in the spanwise direction in the presence of an APG. In Figure 27(b), the FOV captured most of the incipient detachment points ($\gamma = 0.99$) in the upstream region with exception to the mid-span region as shown by the contours of γ . It is noted that there are no points within the FOV where the flow is downstream ($U > 0$) or reversed ($U < 0$) at all instances, showcasing the intermittency of the flow and the large spatial influence of the present separation.

The distance between the two foci in the present study is approximately $0.17s$ (or $0.21c$). Manolesos & Voutsinas (2014a) reported a minimum stall cell width of $0.25s$ for an airfoil with unspecified camber, an aspect ratio of 1.5, and Re_c of 1.5×10^6 . Stall cell width in their investigation include the distance between the outer edges of the two foci, which means the distance between the two foci would have been less than $0.25s$. They also applied zig-zag tape over only 10% of the span to stabilize the stall cell. Dell’Orso & Amitay (2018) observed a stall cell with an estimated distance of $0.18s$ between the two foci for Reynolds numbers between $Re_c = 4.0 \times 10^5$ and 4.5×10^5 . Their study was conducted on a symmetric NACA 0015 airfoil with an aspect ratio of 4.0 and no trip wire was applied. It is also important to note that the stall cell observed by Dell’Orso & Amitay (2018) was in the post-stall regime while the smallest stall cell of Manolesos & Voutsinas (2014a) was observed for trailing-edge separation in the pre-stall regime. Considering the potential effects of angle of attack, airfoil profile, aspect ratio, type of laminar to turbulent transition, and Reynolds number, the size of the stall cell observed here is comparable to the observations of Manolesos & Voutsinas (2014a) and Dell’Orso & Amitay (2018).

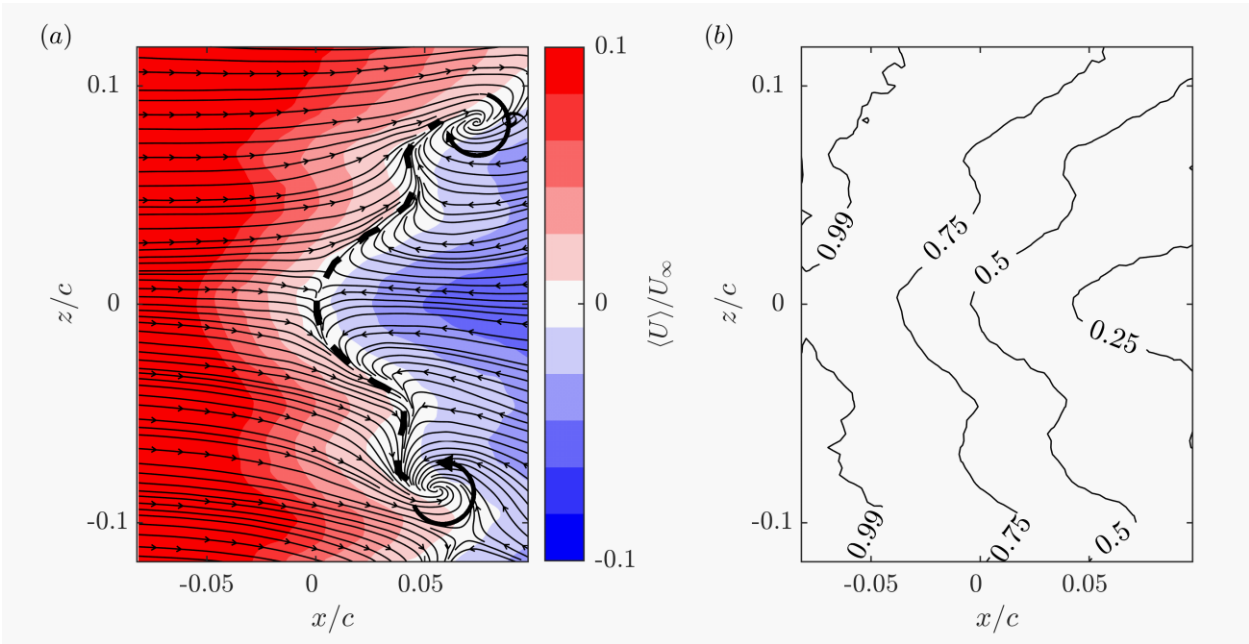


Figure 27. (a) Streamlines obtained from the mean flow in the near-surface ($y = 2 \text{ mm}$) plane. Colors in the background represent the mean streamwise velocity normalized by freestream speed of the wind tunnel U_∞ . The positive and negative contours can be identified based on the streamwise direction of the streamlines. (b) Contour lines of the backflow parameter (γ) in the near-surface plane, showing intermittency of the separated flow.

4.1.4 Reynolds Stresses of the Near-Wall Plane

Reynolds stress contours in the near-wall x - z plane are presented in Figure 28. Once again, the stress terms were normalized by the square of the freestream speed. The contours of $\langle u^2 \rangle / U_\infty^2$ and $\langle w^2 \rangle / U_\infty^2$ both reveal a symmetric pattern about mid-span. By comparing the γ contours in Figure 27(b) with the distribution of normal Reynolds stresses, it is evident that the largest $\langle u^2 \rangle / U_\infty^2$ and $\langle w^2 \rangle / U_\infty^2$ exist just upstream of where the separation line is most likely to be located (i.e. $\gamma \approx 0.50$). The increased fluctuation of both streamwise and spanwise velocity in this region indicates the large turbulence and intermittency of the flow structures that are present at the separation front. Downstream of the mean separation line, both $\langle u^2 \rangle / U_\infty^2$ and $\langle w^2 \rangle / U_\infty^2$ begin to decrease as the shear layer detaches from the surface and departs from the x - z plane of PIV. This agrees with the stress contours in the streamwise-wall-normal plane (Figure 25), which show little mixing in the vicinity of the wall within the recirculation region.

The contours of the Reynolds shear stress shown in Figure 28(c) are different from the contours of the normal stresses, as large magnitudes of shear stress appear in streamwise-elongated streaks. The streaks of large $\langle uw \rangle / U_\infty^2$ near $z/c = \pm 0.03$ are located along the detachment lines emanating from the saddle point of the mean flow. The secondary regions of large $\langle uw \rangle$ at $z/c = \pm 0.08$ are located at the same spanwise position as the two counter-rotating foci. There is also a deficit region of $\langle uw \rangle / U_\infty^2$, which is also elongated in the streamwise direction, and overlaps with the undulating part of the separation line at $z/c = \pm 0.05$.

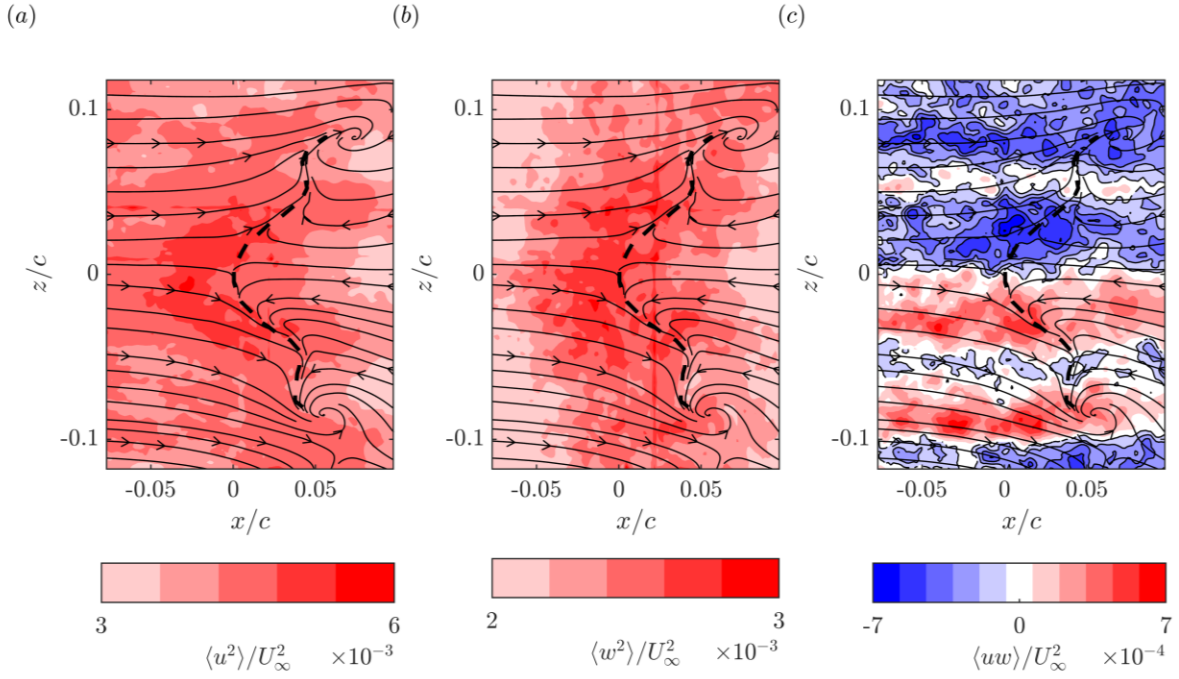


Figure 28. Contours of (a) streamwise and (b) spanwise components of Reynolds normal stress, and (c) Reynolds shear stress in the x - z plane. The near-surface streamlines obtained from the mean flow are superimposed on the contours. The negative contours are shown with solid black outlines.

4.2 Unsteady Flow Characteristics

The unsteady organization of the stall cell is investigated here by an initial evaluation of the energy spectrum of velocity fluctuations. Once the frequency range that forms the bulk of the turbulent kinetic energy is identified based on the spectrum, a low-pass filter is used to isolate the coherent motions. The filtered vector fields are also used to investigate the organization of the critical points and formation mechanism of the stall cell. Afterwards, the relationship between high-speed streaks and instantaneous separation structures is developed by comparing their spatial organizations.

4.2.1 Energy Spectra

A discrete Fourier transform (DFT) was performed on the fluctuating velocity components obtained from the time-resolved images in FOV2 (Figure 18) to identify the energy spectrum of the frequencies present in the flow. Welch's method was used to reduce spectral variance by performing DFT over overlapping segments and then averaging the results (Heinzel *et al.* 2002).

Hanning windows with 50% overlap were applied to the segments to achieve amplitude flatness among all data points (Heinzel *et al.* 2002). A segment length of 0.50 s (874 images) was used, resulting in a frequency resolution of 2.0 Hz. The spectral density was evaluated for each set of time-resolved data (2.86 s) and then averaged (5 sets in total).

The power spectral density (PSD) of the fluctuating streamwise velocity is presented in Figure 29(a) and the PSD of the fluctuating spanwise velocity is shown in Figure 29(b). Three points of interest along the mid-span ($z = 0$) were selected: one upstream of the mean separation ($x/c = -0.05$), one at the saddle point ($x/c = 0$), and another within the region of reverse flow ($x/c = 0.05$). The three points were selected to determine the change of the frequency spectrum with increasing probability of backflow (i.e. decreasing γ). Spectral analysis of the fluctuating velocities at locations away from mid-span were also investigated and yielded similar results.

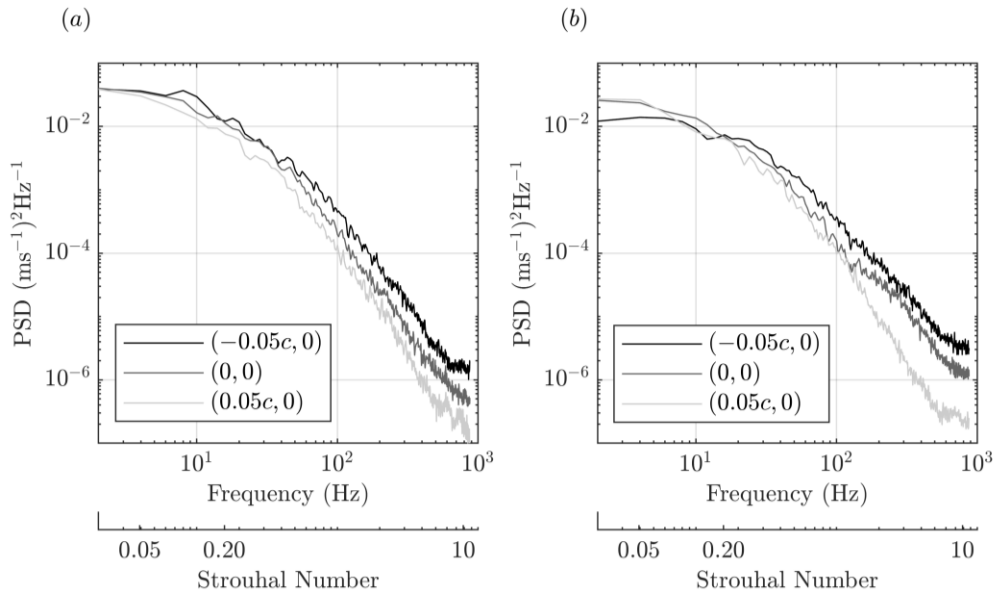


Figure 29. Power spectral density (PSD) of the fluctuating (a) streamwise and (b) spanwise velocity at a location upstream of the mean separation point ($x/c = -0.05$), at the saddle point ($x/c = 0$), and a point in the backflow region ($x/c = 0.05$) along mid-span ($z = 0$).

As is evident in the plots of Figure 29, the low-frequency fluctuations have a large kinetic energy at all three points. The energy of the velocity fluctuations decreases sharply with increasing frequency. No strong local peak is observed in the PSD, indicating the absence of a strong periodic shedding process. At the low frequency range of the spectra, the streamwise PSD shows a similar energy for all three points. However, at higher frequencies, the energy reduces with streamwise

distance. Since the backflow parameter also decreases with streamwise distance, the reduced high-frequency energy coincides with a larger probability of backflow motions.

Considering spanwise velocity fluctuations in Figure 29(b), the low-frequency energy is smaller at the upstream point than it is at mean separation and within the backflow region. Investigation of the data at spanwise locations of $z/c = \pm 0.05$ and ± 0.10 also revealed smaller energy of low-frequency content at locations upstream of the mean separation line. The PSD at $z/c = \pm 0.05$ and ± 0.10 are excluded for brevity. At higher frequencies, the energy at the upstream points is larger. This trend indicates presence of strong low-frequency spanwise motions at the separation point and its downstream locations (i.e. regions where $\gamma \leq 0.50$) as the flow turns in the spanwise direction in response to the APG. The presence of the spanwise motions was evident in the mean flow of Figure 27(a) and $\langle w^2 \rangle$ contours of Figure 28(c).

Zaman *et al.* (1989) conducted a study on the oscillation of flow around a stalled airfoil and concluded that bluff body vortex shedding appeared during deep stall at high angles of attack with a Strouhal number of 0.2. The Strouhal number was evaluated by normalizing the frequency, f , by the projected height of the airfoil and the freestream speed ($St = fc \sin\alpha/U_\infty$). At lower angle of attack, the vortex shedding frequency was replaced with a Strouhal number in the range of 0.02 to 0.05, which was associated with a shallow stall due to trailing-edge separation. Similar low-frequency phenomenon was observed by Yon & Katz (1998) for stalled airfoils that showed stall cell pattern. Zaman *et al.* (1989) attributed this low-frequency fluctuation to the transition of flow between a stalled and unstalled state. The second horizontal axis of Figure 29 shows St , estimated using $fc \sin\alpha/U_\infty$. Most frequency content contained within the flow appears to be less than the bluff body shedding frequency of $St = 0.20$. This agrees with the intermittency of trailing-edge separation as it is constantly alternating between forward and reverse flow, i.e. separated and attached.

4.2.2 Spatial Organization of Critical Points

A sample snapshot of the instantaneous skin-friction lines is presented in Figure 30(a) along with background contours of the normalized instantaneous streamwise velocity (U/U_∞). This figure provides a glimpse at the complicated nature of the flow field under investigation. The relatively parallel skin-friction at the upstream boarder of the FOV becomes chaotic as the flow evolves from an attached boundary layer to a separated flow with patches of backflow. The instantaneous

separation line is not well-defined in the visualization. Saddle points, foci, and nodes can be observed throughout. These structures are intertwined with each other and the small-scale turbulence, making it hard to isolate individual structures. There is also no distinct resemblance of a stall cell in this instantaneous visualization. In Figure 30(b), background contours of two-dimensional Q -criterion (Jeong & Hussain 1995) are used to show vortices with strong local rotation within the FOV. Although several patches of large Q are observed, no distinct pair of counter-rotating vortices is observed to guide us toward identifying a stall cell pattern.

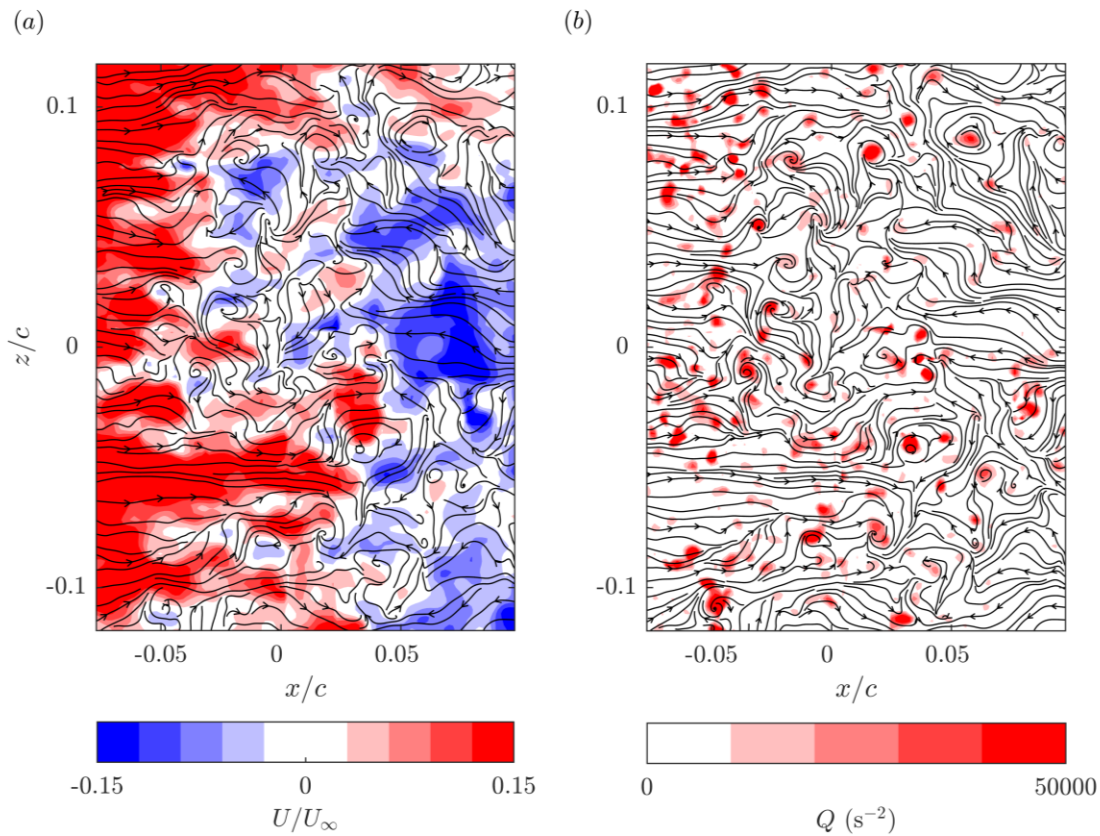


Figure 30. Snapshot of the instantaneous near-surface streamlines with a background contour of (a) normalized streamwise velocity and (b) two-dimensional Q -criterion. The sign of the contours in (a) can be identified using the streamwise direction of the streamlines.

In order to remove the small-scale, high-frequency structures from the instantaneous snapshots, a moving average filter is applied to the time-resolved data. The filter is used to isolate the low-frequency motion shown in the spectral analysis of Figure 29 and observed in past studies (Yon & Katz 1998; Zaman *et al.* 1989). The moving average filter acts as a low-pass filter with a -3 dB cutoff frequency at $St = 0.05$, which was chosen based on the values provided by Zaman *et*

al. (1989). They stated that the low frequency motions associated with a mild stall have a non-dimensional frequency between $St = 0.02$ and 0.05 . Yon & Katz (1998) later connected this low frequency motion to airfoils with stall cell pattern. This cutoff frequency corresponds to a kernel size of $k = 200$ snapshots for the image acquisition frequency of 1750 Hz, which spans over 0.114 s. The instantaneous snapshot of Figure 30 has been filtered as described above and is shown in Figure 31(a) with normalized instantaneous velocity and in Figure 31(b) with Q -criterion in the background.

At first glance of the skin-friction lines in Figure 31, it is observed that the majority of the small turbulent vortices with a shorter lifetime have been removed from the snapshot due to filtering. The separation structures also appear to be more identifiable through visual inspection. The separation front is three-dimensional and made up of many local separation lines forming from small-scale saddle points. A few of these local separation lines are shown by the dashed lines in Figure 31(a). All these separation lines pass through a saddle point and the neighboring skin-friction lines converge as they approach the separation line. However, even after application of the filter, there is no distinct separation line that extends across the entire spanwise length of the FOV as seen in the mean flow of Figure 27(a).

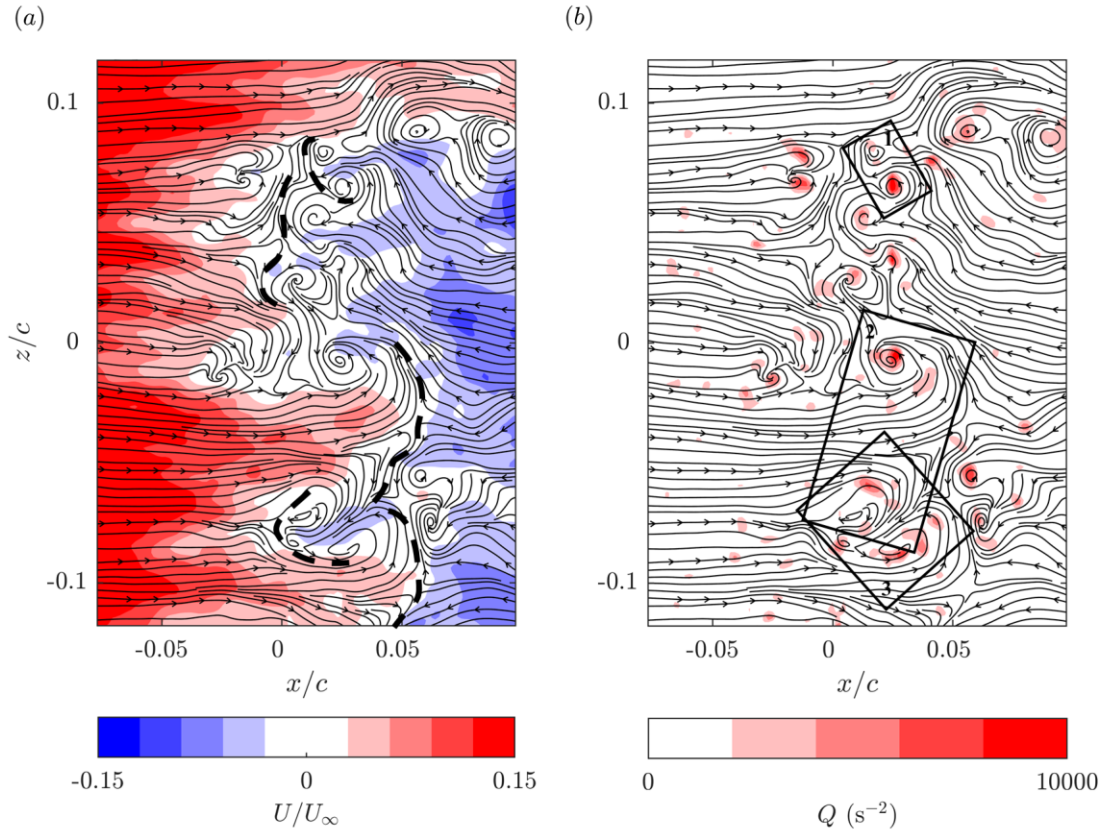


Figure 31. Filtered streamlines of the instantaneous velocity field in Figure 30 with (a) instantaneous streamwise velocity and (b) two-dimensional Q -criterion shown in the background. A moving average filter with cutoff frequency at $St = 0.05$ was applied. Once again, the color of the contours in (a) can be identified through the streamwise direction of the streamlines.

According to Surana *et al.* (2006), the separation line emanating from a saddle point must terminate at either a node or focus, which is true for the instantaneous skin-friction lines shown in Figure 31. The local separation lines sometimes terminate in a pair of counter-rotating foci as identified by the three rectangular boxes in Figure 31(b), resulting in “instantaneous stall cells” that are smaller than the stall cell in the mean skin-friction pattern. It is also possible for two separation lines to terminate at the same focus as highlighted by the overlap of the instantaneous stall cells identified by boxes 2 and 3 in Figure 31(b). By inspecting the visualizations, the width of these instantaneous stall cells (i.e. distance between the two foci) can range from $0.02s$ to $0.06s$ ($0.02c$ to $0.07c$), which is an order of magnitude smaller than the width of the mean stall cell.

Further inspection of Figure 31 shows two types of stall cell in this instantaneous visualization based on the flow direction between the foci pair and the relative location of the saddle point.

There are local stall cells with a strong backward flow motion such as the ones identified in rectangles 1 and 3. The saddle point of these stall cells is pushed to the upstream side of the foci pair. The second type of stall cell consists of a strong inrush of forward flow as shown in rectangle 2. As a result, the saddle point is observed on the downstream side of the foci. Based on the direction of the flow between the foci pair, these two structures will be referred to as backward and forward stall cells, respectively.

The above analysis was repeated using a low-pass filter with different cutoff frequencies, which varied from $St = 0.02$ to 0.2 . In general, the number of critical points increased with increasing cutoff frequency due to the appearance of a larger number of small-scale structures. At the highest cutoff frequency of $St = 0.2$, the organization of instantaneous stall cells became intertwined with small-scale structures, thus making the instantaneous structures less apparent. For the lowest cutoff of $St = 0.02$, it appeared that the instantaneous stall cell were partially filtered. However, the small instantaneous stall cells were present in all cases.

The low-pass filtered velocity fields from FOV2 have also been used to detect the critical points and track them in time using the algorithm described in section 3.3.3. A visualization of the trajectories of saddle points, clockwise (CW) foci, and counter-clockwise (CCW) foci based on 1.0 s of time-resolved data are shown in Figure 32(a). The left-side axes of the plot show the x and z coordinates of the critical points while the horizontal axis shows time. The figure indicates that the translations of the critical points in the x and z directions are small since most of the tracks appear as relatively straight lines. The average streamwise advection velocity, $\langle U_a \rangle$, and the average streamwise advection speed, $\langle |U_a| \rangle$, for saddle points and foci were calculated from the detected tracks and are shown in Table 4. The same calculation is also carried out for the average spanwise advection velocity, $\langle W_a \rangle$, and its speed, $\langle |W_a| \rangle$. Here, the absolute operator, $|\dots|$, is applied to isolate the effect of the direction. All five sets of filtered time-resolved datasets were considered to obtain the values shown in Table 4. Statistical convergence of the advection velocities was verified by plotting the parameter against the number of sample points used for its calculation. The convergence tests showed that the values have statistically converged to their mean values. The random error of the values presented in Table 4 were determined by finding the difference between the maximum and minimum value (the range) for the trailing 20% of the convergence curve.

Advection of the saddle and focus points is observed in both the streamwise and spanwise directions as they both possess finite $\langle |U_a| \rangle$ and $\langle |W_a| \rangle$ values. The sign of $\langle U_a \rangle$ is positive for saddle and focus points, revealing that, on average, these structures tend to move in the downstream direction. However, the larger value of $\langle |U_a| \rangle$ with respect to $\langle U_a \rangle$ indicates that there is also a significant amount of backward advection in the upstream direction. Since saddle points and foci form along the separation lines of the instantaneous stall cells, the advection of these critical points is associated with movement and intermittency of the separation lines. Consequently, the separation lines are also expected to move in both the upstream and downstream directions with a slight tendency towards the downstream direction. The spanwise advection speed of the structures is also comparable with their streamwise speed. However, there is no spanwise preference as the average spanwise advection, $\langle W_a \rangle$, is negligible.

Advection Velocity ($\times 10^{-4}$)	Saddle Points	CW Foci	CCW Foci
$\langle U_a \rangle / U_\infty$	31 \pm 2.1	38 \pm 2.5	35 \pm 1.7
$\langle U_a \rangle / U_\infty$	144 \pm 1.7	135 \pm 3.1	130 \pm 1.0
$\langle W_a \rangle / U_\infty$	-3 \pm 1.5	2 \pm 1.2	-10 \pm 3.6
$\langle W_a \rangle / U_\infty$	113 \pm 1.2	88 \pm 3.7	89 \pm 1.0

Table 4. Advection velocities and speed of saddle points and foci evaluated based on the tracks detected in five sets of filtered time-resolved data.

The tracks of saddle points and foci have been projected onto the x - z plane and presented in Figure 32(b) and (c), respectively. These figures visualize the motion of the critical points in the x - z plane and approximate their probability density distributions. In both figures, the location of the critical points forms a V-shape distribution, similar to the pattern of the mean stall cell. The saddle points in Figure 32(b) are evenly distributed between both halves of the span. In Figure 32(c), the tracks of clockwise foci are shown in dark gray (green) while the tracks of counter-clockwise foci are shown in light gray (yellow). It is evident that the counter-clockwise foci are localized at the bottom of the FOV, while foci with clockwise rotation are centralized at the top. This preferential concentration of the foci structures is believed to form the foci pair of the mean stall cell pattern that was observed in Figure 27(a), i.e. the average of counter-clockwise foci located at the bottom of the FOV forms the large mean counter-clockwise focus in the mean-velocity field, and vice versa for the clockwise focus that appears at the top of the FOV.

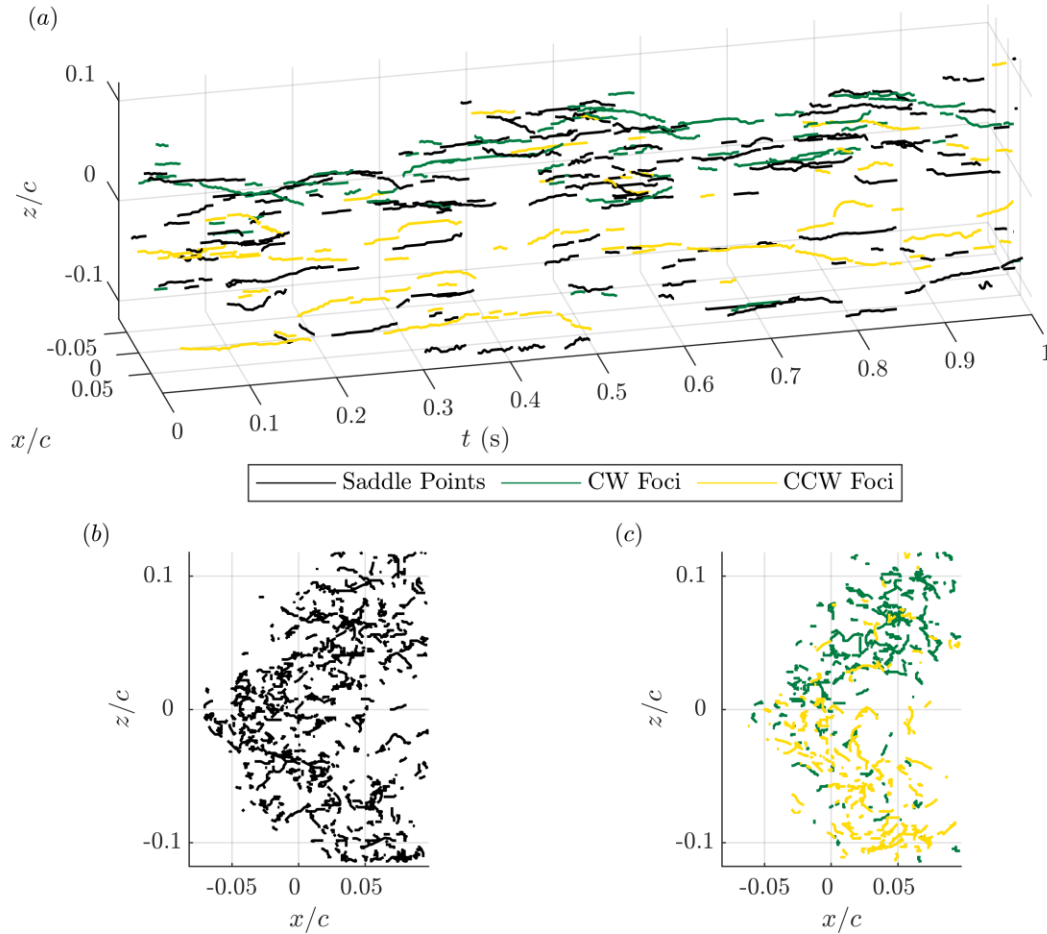


Figure 32. (a) Visualization of the detected tracks of saddle points, clockwise foci, and counter-clockwise foci over 1.0 s. Saddle points, clockwise foci, and counter-clockwise foci are shown with black, medium gray (green), and light gray (yellow) tracks, respectively. Tracks shown in the figures have a minimum length of 25 frames (0.014 s). The lower two plots show projections of the locations of the (b) saddle points and (c) foci obtained from 2.5 s of time-resolved data onto the x - z plane.

4.2.3 Instantaneous Forward and Backward Stall Cells

Inspection of the time-resolved skin-friction lines shows that foci pairs tend to form near regions of strong local flow at the separation front. This local flow results in high shear and the formation of counter-rotating, tornado-like vortices (the foci pair). In one presently observed scenario, the strong local flow originates from an influx of streamwise momentum from upstream flow in the form of a single high-speed streak. The high-momentum flow pierces an already existing

separation front and forms the foci pair. The resultant skin-friction pattern is a saddle point with a pair of counter-rotating foci, i.e. an instantaneous stall cell. The motion corresponding to this topology is separation via a pair of tornado-like vortices (Délery 2013). As shown in the visualization of Figure 31, these instantaneous stall cells can exist with either forward or backward orientations. In contrast to the above description, the latter forms as a result of a strong backflow from the downstream side of the separation front. By identifying the instantaneous stall cells as a pair of tornado-like vortices (Délery 2013), it is hypothesized that streamwise momentum is converted into wall-normal momentum during the formation of these structures.

The instantaneous stall cell formation described above is visualized in Figure 33. Figure 33(*a* – *d*) show the formation of a forward stall cell due to a strong downstream flow, while Figure 33(*e* – *f*) show the formation of a backward stall cell due to a strong backflow. The process is demonstrated through carefully selected timestamps here. Once again, these streamlines were obtained from the filtered data described in section 4.2.2. The subfigures contain a zoomed-in view of the structures with normalized instantaneous streamwise velocity (U/U_∞) plotted in the background of the streamlines. The separation lines of nearby saddle points are represented by dashed lines to highlight the movement of the instantaneous separation line.

Figure 33(*a*) reveals the skin-friction lines before the influx of streamwise momentum. The dashed lines in the subfigure are clearly separation lines because neighboring skin-friction lines converge towards it. The local separation line on the left comes from a saddle point that is outside of the cropped FOV. After 0.055 s, a pair of foci is formed due to an inrush of strong streamwise flow as indicated by the arrow in Figure 33(*b*). The centers of the two foci are located at approximately $(x/c, z/c) = (0, 0)$ and $(0.01, -0.03)$ in the figure. The two foci indicate that the local flow ejects from the surface via a pair of tornado-like vortices that contain both spanwise and wall-normal momentum. As the incoming momentum subsides (Figure 33(*c*)), the pair of foci eventually disintegrates and smaller, unstable structures are left behind as shown in Figure 33(*d*). The formation process of a backward stall cell is the same but is spatially reversed as can be seen in Figure 33(*e* – *h*). The strong backflow seen in Figure 33(*f*) results in a pair of foci located at $(x/c, z/c) = (0, 0.01)$ and $(0.01, -0.03)$.

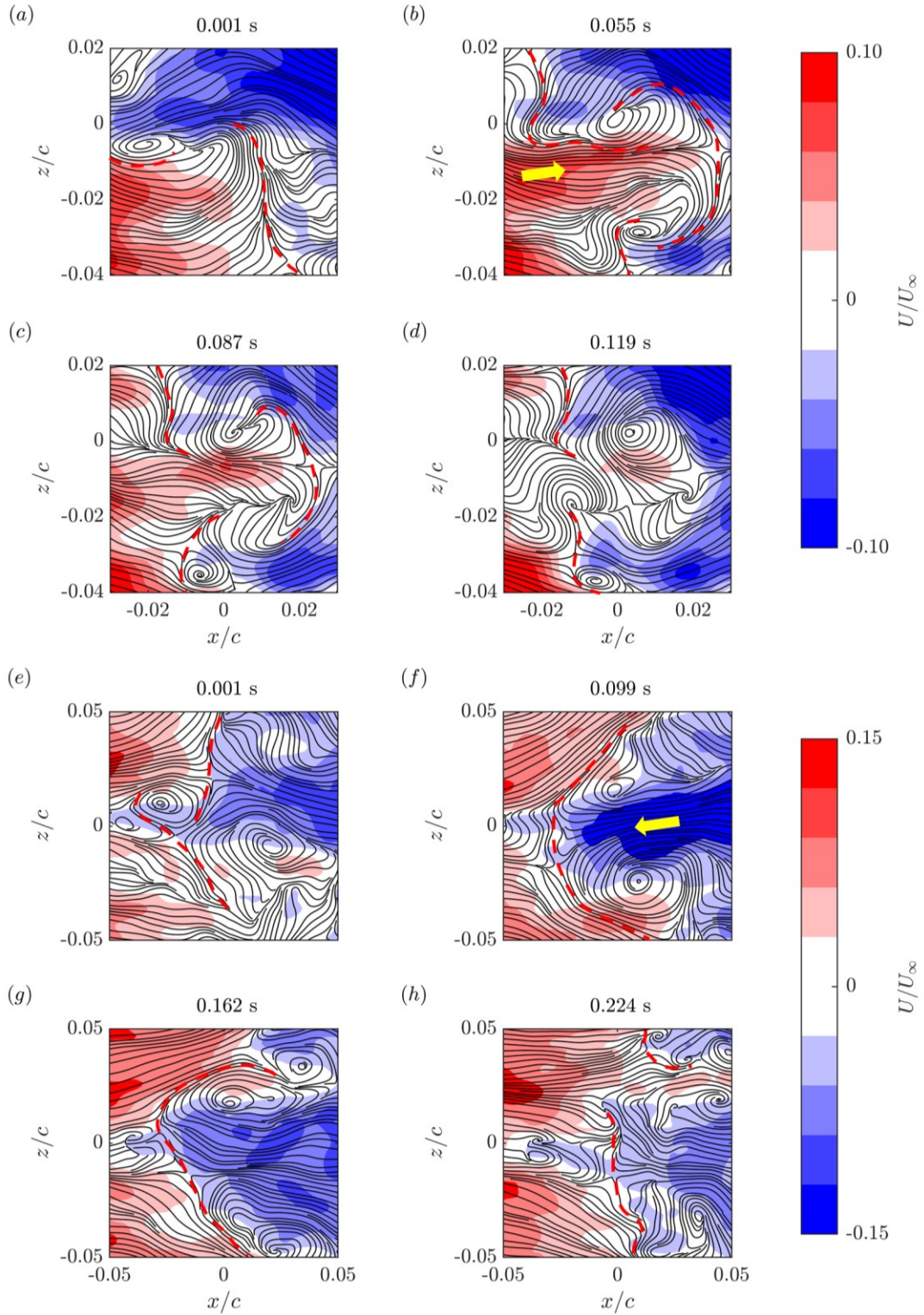


Figure 33. The formation and dissipation of (a – d) a forward stall cell and (e – h) a backward stall cell due to local concentrations of strong streamwise momentum. The colors in the background correspond to the normalized streamwise velocity.

4.2.4 High-Speed Streaks

In section 4.2.3, it was evident that foci are located at high-shear regions of forward or backward flow at the separation front. One possible scenario is that these high-shear regions are created by an inrush of streamwise momentum from upstream high-speed streaks of the turbulent boundary layer. If this is the case, then the width of instantaneous stall cells should be similar to the spanwise spacing between high-speed streaks. In this section, the spanwise distance between adjacent high-speed streaks (λ_z) in the upstream turbulent boundary layer is evaluated through spatial autocorrelation of the streamwise fluctuating velocity in the spanwise direction, which is then compared with the size of instantaneous stall cells determined previously. The normalized correlation coefficient, which is determined using

$$\rho(\Delta z) = \frac{\langle u(x_i, z, t_n) \cdot u(x_i, z + \Delta z, t_n) \rangle}{u_{rms}(x_i, z, t_n)^2}, \quad 4.1$$

can be a value between negative and positive one. The correlation curve is calculated for the n^{th} snapshot at a specified streamwise position x_i . At zero shift ($\Delta z = 0$), the signal aligns perfectly and return a value of $\rho = 1$. As the signal is shifted, the correlation coefficient decreases until a local minimum value is reached. At this minimum, the signal has been shifted by half the spanwise wavelength of the streamwise fluctuations and can therefore be used to determine the associated wavelength. The autocorrelation function was applied to the cyclic data set for faster statistical convergence. Histograms of the spanwise wavelengths have been generated and a lognormal distribution was used to model the probability density function (PDF) of the results.

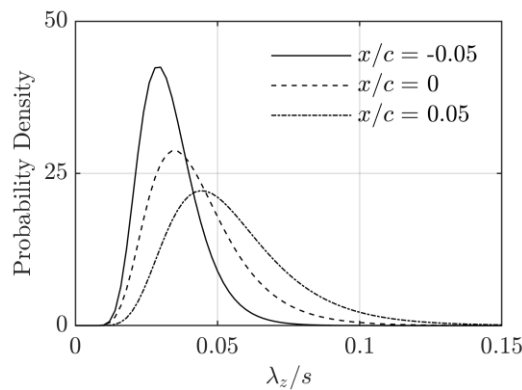


Figure 34. Probability density functions (PDFs) of the spanwise wavelength of high-speed streaks (λ_z/s) at three different chordwise positions. The wavelengths were determined by spatial autocorrelation of the fluctuating streamwise velocity using Eq. (4.1) and were fitted with a lognormal distribution.

The PDFs of the spanwise wavelengths are plotted for three different chordwise positions in Figure 34 to investigate the effect of chordwise position on streak width. The spanwise wavelengths of the streaks presented here are normalized by the span. The chordwise positions chosen correspond to an upstream location ($x/c = -0.05$), the mean separation point ($x/c = 0$), and a downstream location ($x/c = 0.05$). All three distributions are unimodal and are right-skewed to varying degrees. The upstream ($x/c = -0.05$) distribution features a peak located at $\lambda_z/s = 0.030$. In section 4.2.2, it was found that the width of instantaneous stall cells can range from approximately $0.02s$ to $0.06s$. The PDF corresponding to $x/c = -0.05$ reveals that a large majority of the upstream streak widths fall within this range. Consequently, the size of the instantaneous stall cells likely scales with the spacing between upstream high-speed streaks.

As the flow progresses downstream, the peak of the distribution moves to the right while the distribution broadens. At $x/c = 0$ and 0.05 , the peak is shifted to $\lambda_z/s = 0.034$ and 0.044 , respectively. Both of these peak locations (i.e. the most probable values) also fall within the aforementioned range of instantaneous stall cell sizes. The PDF at the downstream location ($x/c = 0.05$) is quite broad, indicating that the size of the streaks varies considerably post separation. This is quantified by the standard deviation of the distribution, which increases from 0.011 to 0.022 between $x/c = -0.05$ and 0.05 . The change in the PDFs reinforces the notion that streaks evolve into two foci and a saddle structure at separation. As the streaks vanish from the measurement plane, the spacing between the streaks increases and λ_z will tend towards a larger value.

The evolution of the high-speed streaks moving through the measurement plane is shown using three-dimensional isosurfaces in Figure 35(a). These isosurfaces have also been projected onto the $x-t$ axis in Figure 35(b) to highlight the advection of streaks in the streamwise direction. The streaks shown in the figure correspond to a segment of the unfiltered time-resolved data. There are a large number of high-speed streaks in the upstream region ($x/c < 0$) and a significant amount of the streaks subside before they reach the downstream section of the FOV. This agrees with the PDFs in Figure 34 and further supports the notion that streamwise momentum from high-speed streaks forms separation structures once they reach the separation front instead of persisting downstream.

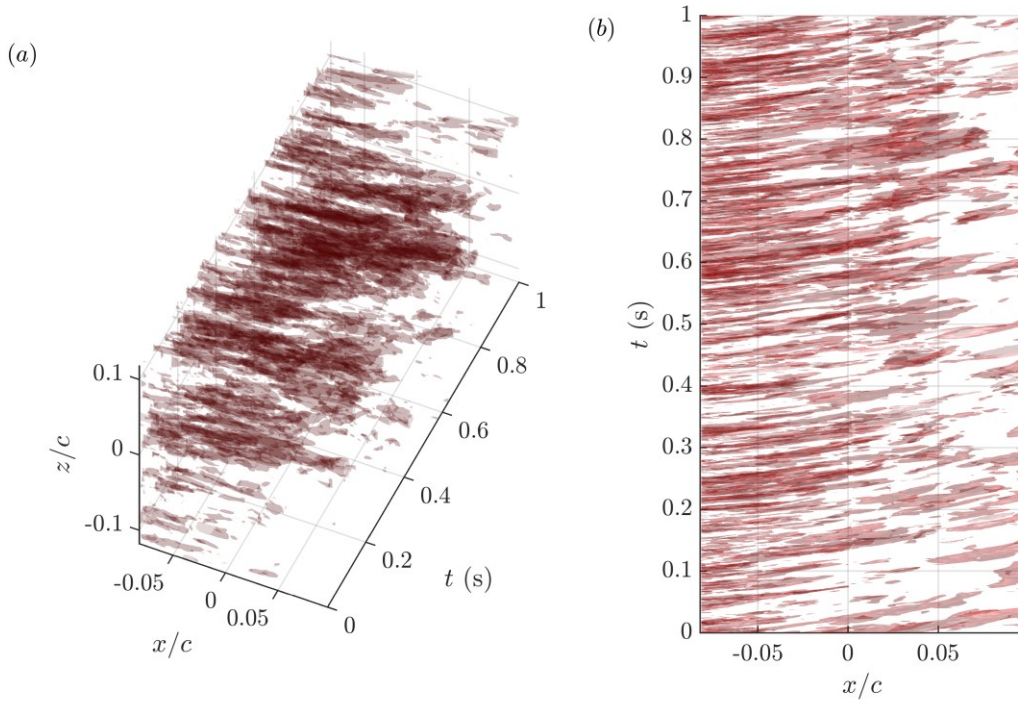


Figure 35. (a) Isosurfaces of the fluctuating streamwise velocity corresponding to $u/U_\infty = 0.12$. (b) The isosurfaces projected onto the x - t axis to highlight the advection velocity of streaks in the streamwise direction.

4.3 Energetic Motions

In this section, the energetic motions of the near-wall flow are investigated via POD of the cyclic datasets. The motion attributed to the energetic modes are determined by adding the spatial mode onto the mean velocity field and then analyzing the change.

POD by the method of snapshots (Sirovich 1987) was used to decompose the near-surface flow into a linear combination of optimal bases (POD modes). The instantaneous fluctuating velocity was used to obtain M spatial modes ($\vec{\phi}_m$), where M is the total number of snapshots used in the analysis. The modes are ordered based on energy content, with mode 1 containing the highest proportion of energy and mode M containing the least. The temporal amplitudes $a_m(t)$ represent the contribution of the corresponding mode m at time t . The data decomposition is mathematically represented by the equation

$$\vec{u}(x, z, t) = \sum_{m=1}^M a_m(t) \vec{\phi}_m(x, z). \quad 4.2$$

The arrow notation indicates a vector in the x - z plane.

The energy content of the first 100 modes is plotted on a semi-logarithmic axis in Figure 36. The first mode captures only 2.60% of the total turbulent kinetic energy content, and the first 100 modes account for 53.7% of the total energy. This is comparable to the results presented by Duquesne *et al.* (2015)(2015), who performed near-wall PIV at the separation front of a turbine diffuser. The amount of energy captured by the top 100 modes in their study ranged from 50% to 80% depending on the location of the measurement region. The low energy of the modes is due to presence of small-scale structures and a lack of coherent periodicity as was observed in the PSD.

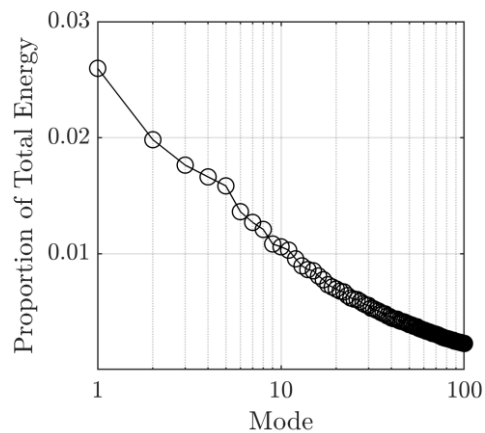


Figure 36. The energy content of the first 100 POD modes in the x - z plane of FOV2.

The first six POD modes are shown in Figure 37 and are arranged in descending order of energy content. The vectors in the figure represent the components of the normalized modes while the background contours show the streamwise component of the vectors. Vector arrows are not scaled identically between the subfigures, but the color map is consistent between them. Mode 1 is symmetric about mid-span. It contains a large streamwise fluctuation band with high shear around its border. The fluctuation can be positive or negative and can contribute to high- or low-speed instantaneous velocity, depending on the sign of the temporal coefficient $a_1(t)$. Modes 2 – 6 reveal similar alternating high- and low-speed streaks that decrease in size with decreasing energy. The streaky pattern of the modes is likely associated with large-scale distortion of the flow field, as the streaks are much larger than those observed in the upstream boundary layer.

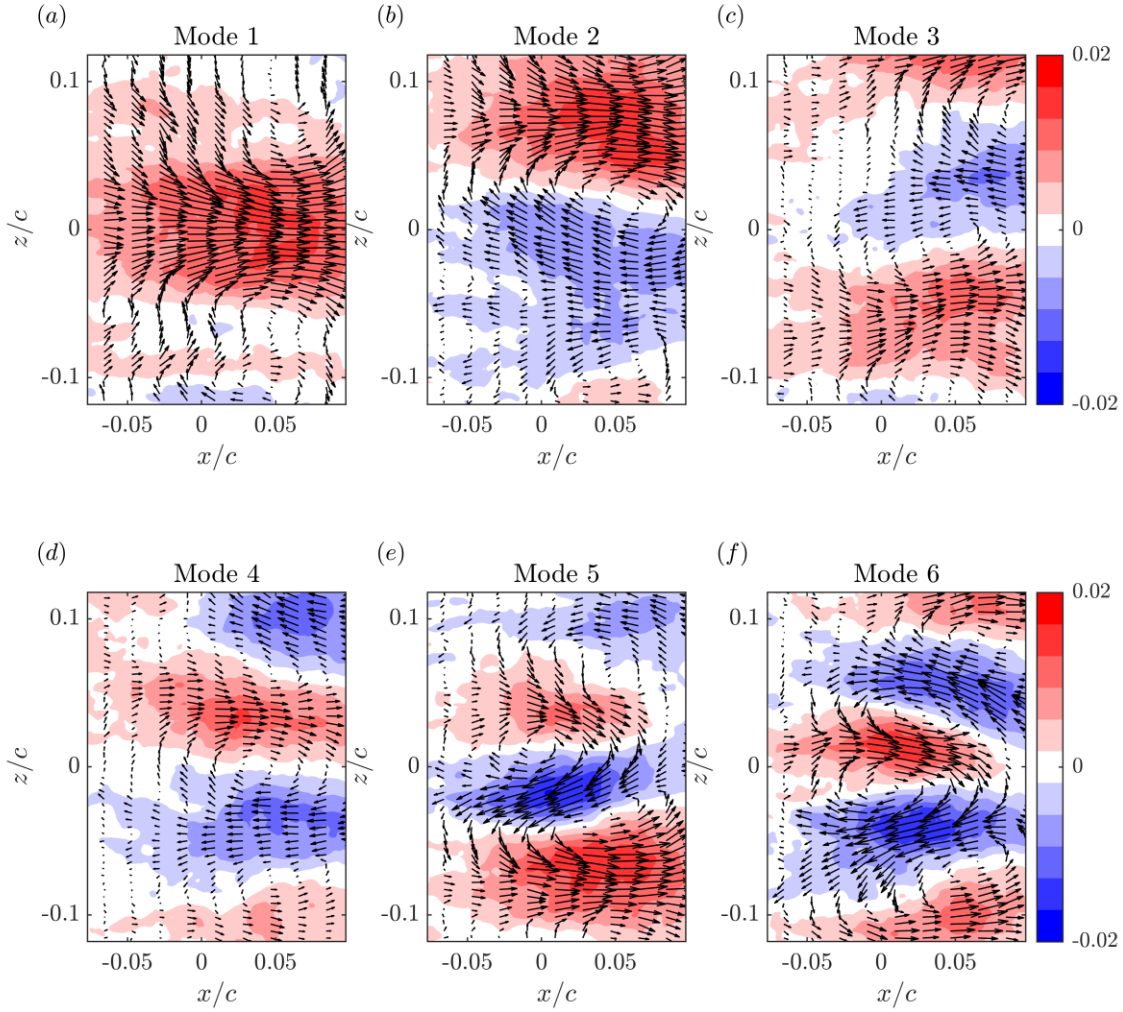


Figure 37. The first six POD modes obtained from decomposition of the fluctuating velocity field. Contours of the fluctuating streamwise velocity are shown in the background.

In order to investigate the effect of the first six modes, a reduced-order flow field was constructed by adding the respective mode to the mean velocity field, i.e. $\vec{U}_r = \langle \vec{U} \rangle + a_m \vec{\phi}_m$. The temporal coefficients were chosen based on the root mean square (RMS) value of the temporal coefficients associated with the respective mode, and both positive and negative coefficients were investigated. Temporal amplitudes of ± 25 were used for the investigation of the first spatial mode, and the results are presented in Figure 38(a). For the positive amplitude, the stall cell from the mean velocity field is eliminated from the flow pattern. The pair of counter rotating foci and the saddle point are no longer identifiable in the skin friction pattern, and the spanwise variation of the separation front is decreased. The stall cell becomes visible for the negative amplitude case,

which is shown in the lower subfigure of Figure 38(a); the saddle point and foci pair are easily identified here, and a strong backflow is observed near mid-span. The flow pattern is also symmetric with respect to mid-span. It is clear that mode 1 is related to the alternation between a two-dimensional separation front and a three-dimensional stall cell pattern, as well as the movement of the separation front in the streamwise direction.

Temporal amplitudes of ± 20 were used to construct the low-order flow field using modes 2 – 6 and the results are presented in Figure 38(b-f). Once again, these values are approximately equal to the associated RMS value of the coefficients within the ensemble. Mode 2 is responsible for shifting the stall cell toward the spanwise side of the airfoil, resulting in an asymmetric stall cell. A large positive amplitude moves the separation front farther downstream for $z/c > 0$ while bringing the separation front upstream for $z/c < 0$, effectively shifting the stall cell in the negative z -direction. A negative amplitude for the second mode has the opposite effect as it moves the stall cell in the positive z -direction. Mode 3 is similar to mode 2 in the sense that it is associated with distorting the stall cell in the spanwise direction. Mode 4 results in a smaller stall cell, shifted in one spanwise direction or the other based on the sign of the mode amplitude. Modes 5 and 6 act as a pair and they strongly control the spanwise distance between the counter-rotating foci. These results indicate that the distortion of the separation front and the movement of the two focus points can be identified as the most energetic motions of the turbulent flow within FOV2.

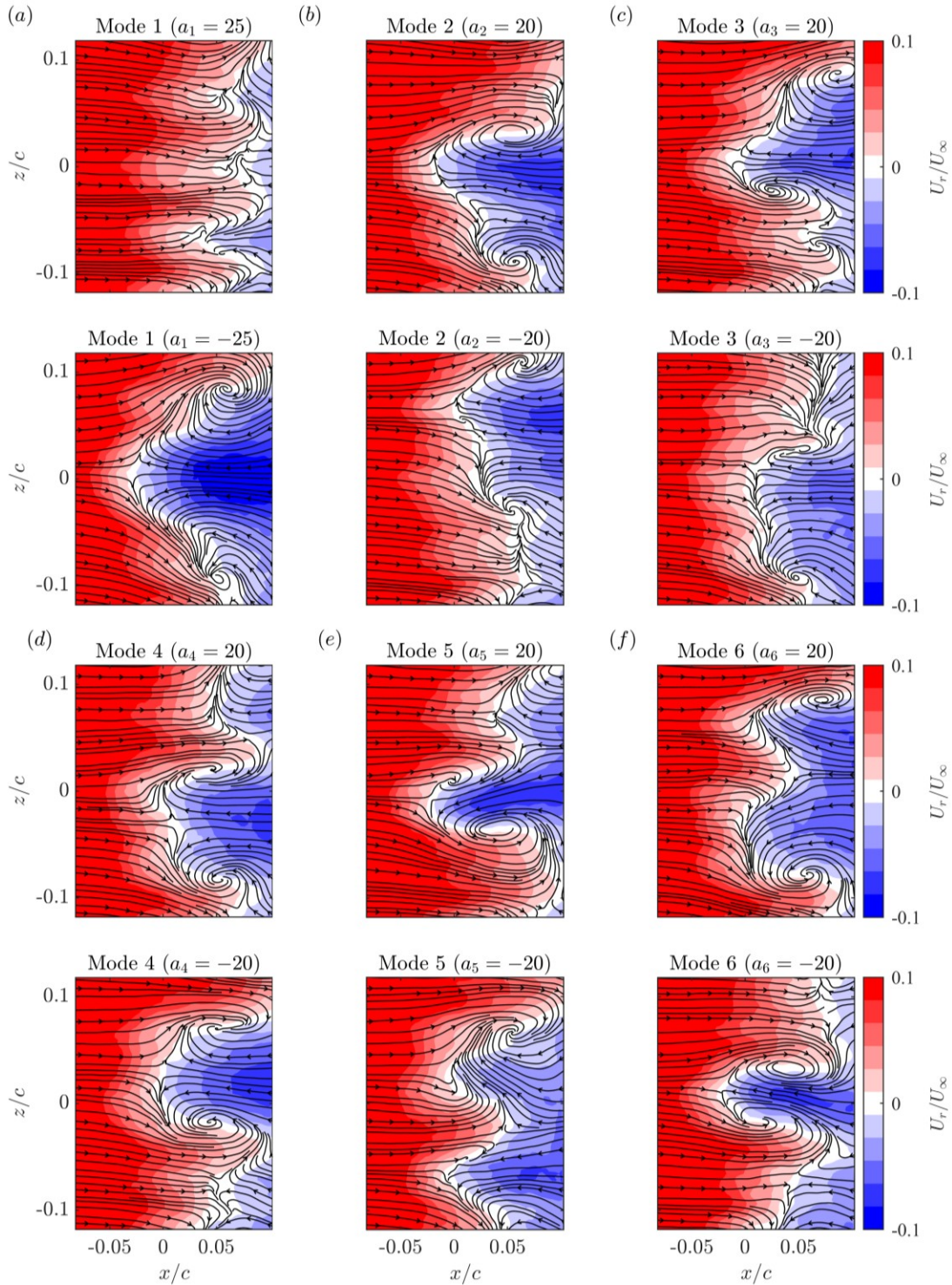


Figure 38. Low-order flow fields obtained by superimposing a selected spatial mode with the mean velocity field. The temporal amplitudes a_i are chosen based on the RMS value of the amplitudes associated with the respective mode. The background contours correspond to the normalized streamwise velocity.

4.4 Summary and Conclusions

In the present work, two-component PIV was used to study the unsteady organization of a three-dimensional trailing-edge separated flow over an airfoil at $Re_c = 750000$. The airfoil was at an angle of attack of 9° , which is located in the nonlinear pre-stall regime of the lift curve. Two FOVs were investigated: one located in a streamwise-wall-normal plane at mid-span and another located near and parallel to the airfoil surface at the separation location. The former experiment was used to characterize the turbulent boundary layer profile experiencing an APG, while the latter experiment was used to investigate the topology of the separated flow by analyzing the skin-friction patterns.

The velocity profiles, Reynolds stresses, and turbulence transport of the separated boundary layer flow in the streamwise-wall-normal plane at mid-span were similar to those reported by other studies of APG-induced flow separation. More specifically, the boundary layers in these flows experience a similar transformation leading up to separation, regardless of the source of the APG or whether the flow is two- or three-dimensional. Another commonality is that the location of peak stress moves away from the wall and broadens as the flow separates, resulting in two distinct regions whose turbulence transport mechanisms are dominated by either ejections or sweeps.

The mean skin-friction lines obtained from near-wall PIV revealed a saddle point near mid-span and two counter-rotating foci, each slightly downstream from the saddle point and offset in one spanwise direction or the other. The separation line emanating from the saddle point terminated at the two foci, resembling a stall cell pattern with a spanwise width of $0.17s$. The size of the mean stall cell found here is comparable with results from past investigations. Visualizations of instantaneous skin-friction lines revealed a highly unorganized flow field. Applying a temporal moving-average filter unveiled many saddle points and foci at the separation front. The existence of these separation structures along the separation front resulted in increased Reynolds stresses in this region. The instantaneous saddle points were more or less evenly distributed across the span. Clockwise foci were more densely concentrated towards one spanwise side of the airfoil, and counter-clockwise foci were more concentrated towards the other. The localization of small foci based on their direction of rotation is believed to be responsible for the stall cell pattern in the mean flow field.

The foci within the instantaneous skin-friction lines sometimes appeared in pairs, forming stall cell-like structures that are an order of magnitude smaller than the stall cell depicted in the mean pattern. However, the fact that clockwise and counter-clockwise foci tend to exist on one side of the airfoil or the other indicates that they do not always form in pairs. Instead of one distinct separation line across the span, the instantaneous separation front was made up of many local separation lines formed by the smaller stall cells. The “instantaneous stall cells” are associated with a strong local streamwise velocity fluctuation between the two foci. The orientation of the instantaneous stall cells depended on direction of the local flow situated between the foci pair. High-speed streaks from upstream penetrated the separation front to form an instantaneous stall cell with a saddle point on the downstream side of the foci pair, i.e. a “forward stall cell”. Conversely, strong backflow from the recirculation zone formed instantaneous stall cells with a saddle point on the upstream side of the foci pair – a “backward stall cell”. In both cases, the tornado-like foci pairs potentially carry the high-momentum fluid in wall-normal directions, causing the high-momentum fluid that formed the instantaneous stall cell to dissipate.

The formation of forward and backward stall cells was further scrutinized using PDFs of high-speed streak spacing as a function of streamwise distance. If streaks form the instantaneous stall cells, then the size of these stall cells should be comparable to the size of the streaks. This was indeed the case, as the PDFs revealed that the most probable distance between streaks of the same sign was within the range of instantaneous stall cell sizes. Moreover, the distance between streaks increased at streamwise locations further downstream, suggesting that streaks are disappearing as they move into the separation region. This is consistent with the hypothesis that foci pairs eject the high-momentum fluid away from the surface. This was further corroborated by visualizing the advection of high-speed streaks using isosurfaces. The visualization revealed that the concentration of streaky structures was greatly reduced within the separation region.

In agreement with previous studies of shallow stall, the unsteady flow field investigated here was found to be dominated by low-frequency motions ($St < 0.2$). These motions can be associated with the movement of the separation front, as it distorts along its span and undulates in the streamwise direction. Since the separation front is tied to the formation of critical points, these points have been tracked to get a sense of the movement and intermittency of the separation front. The streamwise and spanwise speeds of the critical points in the near-wall plane were roughly 1% of U_∞ . Their streamwise velocity was smaller but still positive, indicating that the critical points

can move both upstream and downstream with a slight tendency towards the downstream direction. The spanwise velocity was negligible, showing that the critical points generally do not exhibit preferential movement in one spanwise direction over the other.

Finally, the most energetic motions in the near-wall plane were investigated using POD. The first mode contained only 2.6% of the total fluctuation energy, and the first 100 modes captured a cumulative energy of 53.7%. This is indicative of the complexity of the flow field under investigation, as an accurate low-order representation of the data was not possible. Despite this, the first 6 modes were investigated in more detail by considering their individual contributions added to the mean flow field. It was shown that these 6 modes are responsible for distortion and movement of the mean separation front, namely switching between a two- and three-dimensional separation line, moving the mean stall cell in the spanwise directions, and changing the distance between the foci pair. The most energetic motions in the near-wall plane are therefore associated with the movement and distortion of the separation front.

Chapter 5. Active Control of Flow Separation using Piezoelectric Actuators

Methods of flow control are divided into passive and active techniques. Passive techniques involve a slight modification to the geometry of the flow device such as grooves, porous surfaces, and vortex generators. Active flow control is the suppression of flow separation using actuators such as synthetic fluidic jets/suction, vibrating surfaces, and plasma actuators. These devices are difficult to implement because they require additional electronic components such as a power source, amplifier, signal generator, and additional wiring. However, the main benefit of using active flow control over passive methods is they can be implemented in a closed-loop control system, allowing the system to optimize under changing conditions. In order to use piezoelectric actuators in a close-loop control system, it is necessary to first understand how various parameters, such as actuating frequency and actuator displacement, affect the flow topology.

It is widely reported that the motion of the oscillating piezoelectric actuators result in an increase in maximum lift coefficient while decreasing overall drag (Seifert *et al.* 1998; Zhang *et al.* 2008). These studies have typically been conducted with load cell measurements, which reveal no information on how the topology of a three-dimensional separation can change as result of the motion. In one study, Zhang *et al.* (2008) performed PIV on a streamwise-wall-normal plane on an airfoil with piezoelectric actuators. They theorized flow separation is suppressed by generation of large-scale spanwise vortices on the suction side of the airfoil, which increases the momentum of the flow within the boundary layer. Additional studies using PIV may be required to validate those claims.

The three-dimensional effects of a single piezoelectric actuator was investigated in the past with dye (Kim *et al.* 2013) and hot-wire measurements (Blackwelder *et al.* 1998). Kim *et al.* (2013) observed an organized pair of counter-rotating streamwise vortices at low oscillating frequencies. Increasing the perturbation frequency led to a highly unsteady and unorganized flow downstream of actuator. Likewise, Blackwelder *et al.* (2000) observed strong spanwise motion downstream of the actuators with a triangular tip. In these literatures, the impact of the oscillating motion on a separated shear layer was not demonstrated since the actuators were placed within a boundary layer without separation at low Reynolds number ($Re_x < 2 \times 10^5$). An array of oscillating

piezoelectric actuators across the span of an airfoil is required for suppressing separation, so the results from these studies may not be consistent under the context of suppressing separation at high Reynolds number.

The goal of experiment II is to investigate the impact of changing actuating frequency on the mean velocity fields, Reynold stresses, and frequency spectra in the in the near-wall region immediately downstream of the actuators. By changing the actuating frequency, the actuator displacement is also varied indirectly. As indicated in section 3.4.1, tests will be conducted for both two- and three-dimensional actuation mode.

5.1 Mean Velocity Flow Fields

The mean velocity field of the near-wall flow with the actuators at rest is shown in Figure 39 with the streamwise component displayed in the background contour. A three-dimensional separation is present in the flow, which is evident from the division of forward and backward flow along with large spanwise motion. There is a tendency of downward motion ($W < 0$) within the downstream region ($x/c \geq 0.1$). An undulated separation front presents itself in the mean flow field. At mid-span, the flow appears to detach immediately downstream of the actuators, i.e. $x/c = 0$. The flow field shown in Figure 39 is unsymmetrical even though the experimental setup is two-dimensional in nature. This is not uncommon for separated flow over two-dimensional airfoils as similar observations can be seen in oil flow visualization done by Dell'Orso & Amitay (2018) and tuft visualizations by Broeren & Bragg (2001). Even the stall cell structure shown in experiment I is not completely symmetric.

There is significant difference between the flow pattern shown here and the stall cell presented in experiment I. The mean flow pattern highlighted in section 4.1.3 reveals a pair of counter rotating foci but no such rotational structures can be observed in this case. One possible explanation for this is the imperfect mounting of the actuators and actuator flaps may have changed the topology of the separated flow. This include warping of the thin metal pieces, added tolerances of all of the pieces stacked on top of each other (e.g. multiple pieces of tape, actuator flaps, wire over, actuator), and existence of the gap between adjacent actuator flaps. For this reason, the performance of the actuators will be compared to flow field shown in Figure 39 instead of the results presented in experiment I.

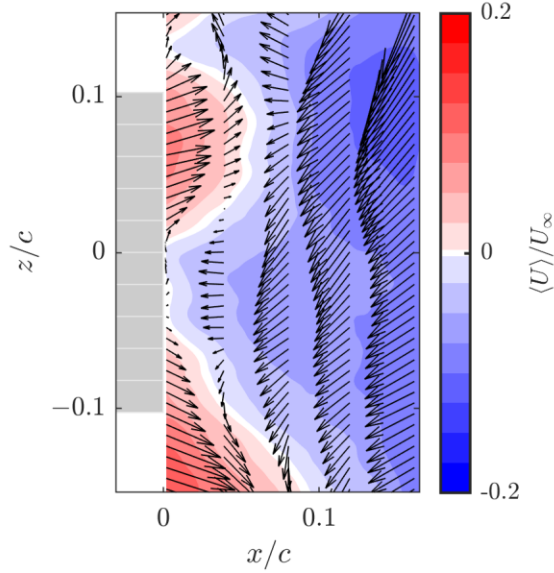


Figure 39. Mean velocity field of the near-wall flow with piezoelectric actuators at rest. The background contour correspond to the streamwise component of the near-wall velocity vectors.

The mean velocity field of the near-wall flow for actuating frequencies between $f_a = 50$ Hz to 225 Hz are shown in Figure 40 for the two-dimensional control mode and Figure 41 for the three-dimensional mode. The range of actuating frequencies correspond to a range of $St_a = 0.8 - 3.6$, where $St = f_a l_s / U_\infty$ as defined by Seifert et al. (1996). The characteristic length scale l_s is given as the length of the separated region, which is equivalent to 168 mm. The vectors shown in the figures are downsampled by a factor of 4 in the spanwise direction and only shown at $x/c = 0.01, 0.04, 0.08, 0.12, \text{ and } 0.16$ to improve visualization.

At first glance, the mean velocity field for all actuating frequencies are relatively similar. No obvious difference can be spotted between any of the mean velocity fields and the uncontrolled case (Figure 39). It is shown that the undulated outline of the separation front are similar for all actuating frequencies under the two-dimensional control mode; there are more backflow at the top of the field-of-view ($z/c > 0.10$) and the region just below mid-span ($-0.05 \leq z/c \leq 0$). This is true for all cases except at the highest tested actuating frequency $f_a = 225$ Hz. Under this configuration, the separation line is forced downstream near the mid-span region resulting in separation at around $x/c = 0.03$. This slight movement of the separation front in the downstream direction implies a decrease in size of the recirculation zone, which will result in a small increase in lift and decrease in drag. Zhang *et al.* (2008) reported only a 2 – 4% increase of the lift coefficient when flapping

actuators were excited with a sine wave in the post stall region. An increase that small would likely only result in a small change in the size of the recirculation zone like the results here show.

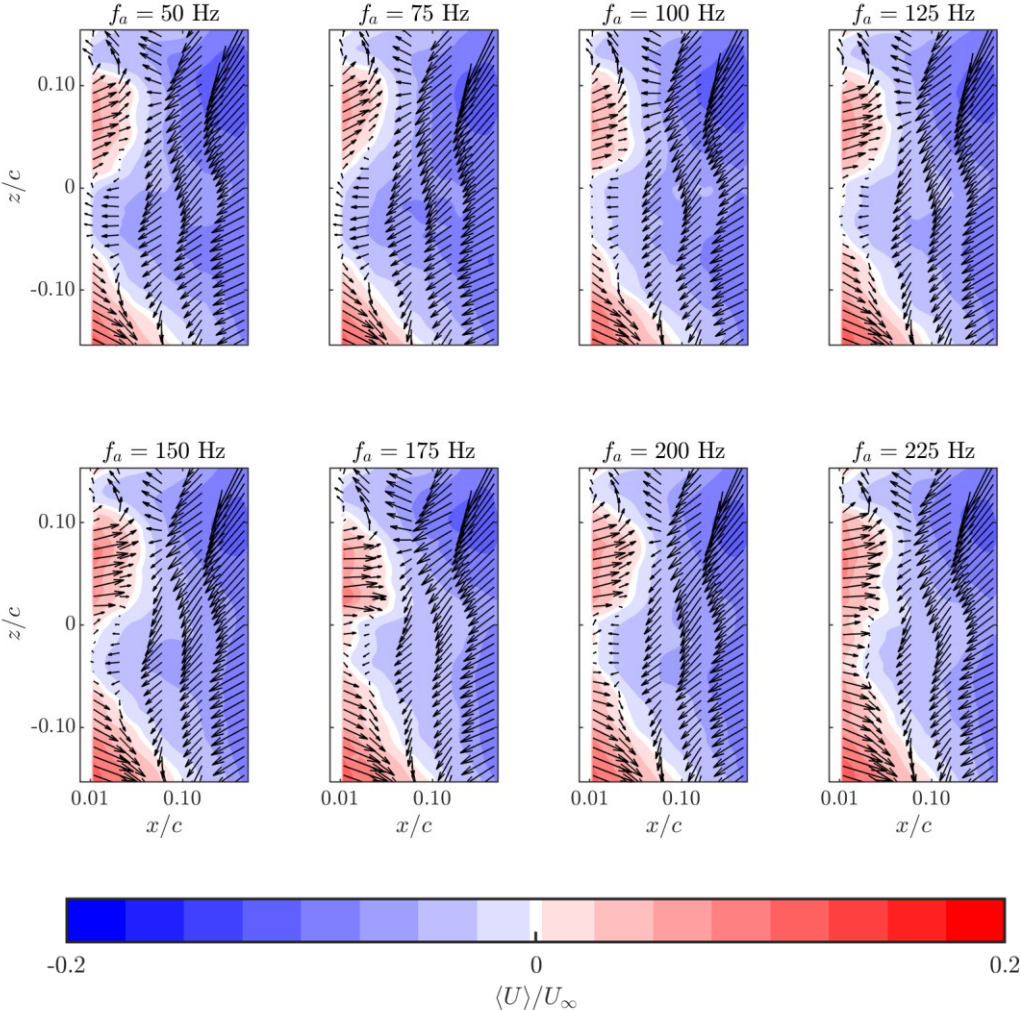


Figure 40. Mean velocity field of the near-wall flow with actuating frequencies between 50 and 225 Hz under the two-dimensional control mode. The background contour correspond to the streamwise component of the near-wall velocity vectors.

Similar conclusions can be made through examination of the mean velocity fields under a three-dimensional actuation in Figure 41. The average flow fields at different actuating frequencies are almost identical. Even at the highest actuating frequency, the actuators had no effect on the flow topology as the separation front remained close to $x/c = 0$ near mid-span. The three-dimensional actuating mode is less effective at flow control than the two-dimensional mode.

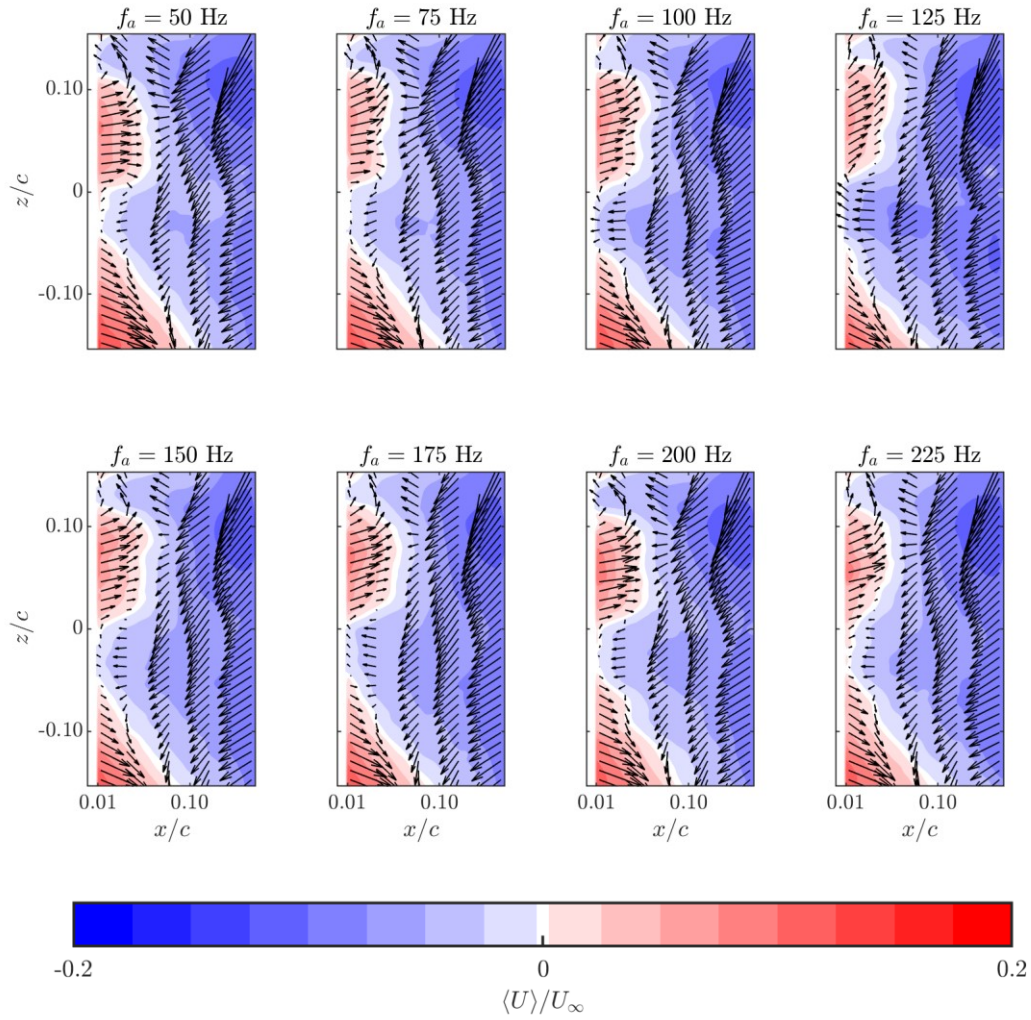


Figure 41. Mean velocity field of the near-wall flow with actuating frequencies between 50 and 225 Hz under the three-dimensional control mode. The background contour correspond to the streamwise component of the near-wall velocity vectors.

The outline of the separation line was estimated by finding the location of zero mean streamwise velocity ($\langle U \rangle = 0$) at every spanwise position. This will return the shape of the interface that divide the forward flow and backflow region. Note that this is only an estimation of the separation line since the separation line is identified by an asymptotic lines that intersect a saddle point in the skin-friction pattern. Since the generated curve is not the true separation line, the curves will be referred to as the backflow interface for correctness. Backflow interfaces for both the two-dimensional and three-dimensional mode are shown in Figure 42(a) and (b) respectively. The backflow interface at low actuation frequencies ($f_a \leq 125$ Hz) had parts of its outline extend upstream and outside of the field-of-view. As a result, these outlines were not shown in Figure 42.

The interface of the flow field with no actuation is shown by the red line. On the other hand, the colors of the other lines are shown in grayscale that increase in darkness with increasing actuating frequency.

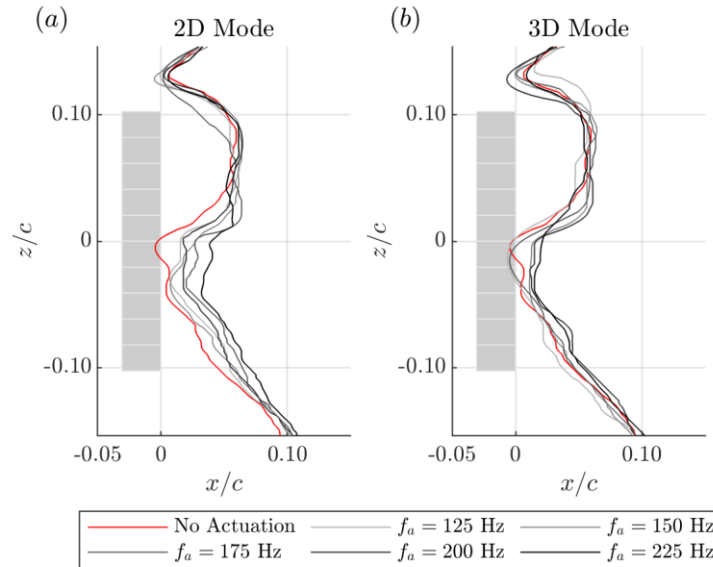


Figure 42. The backflow interface identified by points where $\langle U \rangle = 0$ for the (a) two-dimensional and (b) three-dimensional actuation mode. The location of the ten actuators are shown relative to the backflow interfaces.

Under the two dimensional-actuation mode, the backflow interface is pushed further downstream between $z/c = 0$ and -0.10 while minimal changes are observed between $y/c = 0.03$ and 0.10 . The actuators are most effective at locations where the backflow interface with no actuation lie immediately downstream. On the contrary, the actuators are less effective if the backflow interface with no flow control is far from where the energy is supplied. Figure 42(a) also show the distance shifted increases with increasing actuating frequency. This is surprisingly since the actuator displacement at 175 and 200 Hz are almost doubled the displacement at 225 Hz according to Figure 23. Since the actuator displacement is small to begin with – less than 1 mm at resonance – the added energy of actuating at a higher frequency provides a larger benefit for delaying separation. According to Seifert *et al.* (1996), flow control with oscillating flaps at a dimensionless frequency of $St_a = 1$. The present study does not show this, as operating the actuators at $f_a = 75$ Hz ($St_a = 1.2$) had almost no impact on the mean flow as shown in Figure 40 and Figure 41.

The actuators have almost no effect on the backflow interface when they operate under the three-dimensional mode. This is true across all actuation frequency, as the backflow interface remained almost identical in all cases. According to Seifert *et al.* (1998), the three-dimensional mode achieved similar performance to the two-dimensional mode with the benefit of requiring less power. However, the actuators used in their experiment had a maximum tip-to-tip displacement of 13 mm, which is much larger than the displacement of the actuators used in the present experiment. At small actuator displacement, the two-dimensional mode should be used for flow control.

5.2 Reynold stresses

The Reynolds stresses for the near wall flow with no actuation and actuating at $f_a = 225$ Hz are shown in Figure 43 below. Reynolds stresses of all the other configurations of flow control can be seen in Appendix A. The Reynolds normal and shear stresses in Figure 43 reveal no distinguishable trend between the flow with no actuation, two-dimensional actuation at 225 Hz, and three-dimensional actuation at 225 Hz. At the same time, the magnitude of Reynolds stresses between no actuation and all cases of flow control are similar. The oscillation of the actuators have minimal impact on the turbulence statistics, meaning the energy supplied to the flow by the actuators are smaller than the turbulence energy of the flow. This is possibly due to the small tip displacement. This observation is consistent among the Reynolds stresses for all other actuating frequencies for both the two-dimensional and three-dimensional case, as shown in the figures in Appendix A1-A6. In a similar study performed by Zhang *et al.* (2008), the authors saw almost no change in the instantaneous streamwise flow velocity when the actuators were excited with a sine wave signal. The fact that there are no distinct differences between the Reynolds stresses here is not surprising.

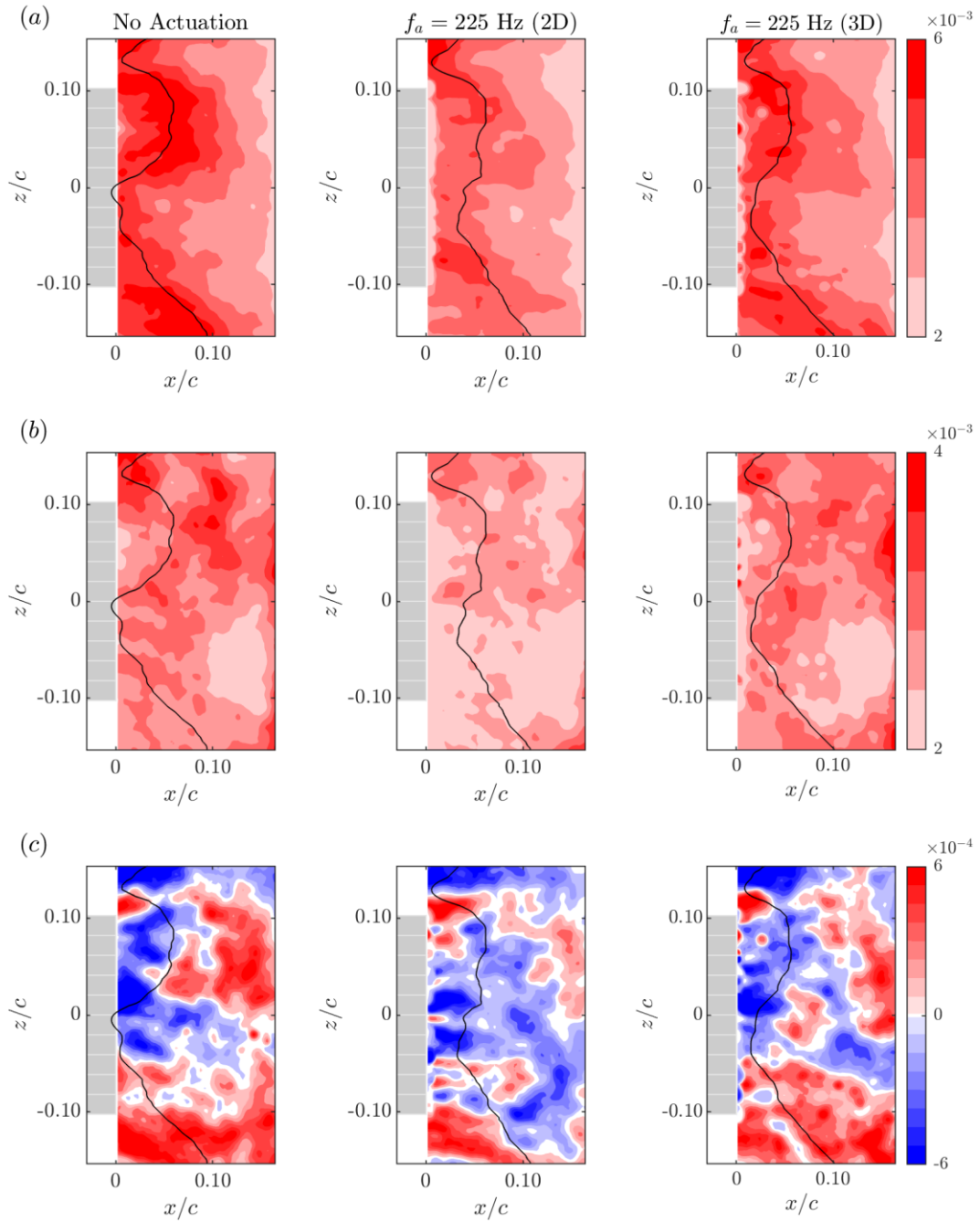


Figure 43. (a) Streamwise Reynolds normal stresses ($\langle u^2 \rangle$), (b) spanwise Reynolds normal stresses ($\langle w^2 \rangle$), and (c) Reynolds shear stresses ($\langle uw \rangle$) for the no actuation case, two-dimensional actuation at 225 Hz, and three-dimensional actuation at 225 Hz.

5.3 Spectral Analysis

The power spectral density (PSD) of the fluctuating streamwise velocity, u , at various points along midspan were evaluated for both the two- and three-dimensional case at 225 Hz. The results are presented in Figure 44 and no distinct peak are shown in any of the PSD. Power spectral densities of the fluctuating streamwise velocity were also evaluated under different control cases and for different locations within the field of view. These figures are shown in appendix A and they are near identical to the PSDs in Figure 44. The fluctuation of the streamwise velocity caused by oscillation of the actuators may be undetected in the PSDs because the length scale of the generated eddies are smaller than the offset of the laser sheet from the wall, which is 2 mm. As a result, it is likely that the generated eddies did not pass through the measurement region.

Power spectral densities were evaluated for the backflow ratio, Γ , defined as the percentage of flow within the field of view that is backwards (i.e. $U < 0$). This was done to see if the actuators had an impact on the size of the recirculation zone even though the generated eddies did not pass through the field of view. From the results shown in Figure 45, the actuating frequency of 225 Hz can easily be identified by the peak in the spectrum for both the two- and three-dimensional case. The analysis was repeated for all actuating frequencies and the peak was only observed at actuating frequencies of 200 and 225 Hz and not for low frequencies. Spectral analysis showed that with sufficient energy, i.e. high frequency, the actuators can have an oscillating effect on the amount of downstream flow within the field of view.

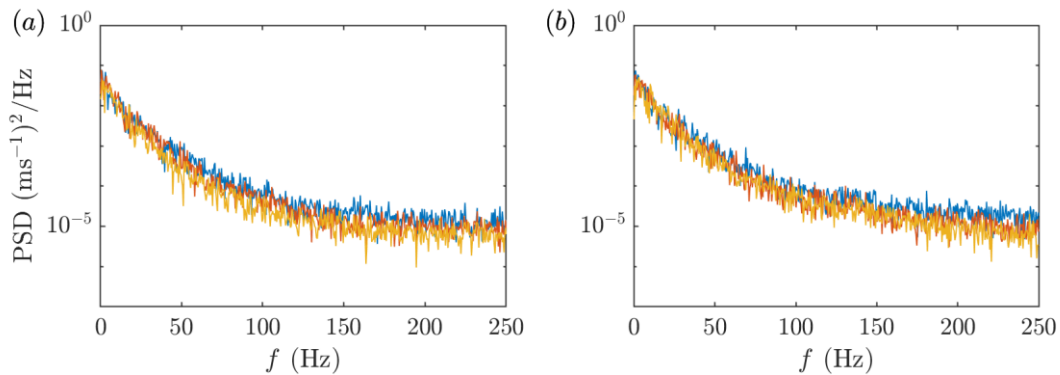


Figure 44. Power spectral density of the fluctuating streamwise velocity, u , for the (a) two-dimensional and (b) three-dimensional actuation mode at 225 Hz. The PSDs are obtained from points $x/c = 0.01, 0.05, 0.10, \text{ and } 0.15$ at $z/c = 0$ (midspan).

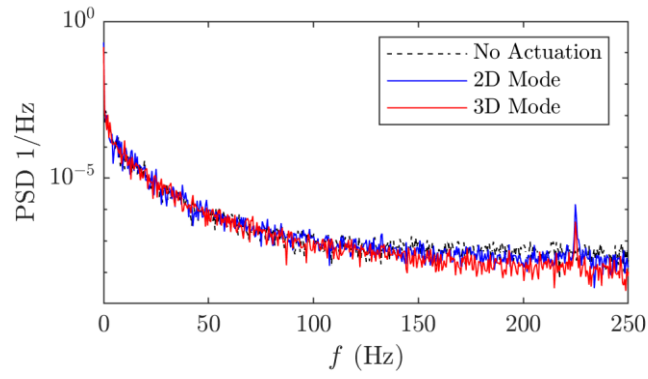


Figure 45. Power spectral density of the backflow ratio (I) for the separated flow with no flow control and two- and three-dimensional actuation at 225 Hz.

5.4 Conclusions

There were negligible differences between the mean velocity fields of varying actuating frequencies for the three-dimensional actuation mode: the backflow interface retained its shape and remained at approximately the same position compared with the flow with no actuation. Under the two dimensional actuation mode, the backflow interface advanced downstream with increasing perturbation frequency. A downstream movement of the separation front implies a decrease in size of the recirculation region, leading to higher lift and less drag.

The actuators were more effective at “pushing” the separation front downstream for section of the span where the natural separation line is immediately downstream of the actuators. This is consistent with the conclusion made by Seifert *et al.* (1996) and it remains true regardless if a mechanical device, i.e. piezoelectric actuators, or a fluidic jet/suction. At the highest frequency of $f_a = 225$ Hz ($St = 3.6$), the backflow interface was shifted $0.04c$ downstream near midspan where the separation occurs closest to the actuators. This can be problematic if one wanted to design a flow control system using piezoelectric actuators for an airfoil, because separated flow typically exhibit a three-dimensional topology even with a two-dimensional setup (Gregory *et al.* 1971; Moss & Murdin 1970; Winkelmann & Barlow 1980) and the separation location can change under different flight conditions such as speed and angle of attack (McCullough & Gault 1951).

Chapter 6. Conclusion

6.1 Summary

The separated turbulent boundary layer from the trailing edge of a NACA 4418 airfoil within the nonlinear pre-stall region was characterized. Within a streamwise-wall-normal plane along the midspan of the airfoil, the boundary layer profile, Reynold stresses, and turbulence transport were consistent with previous studies of separated flow with different flow topologies. The agreement suggests the roll-up of the shear layer is a major contributor to the turbulence statistics within the streamwise-wall-normal plane. Near-wall PIV was performed to obtain an approximation of the skin-friction pattern. The streamlines of the mean flow revealed a separation saddle point near midspan with the ends of the separation line terminating at a pair of counter-rotating foci. Previous literature termed this distinctive separation pattern over an airfoil as a stall cell. Inspection of the time-resolved instantaneous streamlines showed organized structures resembling smaller stall cells within the separation front. Further inspection showed that these instantaneous structures were formed by streaks of strong downstream or backflow. By isolating the motion of high-speed streaks from the upstream flow, it was shown that the streaks vanish from the measurement region as they approach the separation front. From this observation, it was hypothesized that the momentum of the high-speed streaks from the upstream flow are converted into a rotational motion at the separation front.

In the latter part of the project, an array of piezoelectric actuators were mounted flush to the surface of the airfoil upstream of the saddle point. Placement of the actuators caused the flow topology to change: the stall cell pattern was removed but three-dimensional separation was still present. For sections of the span where the natural, i.e. without flow control, separation line is closest to the actuators, the separation front was “pushed” downstream, effectively reducing the size of the recirculation zone. This effect was amplified with increasing actuating frequency. No significant differences were observed in the flow when adjacent actuators operated 180° out-of-phase. Periodic motion of the actuator accelerates the generation of large coherent structures (Seifert *et al.* 1996). These structures may possibly contain large streamwise momentum that contribute in the formation of instantaneous stall cells and downstream movement of the separation

front. This study implies there is a difference in the large coherent structure generated by the two- and three-dimensional actuating mode that make the former more effective at delaying separation.

6.2 Future Works

It was hypothesized, from experiment I, that the momentum of high-speed streaks are converted into rotational motion at the separation front instead of persisting downstream into the backflow region. Time-resolved three-dimensional measurements of the flow at the separation front can be conducted to verify this motion. The experiment should also be repeated for an airfoil with aspect ratio larger than 1.2 that may feature a different flow topology to determine whether the motion is universal. The average velocity field at the near-wall plane revealed attached flow for approximately 60% of the field of view. Considering the large spatial influence of the separation, a PIV experiment that captures more of the attached flow would be useful for verifying the source of the streaks.

It was recognized that there were shortcomings in the design of the experiment that led to null results for experiment II. The implementation of piezoelectric actuators were expected to suppress a mild trailing-edge separation, of which the effects can be observed in the near-wall topology. It is believed that the main reason for this is that the maximum displacement of the actuators used, which ranged from 0.4 mm to 0.8 mm, were too small to have a significant impact on the flow. Using the results obtained from experiment I, the ratio of the maximum actuator displacement to the boundary layer thickness at the mean separation point ($d_{a,max}/\delta_{99}$) is 0.018. Because the actuators were attached to the surface of the airfoil with two-sided tape, the resting height of the actuators was also inconsistent. At rest, the tip of the actuator flaps were within a range of 0.5 mm relative to each other. This proved to be problematic since it is the same magnitude as the actuator displacement. At the same time, these minor steps may also have passive effect on the separated flow. The actuators also tended to shift and move out of position after running. As a result, they needed to be pushed back into place between tests. For future experiments, all ten actuators can be attached to one large flap instead of bonding each actuator to an individual flap since the two-dimensional mode is more effective for flow control.

According to the results in Seifert *et al.* (1998), the actuators have minimal effect in the pre-stall separated region – the narrow range of angles of attack where separation had occurred but maximum lift has not been achieved yet. The largest change in lift occurs at angles of attack well

beyond stall, i.e. larger separation. For this reason, it may be more suitable to investigate the flow control of piezoelectric actuators at higher angles of attack where the separation occurs further upstream. In previous experiments, actuators and jets were usually placed immediately upstream of the separated shear layer. However, it may be more beneficial to investigate whether placing actuators within the recirculation zone promotes flow reattachment because the separation point is sensitive to many parameters.

REFERENCES

- Abbott, I. H., & Von Doenhoff, A. E. (1959). *Theory of wing sections, including a summary of airfoil data*, Courier Corporation.
- Adrian, R., & Westerweel, J. (2011). *Particle image velocimetry*, Cambridge University Press.
- Alving, A. E., & Fernholz, H. H. (1996). Turbulence measurements around a mild separation bubble and downstream of reattachment. *Journal of Fluid Mechanics*, **322**, 297–328.
- Angele, K. P., & Muhammad-Klingmann, B. (2006). PIV measurements in a weakly separating and reattaching turbulent boundary layer. *European Journal of Mechanics-B/Fluids*, **25**(2), 204–222.
- Blackwelder, R. F., Liu, D., & Jeon, W. (1998). Velocity perturbations produced by oscillating delta wing actuators in the wall region. *Experimental Thermal and Fluid Science*, **16**(1–2), 32–40.
- Broeren, A. P., & Bragg, M. B. (2001). Spanwise Variation in the Unsteady Stalling Flow fields. *AIAA Journal*, **39**(9), 1641–1651.
- Brossard, C., Monnier, J. C., Barricau, P., Vandernoot, F. X., Le Sant, Y., Champagnat, F., & Le Besnerais, G. (2009). Principles and applications of particle image velocimetry. *AerospaceLab*, 1–11.
- Castillo, L., Wang, X., & George, W. K. (2004). Separation criterion for turbulent boundary layers via similarity analysis. *Journal of Fluids Engineering*, **126**(3), 297–304.
- Cattafesta, L. N., & Sheplak, M. (2011). Actuators for Active Flow Control. *Annual Review of Fluid Mechanics*, **43**(1), 247–272.
- Choi, J., Jeon, W.-P., & Choi, H. (2002). Control of flow around an airfoil using piezoceramic actuators. *AIAA Journal*, **40**(5), 1008–1010.
- Coles, D., & Wadcock, A. (1978). Flying-hot-wire study of two-dimensional mean flow past an NACA 4412 airfoil at maximum lift. In *11th Fluid and Plasma Dynamics Conference*, p. 1196.
- Corke, T. C., Enloe, C. L., & Wilkinson, S. P. (2010). Dielectric Barrier Discharge Plasma Actuators for Flow Control. *Annual Review of Fluid Mechanics*, **42**(1), 505–529.
- Délery, J. (2013). *Three-dimensional separated flow topology: critical points, separation lines and vortical structures*, John Wiley & Sons.
- Dell’Orso, H., & Amitay, M. (2018). Parametric investigation of stall cell formation on a NACA 0015 airfoil. *AIAA Journal*, **56**(8), 3216–3228.
- Dengel, P., & Fernholz, H. H. (1990). An experimental investigation of an incompressible turbulent boundary layer in the vicinity of separation. *Journal of Fluid Mechanics*, **212**, 615–636.
- Depardon, S., Lasserre, J. J., Boueilh, J. C., Brizzi, L. E., & Borée, J. (2005). Skin friction

- pattern analysis using near-wall PIV. *Experiments in Fluids*, **39**(5), 805–818.
- Duquesne, P., Maciel, Y., & Deschênes, C. (2015). Unsteady flow separation in a turbine diffuser. *Experiments in Fluids*, **56**(8), 156.
- Elyasi, M., & Ghaemi, S. (2019). Experimental investigation of coherent structures of a three-dimensional separated turbulent boundary layer. *Journal of Fluid Mechanics*, **859**, 1–32.
- Fish, F., & Lauder, G. (2006). Passive and Active Flow Control by Swimming Fishes and Mammals. *The Annual Review of Fluid Mechanics*, 193–224.
- Ghaemi, S., Ragni, D., & Scarano, F. (2012). PIV-based pressure fluctuations in the turbulent boundary layer. *Experiments in Fluids*, **53**(6), 1823–1840.
- Gibeau, B., & Ghaemi, S. (2020). The mode B structure of streamwise vortices in the wake of a two-dimensional blunt trailing edge. *Journal of Fluid Mechanics*, 884.
- Gregory, J. W., Ruotolo, J. C., Byerley, A. R., & McLaughlin, T. E. (2007). Switching behavior of a plasma-fluidic actuator. *Collection of Technical Papers - 45th AIAA Aerospace Sciences Meeting*, **14**, 9619–9629.
- Gregory, N., Quincey, V. G., O'Reilly, C. L., & Hall, D. J. (1971). Progress Report on Observations of Three-Dimensional Flow Patterns obtained during Stall Development on Aerofoils, and on the Problem of Measuring Two-Dimensional Characteristics. *Aeronautical Research Council: Current Papers*, (1146).
- Heinzel, G., Rüdiger, A., & Schilling, R. (2002). Spectrum and spectral density estimation by the Discrete Fourier transform (DFT). *MPG Publication Repository*, 1–84.
- Holm, R., & Gustavsson, J. (1999). A PIV study of separated flow around a 2D airfoil at high angles of attack in a low speed wind tunnel. *FFA TN*, **52**.
- Jeon, W. P., & Blackwelder, R. F. (2000). Perturbations in the wall region using flush mounted piezoceramic actuators. *Experiments in Fluids*, **28**(6), 485–496.
- Jeong, J., & Hussain, F. (1995). On the Identification Problem. *Journal of Fluid Mechanics*, **285**(1), 69–94.
- Jones, L. E., Sandberg, R. D., & Sandham, N. D. (2008). Direct numerical simulations of forced and unforced separation bubbles on an airfoil at incidence. *Journal of Fluid Mechanics*, **602**, 175–207.
- Kähler, C. J., Scharnowski, S., & Cierpka, C. (2012). On the resolution limit of digital particle image velocimetry. *Experiments in Fluids*, **52**(6), 1629–1639.
- Kim, D.-H., Chang, J.-W., & Cho, J.-S. (2013). Flow disturbances depending on excitation frequency on a flat plate by a piezoceramic actuator. *Journal of Visualization*, **16**(2), 111–121.
- Lighthill, M. (1963). Section 2.6. Attachment and Separation in Three-Dimensional Flows. *Laminar Boundary Layers*, Oxford University Press.
- Lin, J., Howard, F., & Selby, G. (1989). Turbulent flow separation control through passive

- techniques. *2nd Shear Flow Conference*.
- Liu, T., Woodiga, S., & Ma, T. (2011). Skin friction topology in a region enclosed by penetrable boundary. *Experiments in Fluids*, **51**(6), 1549–1562.
- Lu, F. K. (2010). Surface oil flow visualization. *European Physical Journal: Special Topics*, **182**(1), 51–63.
- Luchtenburg, D. M., Noack, B. R., & Schlegel, M. (2009). An introduction to the POD Galerkin method for fluid flows with analytical examples and MATLAB source codes. *Berlin Institute of Technology MBI, Muller-Breslau-Strabe*, **11**.
- Manolesos, M., Papadakis, G., & Voutsinas, S. G. (2014). Experimental and computational analysis of stall cells on rectangular wings. *Wind Energy*, **17**(6), 939–955.
- Manolesos, M., & Voutsinas, S. G. (2014a). Geometrical characterization of stall cells on rectangular wings. *Wind Energy*, **17**(9), 1301–1314.
- Manolesos, M., & Voutsinas, S. G. (2014b). Study of a stall cell using stereo particle image velocimetry. *Physics of Fluids*, **26**(4). doi:10.1063/1.4869726
- McCullough, G., & Gault, D. (1951). Examples of three representative types of airfoil-section stall at low speed. *NACA Technical Note 2502*.
- Meinhart, C. D., Wereley, S. T., & Santiago, J. G. (2000). A PIV algorithm for estimating time-averaged velocity fields. *Journal of Fluids Engineering*, **122**(2), 285–289.
- Melling, A. (1997). Tracer particles and seeding for particle image velocimetry. *Measurement Science and Technology*, **8**(12), 1406–1416.
- Michaelis, D., Neal, D., & Wieneke, B. (2016). Peak-locking reduction for particle image velocimetry. *Measurement Science and Technology*, **27**(10).
- Moghaddam, T., & Neishabouri, N. B. (2017). On the Active and Passive Flow Separation Control Techniques over Airfoils. *IOP Conference Series: Materials Science and Engineering*, **248**(1). doi:10.1088/1757-899X/248/1/012009
- Moss, G. F., & Murdin, P. M. (1970). Two-dimensional low-speed tunnel tests on the NACA 0012 1008 section including measurements made during pitching oscillations at the stall. *HM Stationery Office: Aeronautical Research Council CP. No. 1145*.
- Na, Y., & Moin, P. (1998). Direct numerical simulation of a separated turbulent boundary layer. *Journal of Fluid Mechanics*, **374**, 379–405.
- Poincare, H. (1928). *Oeuvres complètes de Henri Poincare*, Paris: Gauthier-Villars.
- Raffel, M., Willert, C., Scarano, F., Kähler, C., Wereley, S., & Kompenhans, J. (2018). *Particle Image Velocimetry - A Practical Guide*, Springer.
- Ragni, D., & Ferreira, C. (2016). Effect of 3D stall-cells on the pressure distribution of a laminar NACA64-418 wing. *Experiments in Fluids*, **57**(8), 1–19.
- Scarano, F., & Riethmuller, M. L. (1999). Iterative multigrid approach in PIV image processing with discrete window offset. *Experiments in Fluids*, **26**(6), 513–523.

- Schlichting, H., & Gersten, K. (2016). *Boundary-Layer Theory*, Springer.
- Schubauer, G., & Spangenberg, W. (1960). Forced mixing in boundary layers. *Journal of Fluid Mechanics*, 10–32.
- Seifert, A., Darabi, A., & Wygnanski, I. (1996). Delay of airfoil stall by periodic excitation. *Journal of Aircraft*, **33**(4), 691–698.
- Seifert, A., Eliahu, S., Greenblatt, D., & Wygnanski, I. (1998). Use of piezoelectric actuators for airfoil separation control. *AIAA Journal*, **36**(8), 1535–1537.
- Seiler, M., & Seiler, F. (1989). Numerical recipes in C: the art of scientific computing. In *Numerical recipes in C: the art of scientific computing*, Wiley, pp. 549–558.
- Simpson, R. L. (1981). A review of some phenomena in turbulent flow separation. *Journal of Fluids Engineering, Transactions of the ASME*, **103**(4), 520–533.
- Simpson, R. L. (1989). Turbulent boundary-layer separation. *Annual Review of Fluid Mechanics*, **21**(1), 205–232.
- Sirovich, L. (1987). Turbulence and the dynamics of coherent structures Part I: Coherent Structures. *Quarterly of Applied Mathematics*, **45**(3), 561–571.
- Song, S., & Eaton, J. (2002). The effects of wall roughness on the separated flow over a smoothly contoured ramp. *Experiments in Fluids*, **33**(1), 38–46.
- Surana, A., Grunberg, O., & Haller, G. (2006). *Exact theory of three-dimensional flow separation. Part I. Steady separation*. *Journal of Fluid Mechanics*, Vol. 564. doi:10.1017/S0022112006001200
- Thompson, B. E., & Whitelaw, J. H. (1985). Characteristics of a trailing-edge flow with turbulent boundary-layer separation. *Journal of Fluid Mechanics*, **157**, 305–326.
- Thompson, B., & Whitelaw, J. (1982). A turbulent boundary layer approaching separation. In *Recent Contributions to Fluid Mechanics*, 253–264.
- Tobak, M., & Peake, D. J. (1982). Topology of Three - Flows. *Annual Review of Fluid Mechanics*, **14**, 61–85.
- Visbal, M. R. (1991). Structure of Laminar Juncture Flows. *AIAA Journal*, **29**(8), 1273–1282.
- Wadcock, A. J. (1987). *Investigation of Low-Speed Turbulent Separated Flow Around Airfoils (Analytical Methods)*.
- Wang, K. (1972). Separation patterns of boundary layer over an inclined body of revolution. *AIAA Journal*, 1044–1050.
- Wang, S., & Ghaemi, S. (2019). Three-dimensional wake of nonconventional vortex generators. *AIAA Journal*, **57**(3), 949–961.
- Weih, D., & Katz, J. (1983). Cellular patterns in poststall flow over unswept wings. *AIAA Journal*, 1757–1759.
- Westerweel, J., & Scarano, F. (2005). Universal outlier detection for PIV data. *Experiments in*

Fluids, **39**(6), 1096–1100.

Winkelmann, A., & Barlow, J. (1980). Flowfield model for a rectangular planform wing beyond stall. *AIAA Journal*, **18.8**, 1006–1008.

Yon, S., & Katz, J. (1998). Study of the unsteady flow features on a stalled wing. *AIAA Journal*, **36.3**, 305–312.

Zaman, K. B. M. Q., McKinzie, D. J., & Rumsey, C. L. (1989). *A Natural Low-Frequency Oscillation of the Flow over an Airfoil Near Stalling Conditions*. *Journal of Fluid Mechanics*, Vol. 202. doi:10.1017/S0022112089001230

Zhang, H., Younis, M., Hu, B., Wang, H., & Wang, X. (2012). Investigation of attachment saddle point structure of 3-D steady separation in laminar juncture flow using PIV. *Journal of Visualization*, **15.3**, 241–252.

Zhang, M. M., Zhou, Y., & Cheng, L. (2008). Control of poststall airfoil aerodynamics based on surface perturbation. *AIAA Journal*, **46**(10), 2510–2519.

Appendix A – Extra Figures

The following appendix contains extra figures pertaining to experiment II.

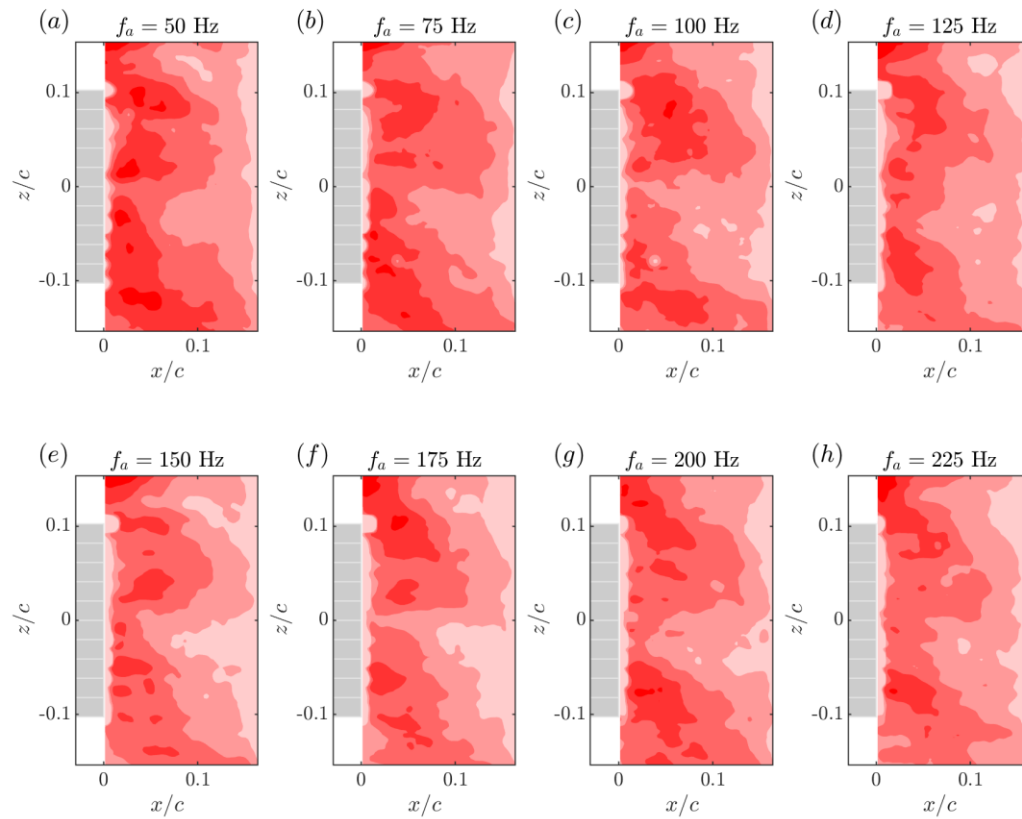


Figure A1. Streamwise Reynolds normal stresses ($\langle u^2 \rangle$) for actuating frequencies between $f_a = 50 - 225$ Hz under the two-dimensional mode.

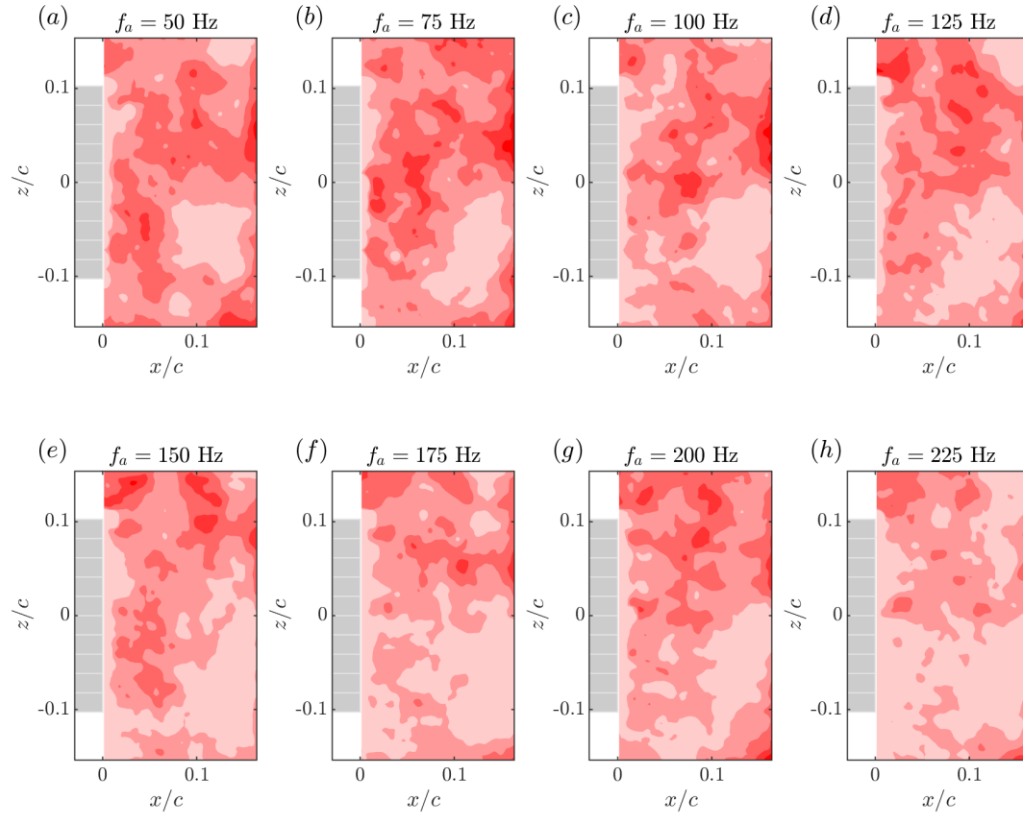


Figure A2. Spanwise Reynolds normal stresses ($\langle w^2 \rangle$) for actuating frequencies between $f_a = 50 - 225$ Hz under the two-dimensional mode.

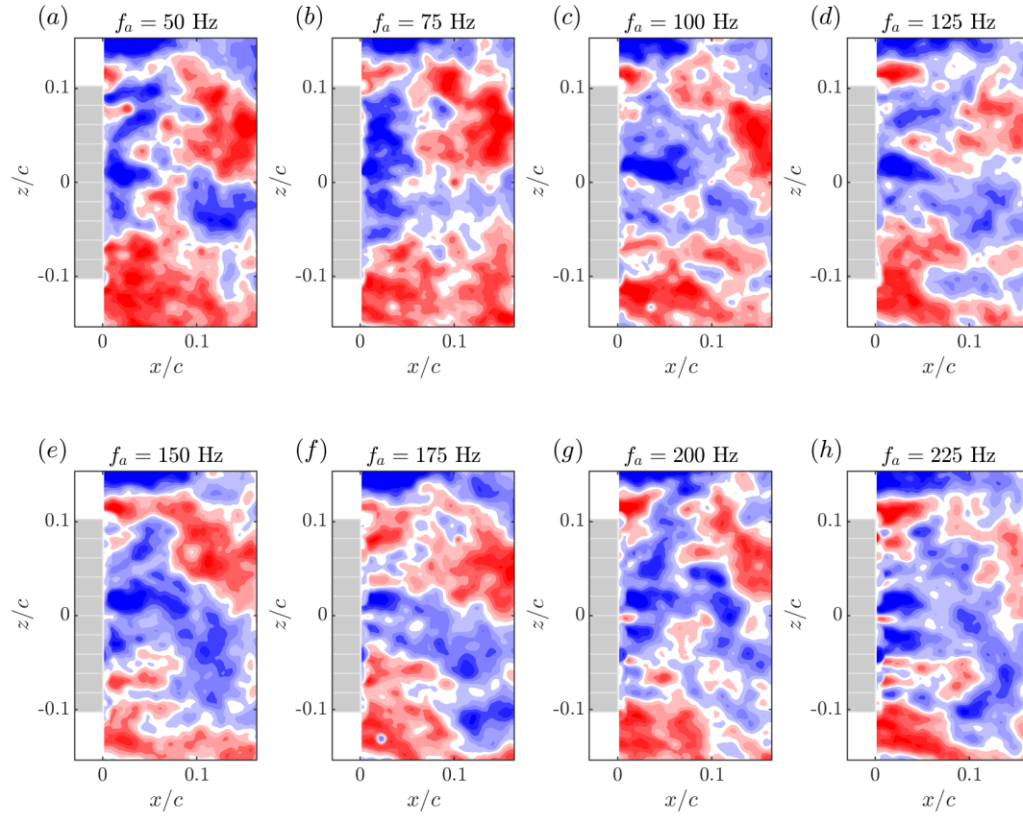


Figure A3. Reynolds shear stresses ($\langle uw \rangle$) of the near-wall flow for actuating frequencies between $f_a = 50 - 225$ Hz under the two-dimensional mode.

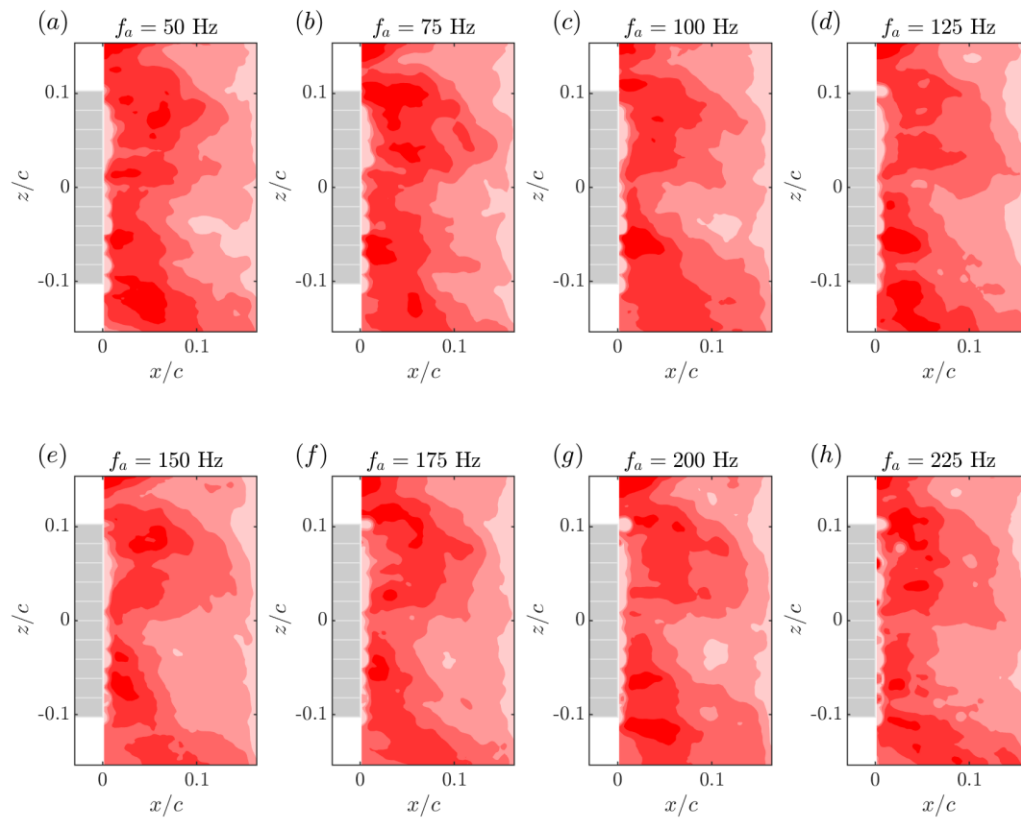


Figure A4. Streamwise Reynolds normal stresses ($\langle u^2 \rangle$) for actuating frequencies between $f_a = 50 - 225$ Hz under the three-dimensional mode.

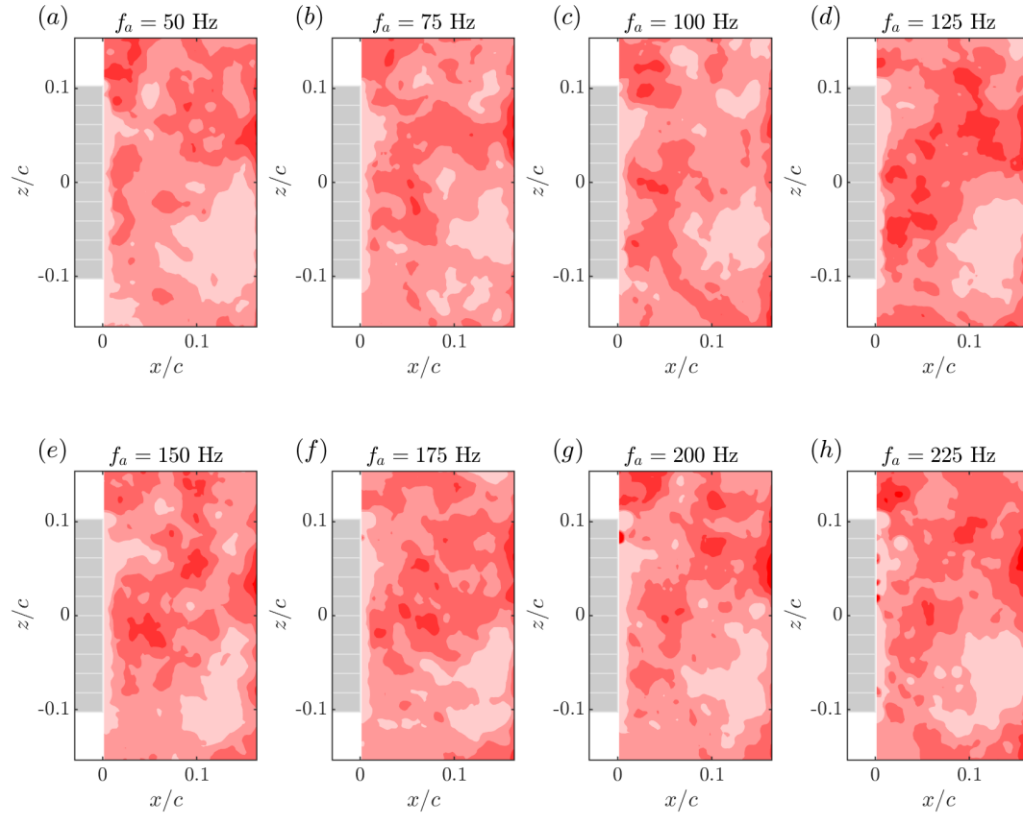


Figure A5. Spanwise Reynolds normal stresses ($\langle w^2 \rangle$) for actuating frequencies between $f_a = 50 - 225$ Hz under the three-dimensional mode.

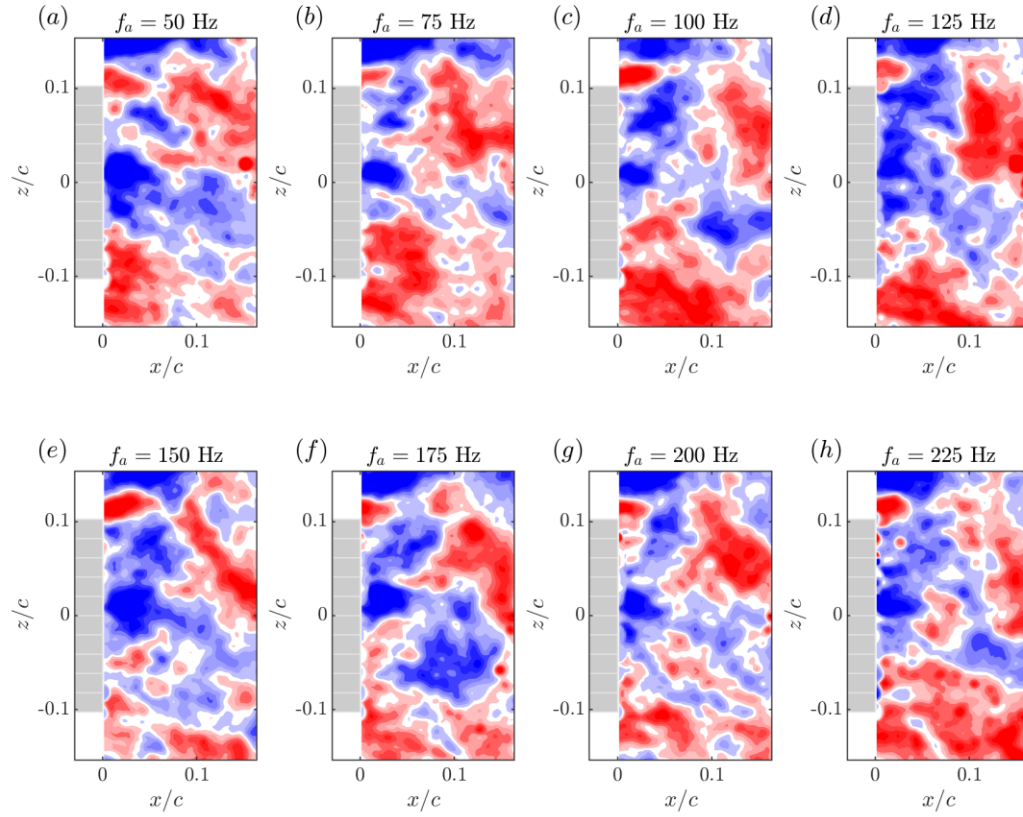
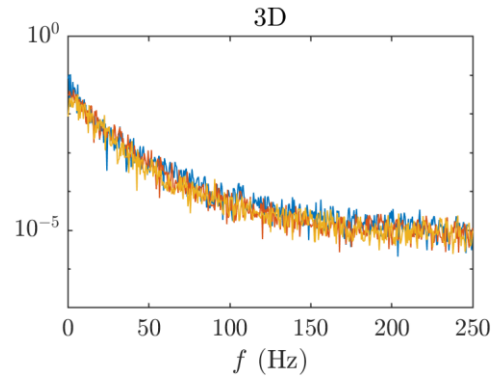
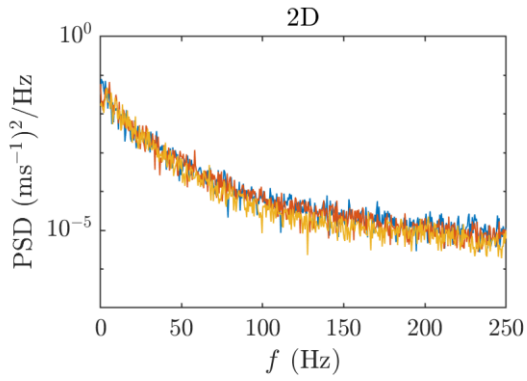
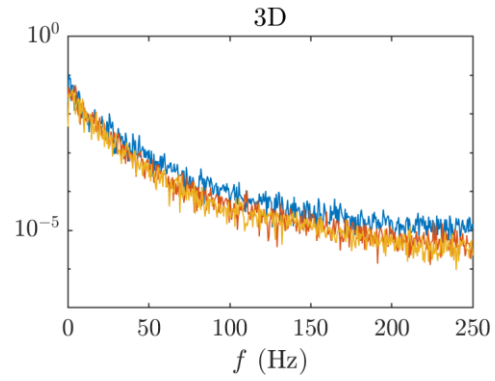
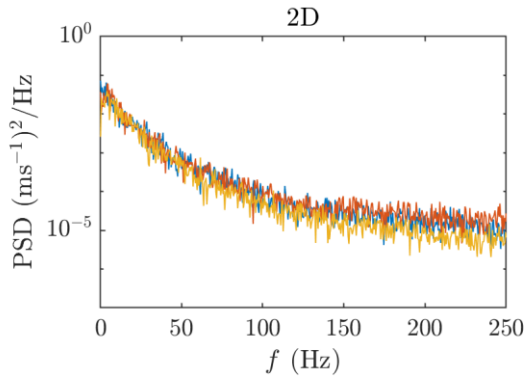


Figure A6. Reynolds shear stresses ($\langle uw \rangle$) of the near-wall flow for actuating frequencies between $f_a = 50 - 225$ Hz under the three-dimensional mode.

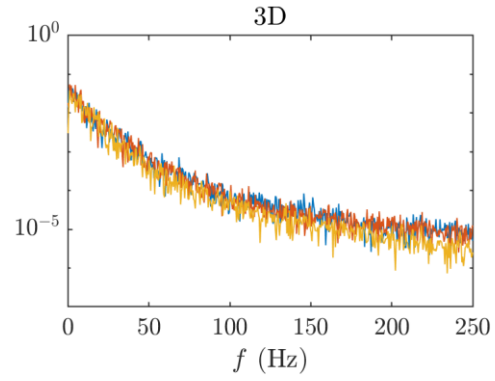
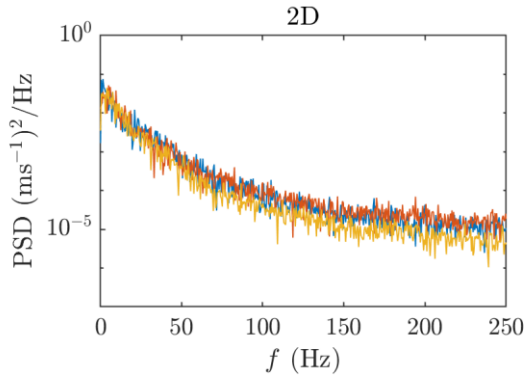
(a) $f_a = 50$ Hz



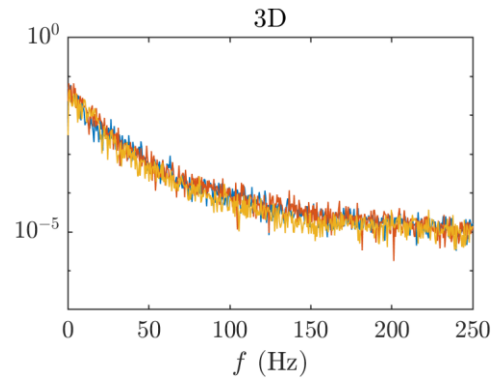
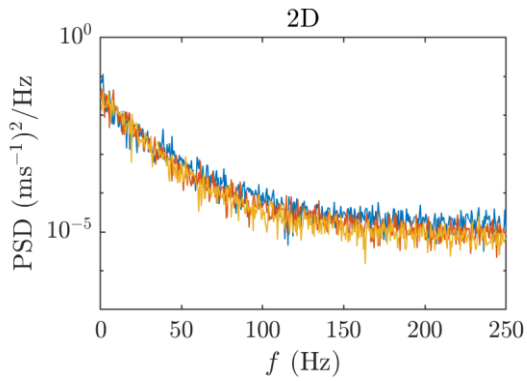
(b) $f_a = 75$ Hz



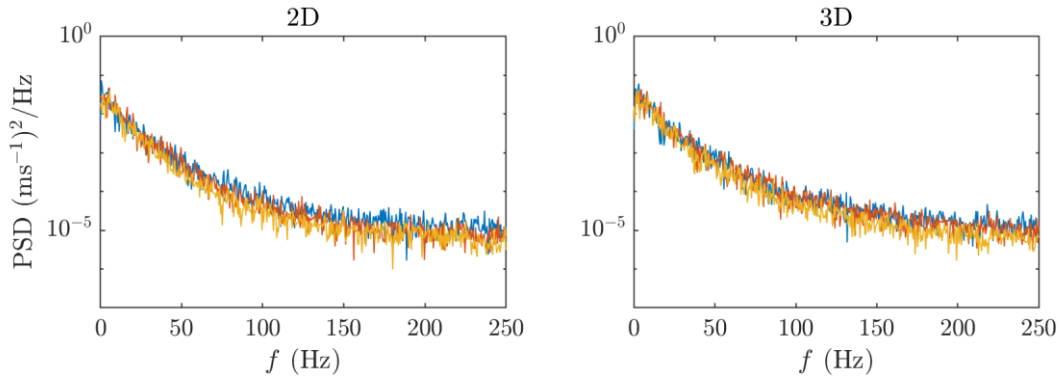
(c) $f_a = 100$ Hz



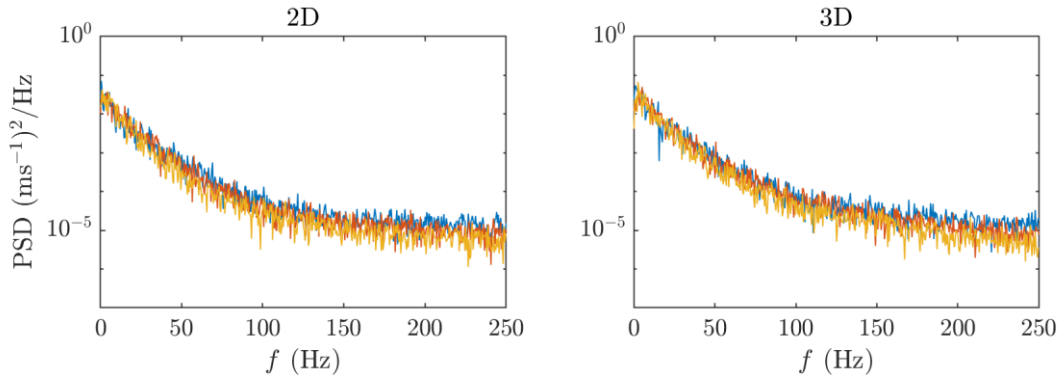
(d) $f_a = 125$ Hz



(e) $f_a = 150$ Hz



(f) $f_a = 175$ Hz



(g) $f_a = 200$ Hz

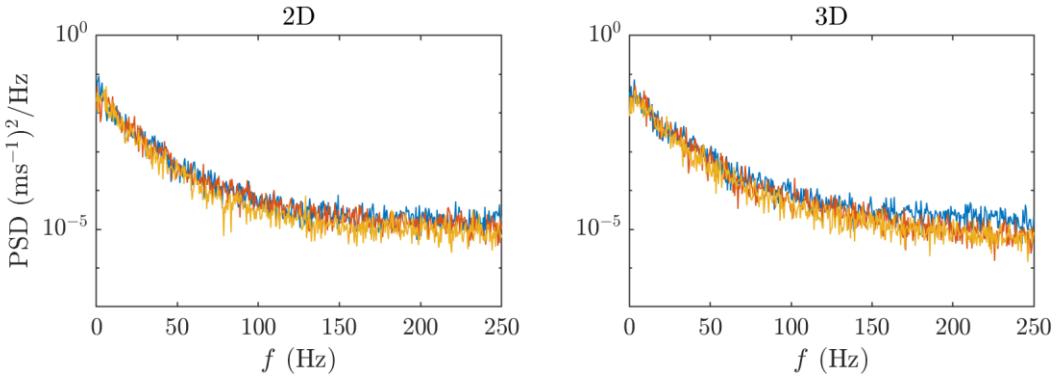
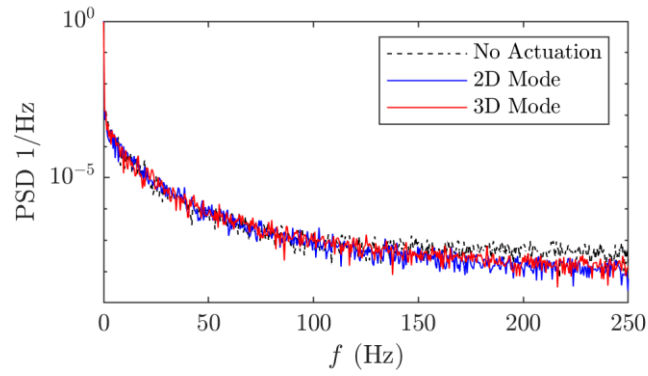
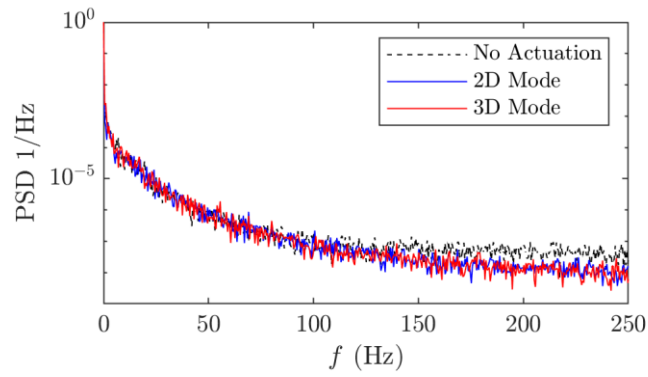


Figure A7. Power spectral density of the fluctuating streamwise velocity, u , for the (left) two-dimensional and (right) three-dimensional actuation mode at various actuating frequencies. The PSDs are obtained from points $x/c = 0.01, 0.05, 0.10,$ and 0.15 at $z/c = 0$ (midspan).

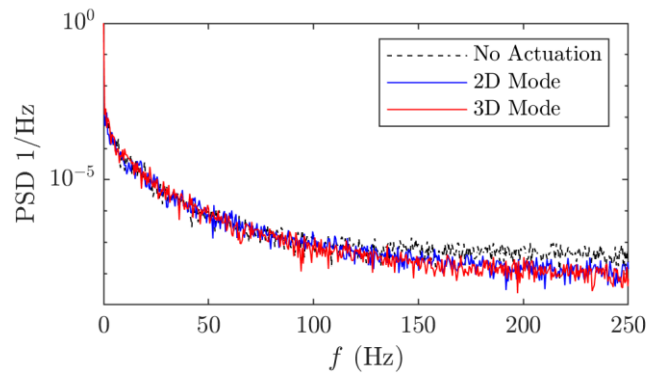
(a) $f_a = 50$ Hz



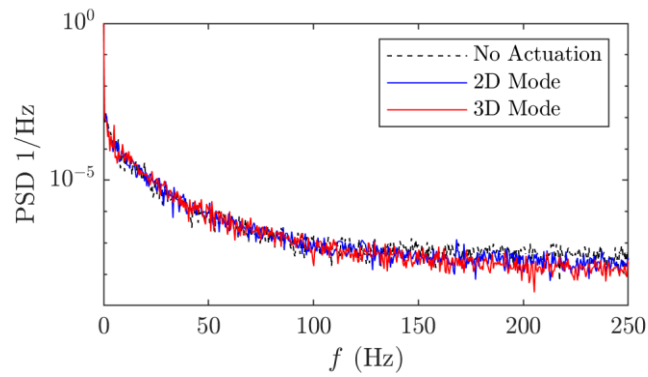
(b) $f_a = 75$ Hz



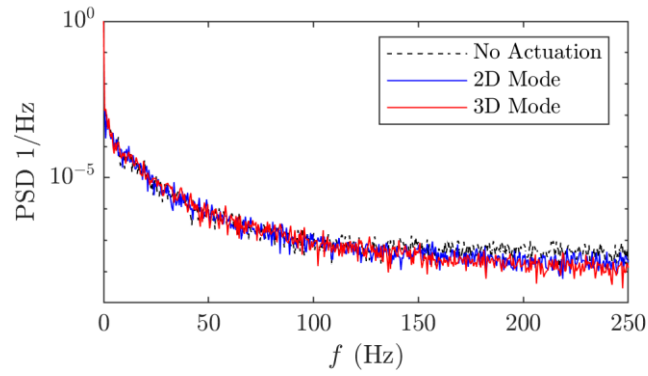
(c) $f_a = 100$ Hz



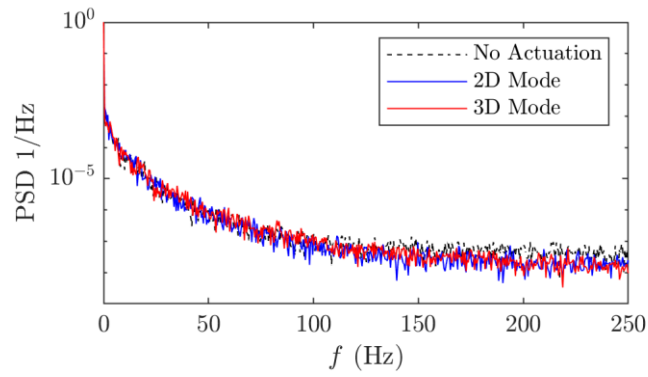
(d) $f_a = 125$ Hz



(e) $f_a = 150$ Hz



(f) $f_a = 175$ Hz



(g) $f_a = 200$ Hz

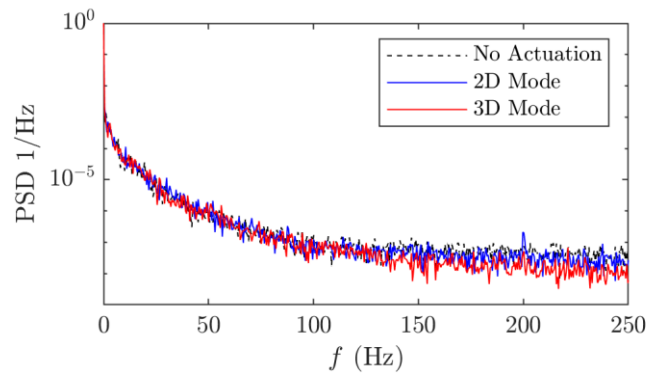


Figure A8. Power spectral density of the backflow ratio (I) for the separated flow with no flow control and two- and three-dimensional actuation at various actuating frequencies.

Appendix B – Matlab Codes

The following section contain the Matlab code used to track and characterize the critical points in experiment I. These codes were developed from scratch for the data collected in this project. The codes are shown here to keep track of the methodology behind the tracking algorithm.

B1. Identifying Possible Critical Points

```
% This code find critical points and classify them as saddle, foci, or
% nodes. Created by Austin Ma (ama2@ualberta.ca)

%%%%%%%%%%%%%%%%%%%%%%%%%%%%%%%%%%%%%%%%%%%%%%%%%%%%%%%%%%%%%%%%%%%%%%%%INPUTS%%%%%%%%%%%%%%%%%%%%%%%%%%%%%%%%%%%%%%%%%%%%%%%%%%%%%%%%%%%%%%%%%%%%%%%%
velThreshold = 0.02*12.0; %velocity magnitude threshold for classifying
critical points
checkSize = 4; %Radius for local min
calcLog = 1; %find critical points

%%%%%%%%%%%%%%%%%%%%%%%%%%%%%%%%%%%%%%%%%%%%%%%%%%%%%%%%%%%%%%%%%%%%%%%%INPUTS%%%%%%%%%%%%%%%%%%%%%%%%%%%%%%%%%%%%%%%%%%%%%%%%%%%%%%%%%%%%%%%%%%%%%%%%
load('StxSp_SAHS1.mat') % Sample data set

%get logistic matrix of local min and V < threshold
if calcLog == 1
    U_set = U2; V_set = V2;
    clear U2 V2 Q

    % Calculate velocity magnitude array
    V_mag = (U_set.^2+V_set.^2).^0.5;

    % Calculate vorticity to distinguish between CW and CCW foci
    vortZ = findVort(U_pos,V_pos,U_set,V_set);
    vortZ = single(vortZ);

    for ii = 1:size(U_set,3)
        minMatrix(:, :, ii) = isLocalMin(V_mag(:, :, ii), checkSize);
    end
    logMatrix = V_mag < velThreshold;

    CPMatrix = logMatrix & minMatrix; %find critical points as the overlap of
local mins and V_mag < threshold

    clear logMatrix minMatrix %clear to save memory
    clear amp V_mag
    disp('Calculation done.')
end
%%
% Find size of matrix CP
s = size(CPMatrix);
% Find grid size in X and Z direction
XStep = abs(U_pos(1,1)-U_pos(2,1));
ZStep = abs(V_pos(1,1)-V_pos(1,2));
% Start counts at 0
```

```

noSaddles = 0; noFoci = 0; noNodes = 0;
CCWfoci = 0; CWfoci = 0;
badBoyCount = 0; % Bad CPs (incorrect)

% Find location of possible critical points
linInd = find(CPMatrix == true);
[ii,jj,kk] = ind2sub(s,linInd);

% Find total number of CP and clear linInd to save memory
totCP = length(ii);
clear linInd

% Create wait bar to show progress
fprintf('Possible CPs: %10.0f\n',totCP);
MileStone = 0.01;
f = waitbar(0,'Analyzing possible critical points...');

% Loop for all possible CPs
for CPno = 1:totCP
    i = ii(CPno); j = jj(CPno); k = kk(CPno);

    % show progress in command window
    percDone = CPno/totCP;
    if percDone >= MileStone
        waitbar(percDone,f,sprintf('%3.0f percent done.',percDone*100));
        MileStone = MileStone + 0.01;
    end

    %classify points
    try
        pointType = detType(i,j,U_pos,V_pos,U_set(:, :, k),V_set(:, :, k));
    catch
        continue
    end
    %bin points
    switch pointType
        case 1
            noSaddles = noSaddles+1;
            saddlePts(noSaddles,1) = k;
            saddlePts(noSaddles,2) = U_pos(i,j);
            saddlePts(noSaddles,3) = V_pos(i,j);
        case 2
            noFoci = noFoci+1;
            fociPts(noFoci,1) = k;
            fociPts(noFoci,2) = U_pos(i,j);
            fociPts(noFoci,3) = V_pos(i,j);
            if vortZ(i,j,k)>0
                CCWfoci = CCWfoci + 1;
                CCWfociPts(CCWfoci,1) = k;
                CCWfociPts(CCWfoci,2) = U_pos(i,j);
                CCWfociPts(CCWfoci,3) = V_pos(i,j);
            else
                CWfoci = CWfoci + 1;
                CWfociPts(CWfoci,1) = k;
            end
    end
end

```

```

        CWfociPts(CWfoci,2) = U_pos(i,j);
        CWfociPts(CWfoci,3) = V_pos(i,j);
    end
case 3
    noNodes = noNodes+1;
    nodePts(noNodes,1) = k;
    nodePts(noNodes,2) = U_pos(i,j);
    nodePts(noNodes,3) = V_pos(i,j);
case 0
    badBoyCount = badBoyCount + 1;
end
end

% Clear old variables to save memory
clear U_set V_set vortZ V_mag CPMatrix

waitbar(1,f,sprintf('Complete'));

```

B2. Determining Type of Critical Point

```
%This function determine the point type of the designated critical point
%1 = saddle point, 2 = foci, 3 = node
function pointType = detType(rowNo, colNo, U_pos, V_pos, U_set, V_set)
    %air properties at 27oC from engineeringtoolbox.com
    rho = 1.177; %density in kg/m^3
    mu = 1.846e-5; %dynamic viscosity in kg/ms
    wallDist = 0.002; %2mm displacement of FOV from surface

    % Find grid spacing in X and Z direction
    XStep = max(abs(U_pos(1,1)-U_pos(1,2)), abs(U_pos(1,1)-U_pos(2,1)));
    ZStep = max(abs(V_pos(1,1)-V_pos(1,2)), abs(V_pos(1,1)-V_pos(2,1)));

    %linear approximation of du/dy and dw/dy by dividing V/wallDist
    dudy = U_set./wallDist;
    dwdy = V_set./wallDist;

    if nargin == 6
        noVal = 5; %take 5 points before and after point of interest for
numerical differentiation
    end

    % Calculate gradients
    ddxdudy = findDer(dudy(rowNo-noVal:rowNo+noVal,colNo),XStep);
    ddzdwdy = findDer(dwdy(rowNo,colNo-noVal:colNo+noVal),ZStep);
    ddxdwdy = findDer(dwdy(rowNo-noVal:rowNo+noVal,colNo),XStep);
    ddzdudy = findDer(dudy(rowNo,colNo-noVal:colNo+noVal),ZStep);

    %calculate skin friction parameters using 2nd order central
    %differencing scheme
    P = -mu*(ddxdudy + ddzdwdy);
    Q = mu^2*(ddxdudy*ddzdwdy - ddxdwdy*ddzdudy);

    D = P^2 - 4*Q;

    pointType = 0;

    % Skip point if determinant is too small to distinguish between CPs
    % using a threshold value
    if abs(D) < 1e-7
        return
    end

    %calculate S1 and S2
    S1 = (-P+sqrt(P^2-4*Q))/2;
    S2 = (-P-sqrt(P^2-4*Q))/2;

    S1_real = isreal(S1);
    %S2_real = isreal(S2);

    if S1_real == 0 %if S1 is complex then point is a focus
```

```

        pointType = 2;
    else
        S1S2 = S1*S2;
        if S1S2 > 0
            pointType = 3; %node if both S1 and S2 are same sign
        else
            pointType = 1; %saddle point if S1 and S2 are opposite signs
        end
    end
end
end

function outSlope = findDer(f,h)
    if mod(length(f),2) == 0
        error('Input should contain odd number of data.')
    else
        %convert f to row vector if it is a column vector
        if isrow(f) == 0
            f = f';
        end

        s = (length(f)-1)/2;
        x = h*(-s:1:s);
        p = polyfit(x,f,2); %polyfit using a quadratic polynomial
        outSlope = p(2); %slope at x = 0 is the second coefficient
    end
end
end

```

B3. Calculating Track Velocities

```
% This code calculates the velocity of CPs for a trx.mat

% Clear and close existing windows
clear
clc
close all

% List of data files
fileName = {'StxSP_SAHS1_CP2_trx.mat',...
           'StxSP_SAHS2_CP2_trx.mat',...
           'StxSP_SAHS3_CP2_trx.mat',...
           'StxSP_SAHS4_CP2_trx.mat',...
           'StxSP_SAHS5_CP2_trx.mat'};

% Experiment setting
fs = 1750;
U_inf = 12.0;

% Loop for all types of critical points
for CurrType = [1,2,3]
    % clear old data to save memory
    clear vList analMat CPIIds U W

    % Initialize U and W arrays
    U = []; W = [];

    % Loop over every dataset
    for jj = 1:5
        load(string(fileName(jj)))

        % Grab matrix based on current type of CP
        switch CurrType
            case 1
                analMat = SPMatrix;
            case 2
                analMat = CWMatrix;
            case 3
                analMat = CCWMatrix;
        end

        % Find unique CPs
        CPIIds = unique(analMat(:,4))';

        vList = cell(length(CPIIds),3);

        % loop over every CP ID
        warning off
        for i = 1:length(CPIIds)
            idNo = CPIIds(i);

            placeholder = analMat(analMat(:,4) == idNo,:);

            t = 1/fs*placeholder(:,1); %create time vector
        end
    end
end
```

```

xnew = kernRgrs(t,placeholder(:,2),5);
ynew = kernRgrs(t,placeholder(:,3),5);

vList(i,1) = {idNo};

vList(i,2) = {0.001*xnew.dydx(2:end-1)}; %x speed in m/s
vList(i,3) = {0.001*ynew.dydx(2:end-1)}; %z speed in m/s
U = [U, 0.001*xnew.dydx(2:end-1)]; % Append U
W = [W, 0.001*ynew.dydx(2:end-1)]; % Append W
end
warning on
end

% Calculate mean velocities and speeds
Uavg = nanmean(U); Wavg = nanmean(W);
Uavg2 = nanmean(abs(U)); Wavg2 = nanmean(abs(W));

% Plot convergence values
Uavg_Con = testConv(U); Wavg_Con = testConv(W);
Uavg2_Con = testConv(abs(U)); Wavg2_Con = testConv(abs(W));
NN = 1:length(U);

% Create figures
figure()
plot(NN, Uavg_Con/U_inf, 'k-', NN, Uavg2_Con/U_inf, 'k--',
', NN, Wavg_Con/U_inf, 'r-', NN, Wavg2_Con/U_inf, 'r--')
legend('$\langle U_a \rangle / U_{\infty}$', ...
'$\langle |U_a| \rangle / U_{\infty}$', ...
'$\langle W_a \rangle / U_{\infty}$', ...
'$\langle |W_a| \rangle / U_{\infty}$', 'interpreter', 'latex', 'fontsize', 10)
xlabel('N, Data Points', 'interpreter', 'latex'); ylabel('Normalized
Advection Velocity', 'interpreter', 'latex')
set(gca, 'ticklabelinterpreter', 'latex')
set(gcf, 'units', 'centimeters', 'position', [5 5 8.5 6])
switch CurrType
case 1
    SPvel = vList;
    disp('Completed analysis for saddle points.')
    fprintf('Average u = %2.3f, Average |u| = %2.3f\nAverage w =
%2.3f, Average |w| = %2.3f\n\n', Uavg, Uavg2, Wavg, Wavg2);
case 2
    CWvel = vList;
    disp('Completed analysis for clockwise foci.')
    fprintf('Average u = %2.3f, Average |u| = %2.3f\nAverage w =
%2.3f, Average |w| = %2.3f\n\n', Uavg, Uavg2, Wavg, Wavg2);
case 3
    CCWvel = vList;
    disp('Completed analysis for counter-clockwise foci.')
    fprintf('Average u = %2.3f, Average |u| = %2.3f\nAverage w =
%2.3f, Average |w| = %2.3f\n\n', Uavg, Uavg2, Wavg, Wavg2);
end
end
end

```

```
%% Test for convergence
% A is an array of value to test convergence for
% B is the output of mean as a function of N
function B = testConv(A)
    n = length(A);
    for i = 1:n
        segA = A(1:i);
        B(i) = nanmean(segA);
    end
end
```